nks

Nordisk kernesikkerhedsforskning
Norrænar kjarnöryggisrannsóknir
Pohjoismainen ydinturvallisuustutkimus
Nordisk kjernesikkerhetsforskning
Nordisk kärnsäkerhetsforskning
Nordic nuclear safety research

NKS-203
ISBN 978-87-7893-272-3

Improving Accuracy of the Calculation of In-core Power Distributions for Light Water Reactors

Makoto Tsuiki and William H. Beere

Institute for energy technology, OECD Halden Reactor Project, Norway

October 2009

Abstract

Comparisons have been made of VNEM prototype system to the measured data obtained from Ringhals unit 3 NPP at its beginning of life, hot-stand-by state. Three cases with difference control rod bank positions and Boron concentrations have been compared:

Case 1: nearly all rod banks withdrawn, Boron = 1315 ppm
Case 2: bank C = nearly half-inserted, bank D = fully inserted, Boron = 1131 ppm
Case 3: banks C and D = fully inserted, Boron = 1060 ppm

The results can be summarized as:

	error: maximum detector reading (%)	error: keff (%)
Case 1	-2.1	-0.175
Case 2	1.5	-0.022
Case 3	-0.5	-0.044

Excellent agreement was observed in the comparison of the neutron detector readings and the core eigenvalues.

The method of core modelling and parameters used in calculation of VNEM is completely the same as the "PWR standard option" determined from similar comparisons of VNEM and other PWRs. No empirical, or any sort of adjustment was done.

Key words

VNEM, Ringhals, unit 3, PWR, neutron detector, keff, IACIP: NKS_R_2008_61

NKS-203
ISBN 978-87-7893-272-3

Electronic report, October 2009

NKS Secretariat
NKS-776
P.O. Box 49
DK - 4000 Roskilde, Denmark

Phone +45 4677 4045
Fax +45 4677 4046
www.nks.org
e-mail nks@nks.org

	Document type	Page
Institutt for energiteknikk **OECD HALDEN REACTOR PROJECT**	ANNUAL REPORT	1/79
Org./Author	Date Code	
IFE / Makoto Tsuiki and William H. Beere	10.12.2008 AR-VNEM-NKS-R-01-08 (r1)	
Distribution	Checked by	Date
NKS-R Program Manager	IFE / Jan Porsmyr	
VTT	Approved by	Date
	IFE / Oivind Berg	
	Replaces	Retention time
		☐ <7 ☐ 8...14 ■ >15

Keywords
VNEM, Ringhals, unit 3, PWR, neutron detector, keff, IACIP: NKS_R_2008_61

Comparison of VNEM to Measured Data from Ringhals Unit 3 IACIP, NKS-R-2008-61

Purpose

According to the agreement between NKS-R program management and Institutt for Energiteknikk (IFE), a verification study of the transport variational nodal expansion method (VNEM) has been performed based on the specification in the offer dated 28.11.2007 for NKS-R-2008-61 (IACIP). This report presents the results of the study in detail.

Abstract

Comparisons have been made of VNEM prototype system to the measured data obtained from Ringhals unit 3 NPP at its beginning of life, hot-stand-by state. Three cases with difference control rod bank positions and Boron concentrations have been compared:

Case 1: nearly all rod banks withdrawn, Boron = 1315 ppm
Case 2: bank C = nearly half-inserted, bank D = fully inserted, Boron = 1131 ppm
Case 3: banks C and D = fully inserted, Boron = 1060 ppm

The results can be summarized as:

	error: maximum detector reading (%)	error: keff (%)
Case 1	–2.1	–0.175
Case 2	1.5	–0.022
Case 3	–0.5	–0.044

Excellent agreement was observed in the comparison of the neutron detector readings and the core eigenvalues.

The method of core modelling and parameters used in calculation of VNEM is completely the same as the "PWR standard option" determined from similar comparisons of VNEM and other PWRs. No empirical, or any sort of adjustment was done.

Table of Contents

1. Comparison of VNEM to Ringhals-3 Plant Data

1.1 Introduction

In this chapter the results of the verification of VNEM by comparing it to the plant data from Ringhals unit 3 are shown. The 3-dimensional (3D) version of VNEM (VNEM3D) is used for calculations. The VNEM solution method adopted in VNEM3D code is explained in the appendix A. Because VNEM3D code still does not include the feedback effects (thermal-hydraulic, burnup, Xenon, etc.), the comparisons have been made for the hot-stand-by core condition at the beginning of its life, for the readings of the in-core neutron detectors and the effective multiplication factor (keff, or the core eigenvalue). The cases for the comparison will be specified in the next section in detail.

The group cross sections of fuel pin-cells are calculated by a lattice code HELIOS [1.1].

1.2 Cases for Comparison

Comparisons are made for the following 3 cases:

Case 1: BOC, 4% power, equilibrium Xenon, boron concentration = 1315 ppm,
fuel temp. = 559K, moderator temp. = 559K,
bank D = 212 - 228 steps (moving during measurement),
all othe banks = 228 steps

Case 2: BOC, 4% power, equilibrium Xenon, boron concentration = 1131 ppm,
fuel temp. = 559K, moderator temp. = 559K,
bank C = 110 - 112 steps (moving during measurement)
bank D = 0 steps,
all othe banks = 228 steps

Case 3: BOC, 4% power, equilibrium Xenon, boron concentration = 1060 ppm,
fuel temp. = 559K, moderator temp. = 559K,
bank B = 217 steps,
bank C = 0 steps,
bank D = 0 steps,
all othe banks = 228 steps

The fuel types in the reactor core are given in Table 1.2.1. The core loading pattern is defined by the fuel types as shown in Fig.1.2.1.

1.3 Comparison Procedure

Figure 1.3.1 shows the flow diagram of the comparison work.

The number of energy groups is assumed to be 7, based on the preliminary analysis. The group boundaries are:

group	upper boundary		lower boundary
1	∞	to	1 MeV
2	1 MeV	to	9.119 KeV
3	9.119 KeV	to	3.9279 eV

4	3.9279 eV	to	0.625 eV
5	0.625 eV	to	0.27052 eV
6	0.27052 eV	to	0.11157 eV
7	0.11157 eV	to	0 eV

The fuel-pin-cell-homogenized 7 group macroscopic cross sections are calculated by HELIOS[1.1] lattice code with ENDFB-6 library. The measured readings of the traversing neutron fission chambers are also sent from Ringhals NPP to IFE, Halden. The radial reflector is assumed to be the light water containing the same Boron as the coolant and including the baffle of 2.2 cm thickness surrounding completely the core. The bottom and the top reflectors are assumed to be a homogeneous mixture of:

bottom: plugs, detector thimbles, and control rod guide tubes,
top: claddings, springs, sealed gas, detector thimbles, control rod guide tubes, and grid.

The FCM2D code calculates a fuel-pin cell angular flux distribution for each of the fuel types, as well as the reflector nodes based on the single-assembly 2D characteristic transport method (CM). The code FCM2D is based on fuel-pin cell homogenized transport calculation.

When VNEM is finally implemented into existing code system, FCM2D code calculations (as well as the fuel-pin cell homogenization) are not needed because the necessary data are provided from alttice codes directly to VCOEF3D.

The parameters used in FCM2D calculations are:

No. of regions:	289 regions = 1 × 1 meshes / fuel cell
No. of azimuthal angles:	80 / 2π
No. of polar angles:	20 / π
Spacing of characteristics:	< 1.9 mm

The VCOEF3D code calculates the VNEM coefficients using the equations described in the appendix A.

The VNEM coefficients prepared by using FCM2D and VCOEF3D are for the assemblies listed in Table 1.2.1 and the radial, bottom and top reflector nodes. For assembly type 1 and 6 (see Table 1.2.1), FCM2D and VCOEF3D calculations are made also for the control rods inserted cases.

The VNEM3D code solves the variational nodal transport equations described in the appendix A and calculates the core power distribution and the core eigenvalue (keff).

Finally the code OTEDIT make the comparison between the measured (from Ringhals NPP), and the calculated (by VNEM3D) detector readings. The methods of the comparison are explained in Section 1.4.

1.4 Method of Comparison

In this section the methods of comparing the measured and the calculated detector readings are discussed.

1.4.1 Core Model of VNEM Calculations

The geometrical core model used in VNEM is shown in Fig.1.4.1. In the radial direction, 1 node / 1 assembly is taken. The radial reflector is treated as "reflector assemblies" that have the same size and shape as the fuel assemblies. The active fuel length is divided into 24 axial nodes of the same size and shape. Therefore a node is nearly a cube of the size: 21.42 cm × 21.42 cm × 15.24 cm in x, y and z directions. It should be noted that the axial node boundary is not necessarily be the same position as the control rod head, therefore we need the homogenization procedure described in Section 1.4.5. The axial reflectors are assumed to be the same size and shape as the node for a fuel assembly, and 1 axial reflector node is set at the top and the bottom of the core.

A quarter-core symmetry is assumed. So we have 8 by 8 assemblies as shown in Fig.1.4.1(a). A zero-flux boundary condition is posed at the outer boundary of the reflector both in the radial and the axial directions.

The assembly loading pattern in the core is shown in Fig.1.2.1. The reference values for parameters in VNEM are listed in Table 1.4.1.

1.4.2 VNEM-Calculated Readings

The code VNEM3D calculates the detector readings in the same way as the normal fuel pin power by Eq.(A.7.7), except that at the thimble position there are infinitely-diluted U235 atoms instead of a normal fuel rod. As we have 24 axial nodes (see Fig.1.4.1), we obtain 24 nodal readings from VNEM3D:

RVn(k = 1:24, i = 8:15, j = 1:8)

where indices k, i and j are:

k: axial node position index
i: node position index in x-(west to east) direction
j: node position index in y-(south to northe) direction

Also refer to Figs.1.4.1 and 1.2.1 for these indices.

By using a quadratic interpolation, we estimate the readings at 60 measuring positions for all the assemblies:

RVm(m = 1:60, i = 8:15, j = 1:8)

The interpolation is defined by, for measuring point m between axially center points of nodes k and k + 1 (the indices i, j are omitted):

(1) Make a quadratic interpolation using RVn(k – 1), RVn(k), RVn(k +1) to obtain RVLm.
(2) Make a quadratic interpolation using RVn(k), RVn(k + 1), RVn(k + 2) to obtain RVUm.
(3) The average of (1) and (2) is taken as the reading at measuring point m, i.e.

RVm(m) = (RVLm + RVUm) / 2

(4) If k = 1 then only interpolation (2) is made, similarly, if k = 23 then only interpolation (1) is made to estimate the reading at measuring point m, i.e.

RVm(m) = RVUm, if k = 1

RVm(m) = RVLm, if k = 23

(5) If k = 0 then a quadratic extrapolation is made using RVn(1), RVn(2), RVn(3) to obtain RVm(m), similarly, if k = 24 then a quadratic extrapolation is made using RVn(22), RVn(23), RVn(24) to obtain RVm(m).

We could have calculated RVm directly by using Eq.(A.7.2) in the appendix A. The reason we used the above interpolation formula is only because we have not implemented Eq.(A.7.2) into the prototype code VNEM3D. This will be performed in near future.

The calculated detector readings RVm(m = 1:60, i = 8:15, j = 1:8) are corrected to include the dips at spacer grids, because the magnitude of these dips are not negligible at all and the dips are also needed to correct the misalignment of the axial position of the measurements.

As no information is available about the exact position of the grids (they may move from their nominal positions), it is assumed that

$$Gp(mg) = Bg + (mg - 1) \times Dg + Ag(mg)$$

where mg = 1:8 is the grid number from the bottom of the fuel, Gp(mg) is the position (cm from the bottom of the fuel), Bg = Gp(1), Dg is the grid spacing (cm), and Ag is the fine adjustment of the grid position. The values of Bg, Dg, and Ag are determined to obtain the best fit of the spacer dips between the measured and the calculated readings, and are listed below:

Bg = 12.4 cm
Dg = 49.9 cm
Ag(1) = 0.0 cm
Ag(2) = 6.2 cm
Ag(3) = 6.2 cm
Ag(4) = 6.2 cm
Ag(5) = 9.3 cm
Ag(6) = 12.4 cm
Ag(7) = 12.4 cm
Ag(8) = 0.0 cm

The magnitude of the dip is assumed to be:

(1) reading with grid (grid position) / reading without grid (grid position) = 0.900
(2) reading with grid (grid position ± dm)
/ reading without grid (grid position ± dm) = 0.965
(3) reading with grid (grid position ± 2 × dm)
/ reading without grid (grid position ± 2 × dm) = 0.990

where dm is the distance (cm) between the measuring position, therefore

dm = active fuel length / 59 = 6.2 cm

The dip of the readings due to the grid should be estimated in a more physical way. However, as there is no information on the grid material, or position etc, we made empirical fitting of the magnitude of the dip. The method is first we remove the cosine-component of the measured and the calculated readings. Then by a try-and-error process, we found nearly the best fit of the magnitude of the dip as given above.

The corrected readings are re-normalized so that the average over all the measuring points becomes 1.0. No other special normalization is performed.

It should be noted that the grid correction described here is only made to the detector readings. No grid correction is done within VNEM3D. This is again because there is no information so far on the grid.

The amount of dip at measuring position is calculated by linearly interpolating the dips determined by (1), (2), and (3) above.

1.4.3 Normalization of Measured Readings

The measured readings from 5 detectors A through E are normalized so that their average readings at "common thimble" J07 (assembly i = 7, j = 7, see Fig.1.2.1) are the same. They also are divided by the flux level at the measurement to remove its effect on the readings. Finally the measured readings are normalized so that their spatial average over all the measuring position becomes 1.0 (as in the case of the calculated readings), after misalignment correction described in 1.4.4.

1.4.4 Misalignment Correction of Measured Readings

The misalignment of measuring positions in the measured readings is clearly observed and is significant. The upper graph of Fig.1.4.1 shows the relative measured readings (normalized so that the average over all measuring points = 1.0) along assembly (i = 8, j = 4) together with the calculated in Case 2. The position of the dips of the measured readings caused by the grid spacers is obviously shifted to the left (upward).

Such misalignment is corrected by the following way:

(1) In an assembly, normalize the measured and the calculated readings, RMm(m) and RVm(m) so that

$$\sum_{m = 1, 60} RV'm(m).w(m) / \sum_{m = 1, 60} w(m) = 1$$
$$\sum_{m = 1, 60} RM'm(m).w(m) / \sum_{m = 1, 60} w(m) = 1$$

where RV'm(m) and RM'm(m) are the VNEM-calculated and the measured readings at measuring position m normalized as above, w(m) is the weight of the position m defined by:

w(1) = w(60) = 0.5
w(2:59) = 1.0

(2) Find a shifting distance Da which minimizes the root mean square deviation

$$RMS = SQRT[\sum_{m = 1, 60} \{RM'm(m) - RV'm(m)\}^2 / 60]$$

by shifting RM'm(m) along the axial direction by Da.

(3) Shift the measured readings RMm(m) of this assembly by Da.

(4) At the top or the bottom of the assembly, the measured data may not be available because of the shift. For example, if we shift the measured readings to the right in the case of Fig.1.4.1 by 3 measuring points, no data are available at position

m = 1, 2, 3. In such a case the calculated readings are set to these positions as "aligned measured readings", i.e. we set

$$RMm(m) = RVm(m), \quad \text{for } m = 1, 2, 3$$

The lower graph of Fig.1.4.1 shows the comparison of the aligned RMm(m) and RVm(m). As shown by this graph, the alignment of the measured readings is quite successful.

1.4.5 Control Rod Effect

The control insertion length (from the top of the active fuel) can be calculated as:

Control rod steps at the top of the active fuel = 225 steps
Control rod move / step = 1.5905 cm / step

therefore,

Control rod insertion length (cm) = (225 – S) * 1.5905

The heads of control rods are not always at the axial boundary of nodes (see Fig.1.4.1). When the control rods are partly inserted into a node, its VNEM coefficients are homogenized by:

$$C_{\text{homogenized}} = VF_{\text{rods not inserted}} C_{\text{rods not inserted}} + VF_{\text{rods inserted}} C_{\text{rods inserted}} \qquad (1.4.1)$$

where

$C_{\text{homogenized}}$: homogenized VNEM coefficient (defined in the appendix A)
$C_{\text{rods not inserted}}$: VNEM coefficient without control rods
$C_{\text{rods inserted}}$: VNEM coefficient with control rods inserted
$VF_{\text{rods not inserted}}$: Volume fraction of control rods inserted part of the node
$VF_{\text{rods inserted}}$: $1 - VF_{\text{rods not inserted}}$

1.5 Results of Comparisons

In this section the comparison results of the detector readings and the core eigenvalues between the measured and the calculated by VNEM are discussed.

The results of the comparisons are summarized as, for

Case 1:

Fig.1.5.1: Core average relative axial readings
Fig.1.5.2: Assembly average relative radial readings
Fig.1.5.3: Readings in assembly H4 (i = 8, j = 4), where the maximum reading is observed in Case 1.

Case 2:

Fig.1.5.4: Core average relative axial readings
Fig.1.5.5: Assembly average relative radial readings
Fig.1.5.6: Readings in assembly H4 (i = 8, j = 4), where the maximum reading is observed in Case 1.

Case 3:

Fig.1.5.7: Core average relative axial readings
Fig.1.5.8: Assembly average relative radial readings
Fig.1.5.9: Readings in assembly J3 (i = 7, j = 3, which is equivalent ot i = 9, j = 3 due to the symmetry of the core), where the maximum reading is observed in Case 1.

The core eigenvalue for each of the cases is shown in Table 1.5.1. The comparison of the maximum reading in the core is shown in Table 1.5.2.

The results of comparisons at all the measuring points of cases 1 2, and 3 are shown in the figures in Appendices B1, B2 and B3, respectively. In these figures, the upper and the lower bounds of the emasured readings are taken from the maximum and the minimum readings of assemblies at octant-symmtric positions, as in Figures 1.5.2, 1.5.5 and 1.5.8.

1.6 Computing Time and Convergence Acceleration

In this section topics related to the computing time of VNEM3D are discussed.

1.6.1 Computing Time

The computing time is measured by using a PC:

PC: HP Compaq dx6100
OS: Windows XP professional
CPU: Pentium-4 (3GHz)
RAM: 2.99GHz / 1.49GB

The computing time of VNEM3D is:

0.13 sec / group / inner iteration / outer iteration

where the parameters are

No. of nodes: 26 (axial) × 64 (radial) = 1664
PL order: P3
No. of axial meshes: 4 / node

This means that the calculation of VNEM3D for a case of Ringhals Unit 3 quarter core requires about 25 minutes of computing time.

1.6.2 Acceleration Technique

We use the method of the usual source iterations [1.2] to calculate the core eigenvalue, and Gauss-Seidel method [1.3] to solve simultaneous linear equations required to perform the source iterations in the code VNEM3D.

The source iteration is accelerated by using the method of coarse-mesh rebalancing [1.4].

1.7 References for Chapter 1

[1.1] F. D. Giust, R. J. J. Stamm'ler, and A. A. Ferri: "HELIOS1.7 User Guide and Manual," Studsvik and Scandpower (2001)
[1.2] http://www.nr.titech.ac.jp/coe21/events/pdf/NuclReactorTheoryTextbook.pdf
[1.3] http://mathworld.wolfram.com/Gauss-SeidelMethod.html
[1.4] http://wwwsoc.nii.ac.jp/aesj/publication/JNST2004/No.8/41_781-789.pdf

2. Conclusions

2.1 Comparison Results

From the comparison of VNEM3D to the measured data from Ringhals unit 3, we conclude that:

(1) The agreement of detector readings between VNEM3D and the measured data is very good, as shown by Table 1.5.2 and Figures 1.5.1 through 1.5.9, as well as the appendices B1 through B3.

In some cases the calculated assembly average readings have some errors to the measured, however, as shown in the appendices B1 through B3, the measured readings have (in some cases quite large) assymmetry even for the core with octant symmetry. Therefore we cannot conclude that the errors are caused by the calculation method, rather we need some more information to estimate accurate measured readings for these cases.

(2) The core eigenvalues calculated by VNEM3D are also agree very well to the measured value (1.0) in cases 2 and 3 (see Table 1.5.1). The calculated value is slightly smaller than the measured in case 1. The reason for this may be because of the rapidly increasing fission products at the beginning of the life of the core, or the effect of the control rod banks that were moving even during the measurement.

2.2 Future Works

The required tasks to finalize the system are:

1. Develop VNEM coefficient generator: VCOEF code.
2. Develop VNEM coefficients tabulator: VTABLE code.
3. Burnup-tilt model development.
4. Make VNEM module faster.
5. Built in VNEM module into CYGNUS code.
6. QA of VNEM

Each of the tasks will be described below.

2.2.1 VCOEF3D Code

VCOEF3D calculates the expansion functions of VNEM in a node by solving mono-energetic (for each of the energy groups) 2-dimensional (2D) neutron transport equations with the method of characteristics (CM) for a given state-point and the fuel type of the node. Here we assume that a node is homogeneous (spatially uniform) along axial direction, so a node is

treated in 2D Cartesian geometry. As the boundary values for the expansion functions are known, this process can be performed analytically. The regions within a node are bounded by either straight lines or circular arcs. Each of the regions is assumed spatially homogeneous.

For the given state-point, VCOEF3D also calculates VNEM coefficients, which are interpreted as macro neutron cross sections averaged (or "homogenized" in a sense) over whole nodal volume. The coefficients of equations solved by VNEM module in 3D core simulator are calculated from the VNEM coefficients.

The present version of VCOEF3D can only accept rectangle regular mesh structure within a node, as a result the so-called "fuel cell homogenization" is necessary. This feature must be removed in the production version, and VCOEF3D should make the calculations based on the geometrical structures provided by lattice codes. With this new VCOEF3D the FCM2D calculations in Fig.1.3.1 can be removed because the solution of lattice codes can directily be used in VCOEF3D.

2.2.2 VTABLE Code

VTABLE compiles the VNEM coefficients calculated by VCOEF3D for a complete set of state-points and fuel types of nodes. VTABLE also tabulates the compiled VNEM coefficients so that VNEM module of 3D core simulator can reproduce them for all of the nodes in the reactor core in which the neutron transport equations are solved to obtain the in-core power distribution.

2.2.3 Burnup-Tilt Model

The burnup (the net depletion of fissile isotopes and accumulation of fission products due to the exposure of fuel to the neutron flux) of a node is calculated by a lattice code, because the VNEM coefficients are very much dependent on it.

One problem is that in a lattice code a reflective boundary condition is assumed at the outer boundary of a given node, because there is no way to know the actual boundary condition. This is equivalent to assuming that the given node is surrounded by itself. However, when a node is put in an actual reactor core, its surroundings are generally different from what is assumed in a lattice code. Then the spatial distribution of the neutron flux and the burnup within a node is different in an actual reactor core from that in a lattice code. As a result VNEM coefficients may be different for a node in an actual reactor core from those calculated by VCOEF3D code based on the burnup of a lattice code.

The burnup-tilt model should be developed to correct this effect on VNEM coefficients caused by the difference of burnup distribution in a node.

A model is proposed and verified for NEACRP MOX BENCHMARKING assemblies by W. H. Beere and we have to complete it to be materialized.

2.2.4 Making VNEM Faster

The neutron transport equation of the VNEM form is a set of simultaneous linear equations that can be written in the form of a matrix eigenvalue problem. The equations are solved in VNEM module by the usual method of inner-outer iteration scheme. Where the outer iteration is the power method to calculate the maximum (in modulus) eigenvalue of given reactor core. The inner iteration is to calculate neutron fluxes for given neutron sources to a given energy group.

From the practical viewpoint, the computing time of a 3D core simulator for one state-point of a reactor core should be less than 20 minutes, while present version of VNEM module takes more than one hour.

To make the computing time shorter, we can:

1. Accelerate the convergence of the iterative scheme.
2. Tune the code.
3. Use faster hardware.

2.2.5 Built-in VNEM into 3D Core Simulator

CYGNUS is IFE's 3D LWR core simulation code based on a very simplified neutronics method. We will make a bypass of alternative neutronics method of VNEM in this code.

2.2.6 QA of VNEM

Though VNEM is based on the solution of rigorous neutron transport equations, it must be verified that it agrees well with actual plant data. In 2007 and 2008 comparisons were made by using plant data obtained from 2 PWRs. As VNEM code was just a transport equation solver (not including the calculation routines to estimate the feedback effects of the power density), the comparisons were made for the hot-stand-by cores at their beginning of life (BOL) where the feed back had no significance.

When we have finished implementing VNEM into CYGNUS, we can calculate the feedback effects and have to make comparisons for nearly all the static cases, including burnup.

Tables and Figures

Table 1.2.1 Fuel types.

Fuel type no.	Enrichment (%)	BP-type
1	2.11	0
3	2.6	12
4	2.6	16
5	2.6	20
6	3.1	0
7	3.1	12
8	3.1	16

Table 1.4.1 VNEM parameters.

Parameter	Value
Number of energy groups (g_{max})	7 *1
PL order (l_{max})	3 *1
Order of source expansion (nr_{max}) *2	5 *1
Order of boundary value expansion (sr_{max})	2 *1
Number of axial meshes / node (N)	4 *1
Axial mesh width in node $z_1 - z_0$ (cm)	0.272143 *1
Axial mesh width in node $z_2 - z_1$ (cm)	7.34786 *1
Axial mesh width in node $z_3 - z_2$ (cm)	7.34786 *1
Axial mesh width in node $z_4 - z_3$ (cm)	0.272143 *1

*1: Refer to the appendix A for the definition of there parameters

*2: The 2D Legendre polynomials used are

$$P_0(x, y) = P_0(x).P_0(y)$$
$$P_1(x, y) = P_1(x).P_0(y)$$
$$P_2(x, y) = P_0(x).P_1(y)$$
$$P_3(x, y) = P_1(x).P_1(y)$$
$$P_4(x, y) = P_2(x).P_0(y)$$
$$P_5(x, y) = P_0(x).P_2(y)$$

Table 1.5.1 Core eigenvalue (effective multiplication factor)

	VNEM-calculated keff	error (deviation from 1.0) in %
Case 1	0.99825	–0.175
Case 2	0.99978	–0.022
Case 3	0.99956	–0.044

Table 1.5.2 Maximum reading in core

	Measured	VNEM-calculated	error in %
Case 1	2.163	2.117	–2.1
Case 2	2.682	2.723	1.5
Case 3	2.763	2.748	–0.5

(j)								
1	6	6						
2	1	8	6	6				
3	3	1	4	7	6			
4	1	4	1	4	1	6		
5	5	1	4	1	4	7	6	
6	1	4	1	4	1	4	6	
7	5	1	4	1	4	1	8	6
8	1	5	1	5	1	3	1	6
	8	9	10	11	12	13	14	15 (i)

Fig.1.2.1 Loading pattern of fuel assemblies in the reactor core. The core is octant-symmetric.

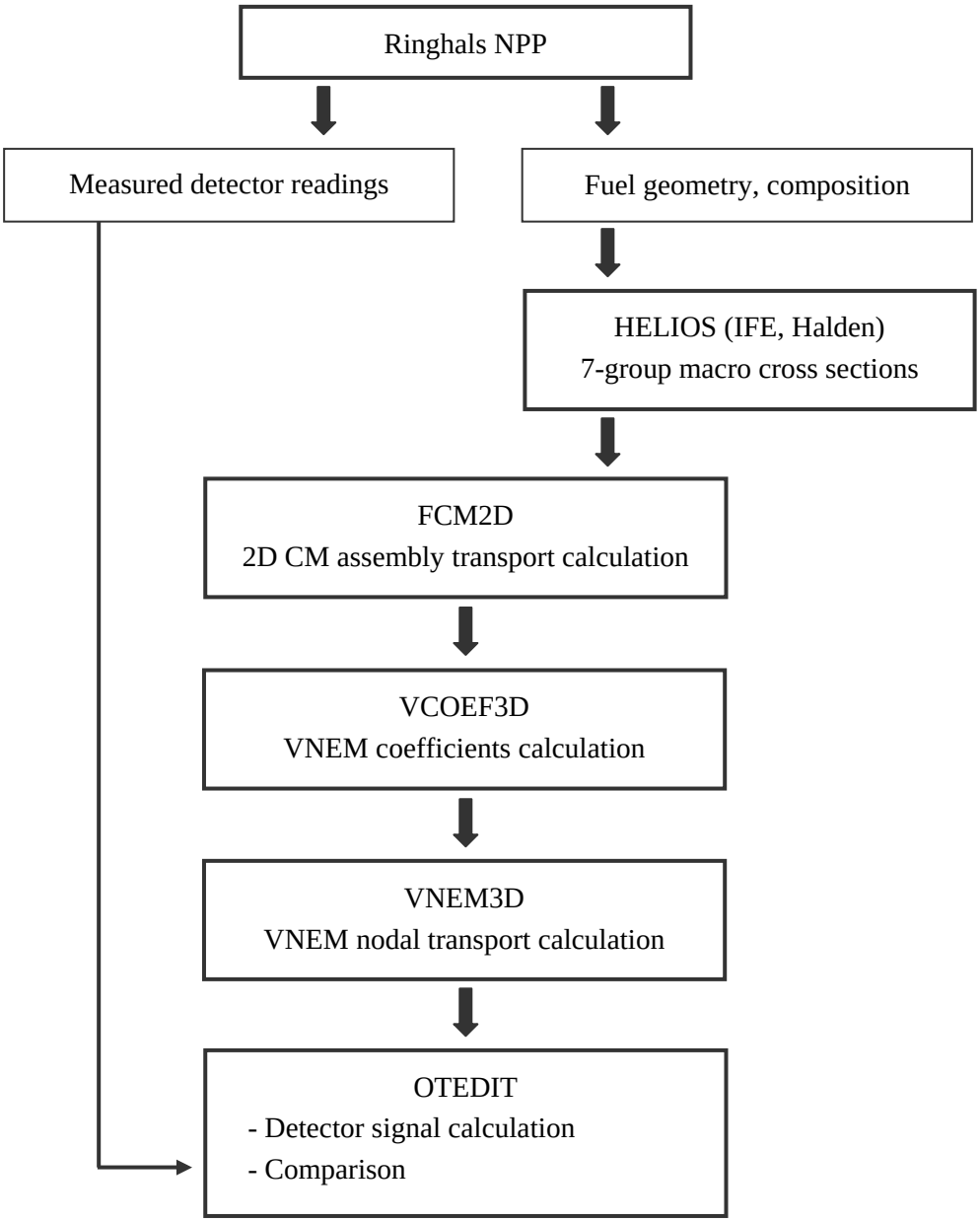

Fig.1.3.1 Flow diagram of comparison procedure of VNEM to Ringhals-3 plant data.

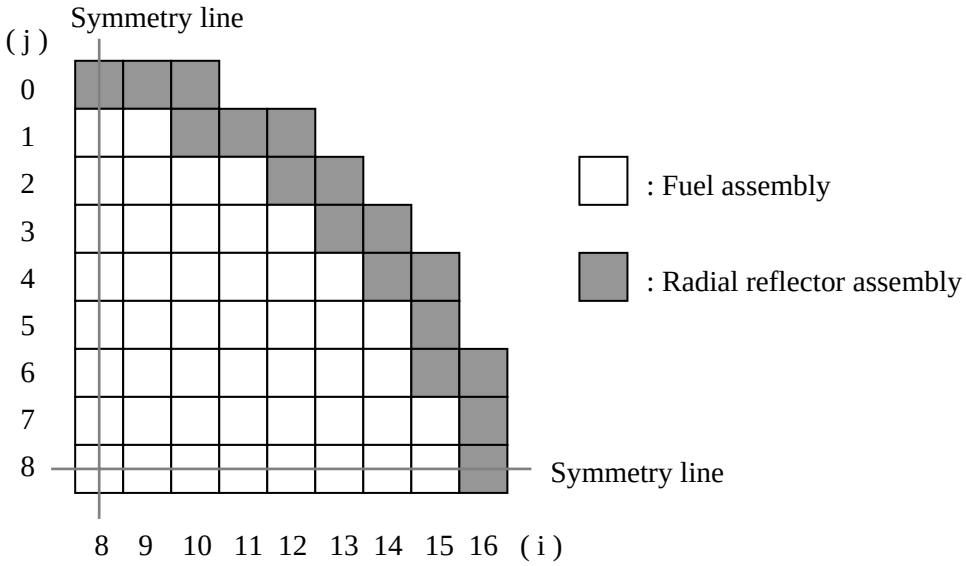

- 1 node / assembly in radial direction
- The size of radial reflector assembly = the size of fuel assembly
- zero flux boundary condition at the outer boundary of radial reflectors

(a) Radial view

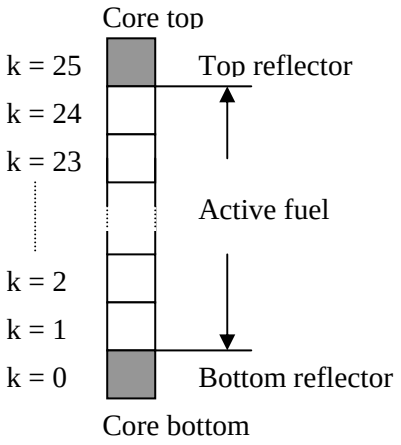

- 24 nodes / active fuel in axial direction
- The size of axial reflector node = the size of fuel-assembly node
- zero flux boundary condition at the outer boundary of axial reflectors
- Active fuel is replaced by radial reflector for the radial reflector assembly

(b) Axial view

Height of active fuel = 365.76 cm
Width of fuel assembly = width of node = 21.42 cm
Height of node = 365.76 / 24 = 15.24 cm

Fig.1.4.1 Core geometry modelling

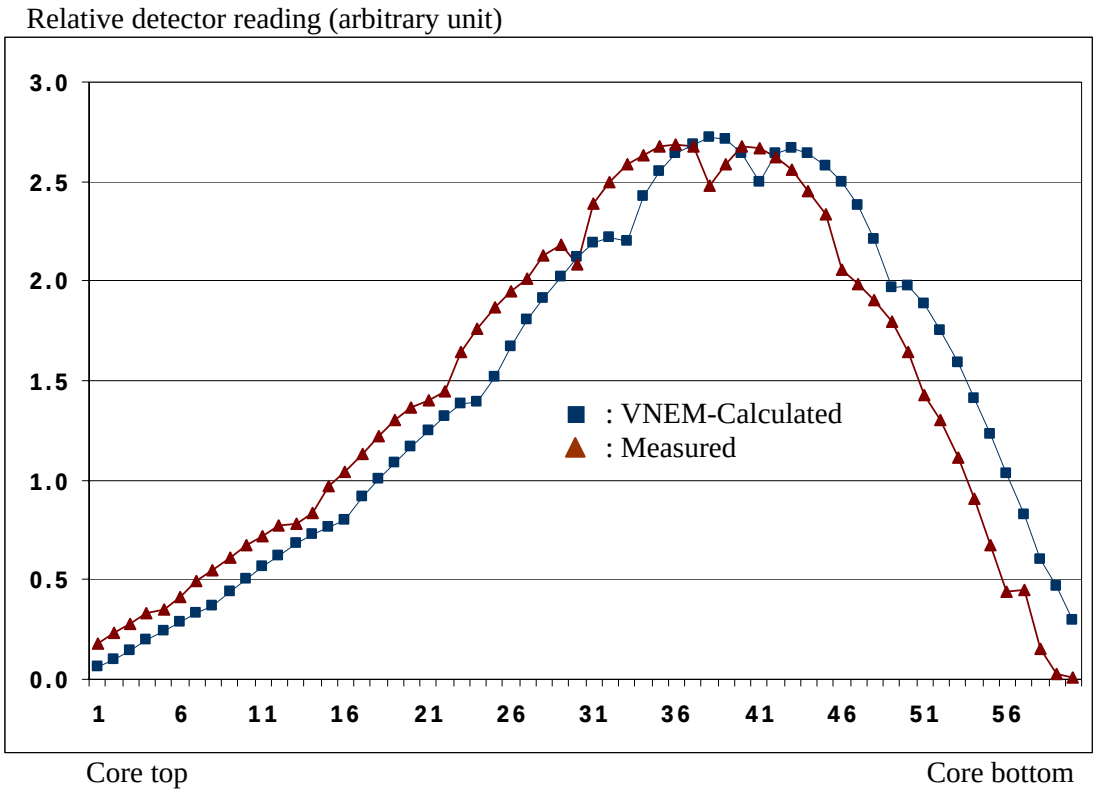

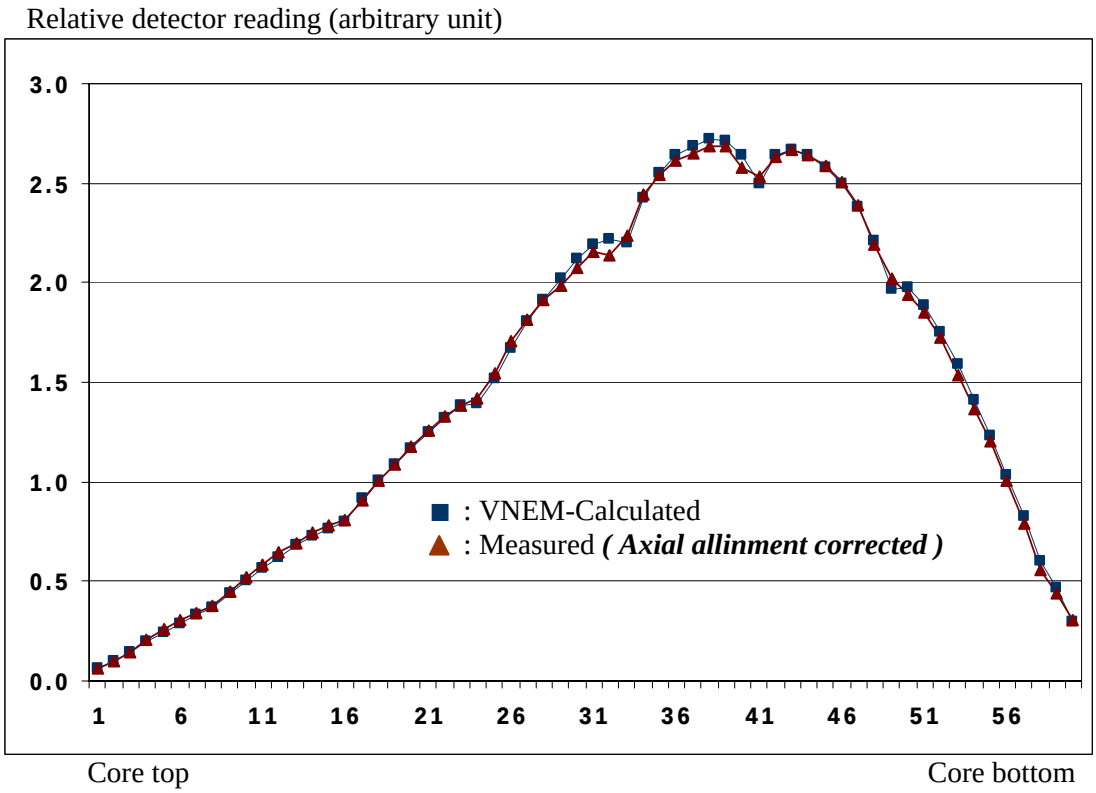

Fig.1.4.1 Misalignment correction of the measured readings.

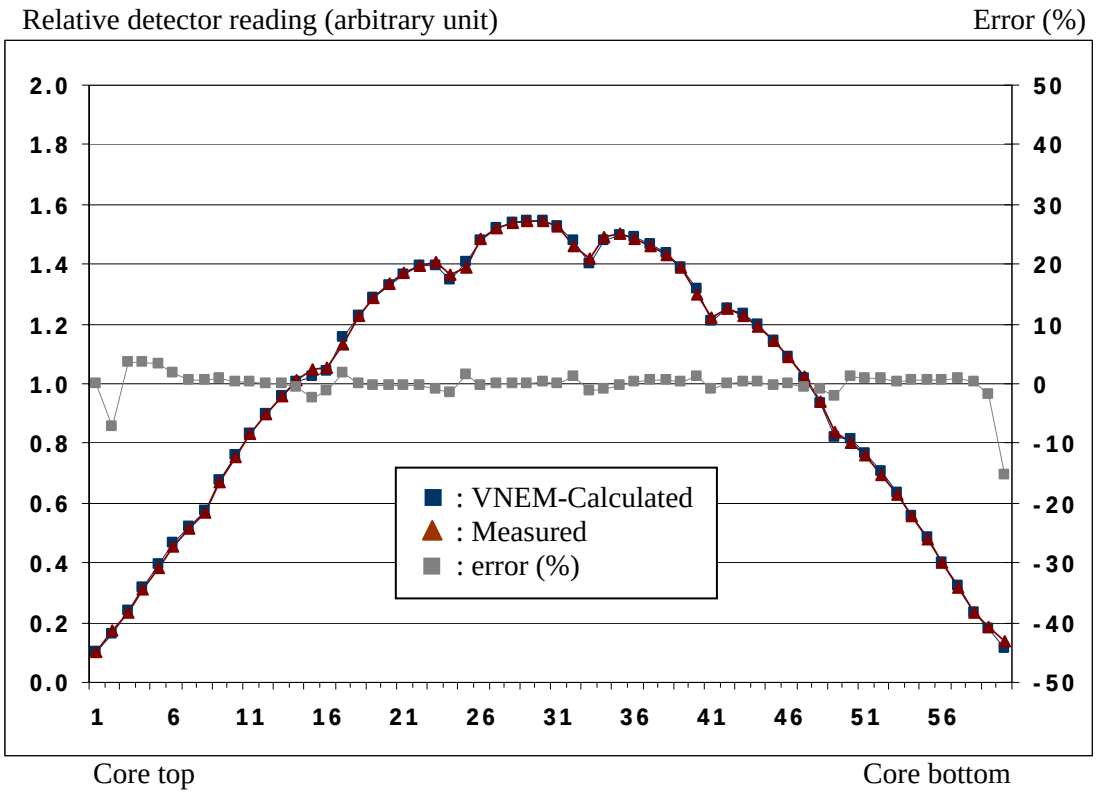

Fig.1.5.1 Comparison of core average axial detector readings, Case 1.
The readings are relative to their average.

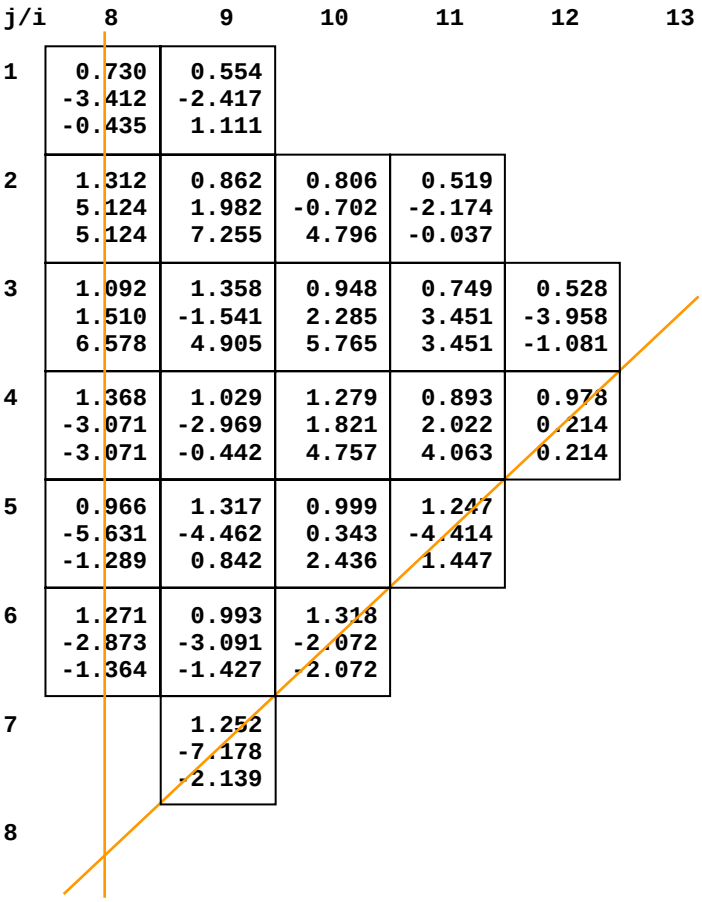

j/i	8	9	10	11	12	13	14
1	0.730 -3.412 -0.435	0.554 -2.417 1.111					
2	1.312 5.124 5.124	0.862 1.982 7.255	0.806 -0.702 4.796	0.519 -2.174 -0.037			
3	1.092 1.510 6.578	1.358 -1.541 4.905	0.948 2.285 5.765	0.749 3.451 3.451	0.528 -3.958 -1.081		
4	1.368 -3.071 -3.071	1.029 -2.969 -0.442	1.279 1.821 4.757	0.893 2.022 4.063	0.978 0.214 0.214		
5	0.966 -5.631 -1.289	1.317 -4.462 0.842	0.999 0.343 2.436	1.247 -4.414 1.447			
6	1.271 -2.873 -1.364	0.993 -3.091 -1.427	1.318 -2.072 -2.072				
7		1.252 -7.178 -2.139					
8							

Octant symmetry lines

Fig.1.5.2 Comparison of assembly average radial detector readings, Case 1. The readings are relative to their average.

Line 1: Calculated reading by VNEM
Line 2: VNEM – Upper bound of measured in %
Line 3: VNEM – Lower bound of measured in %

The upper and the lower bounds are taken from the maximum and the minimum readings of assemblies at octant-symmtric positions.

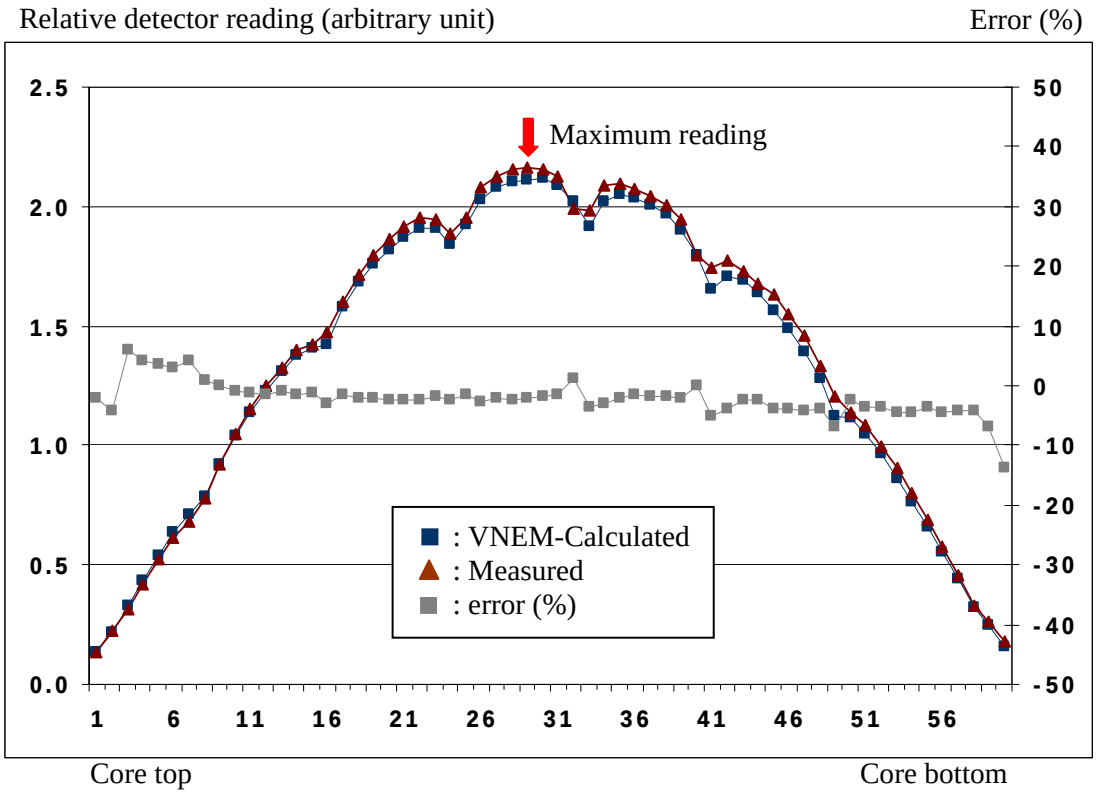

Fig.1.5.3 Comparison of detector readings in assembly H4 (i = 8, j = 4, see Fig.1.5.2 for the assembly position in the core), where the maximum reading is observed in Case 1.

The readings are relative to their average over all the measured positions in the core.

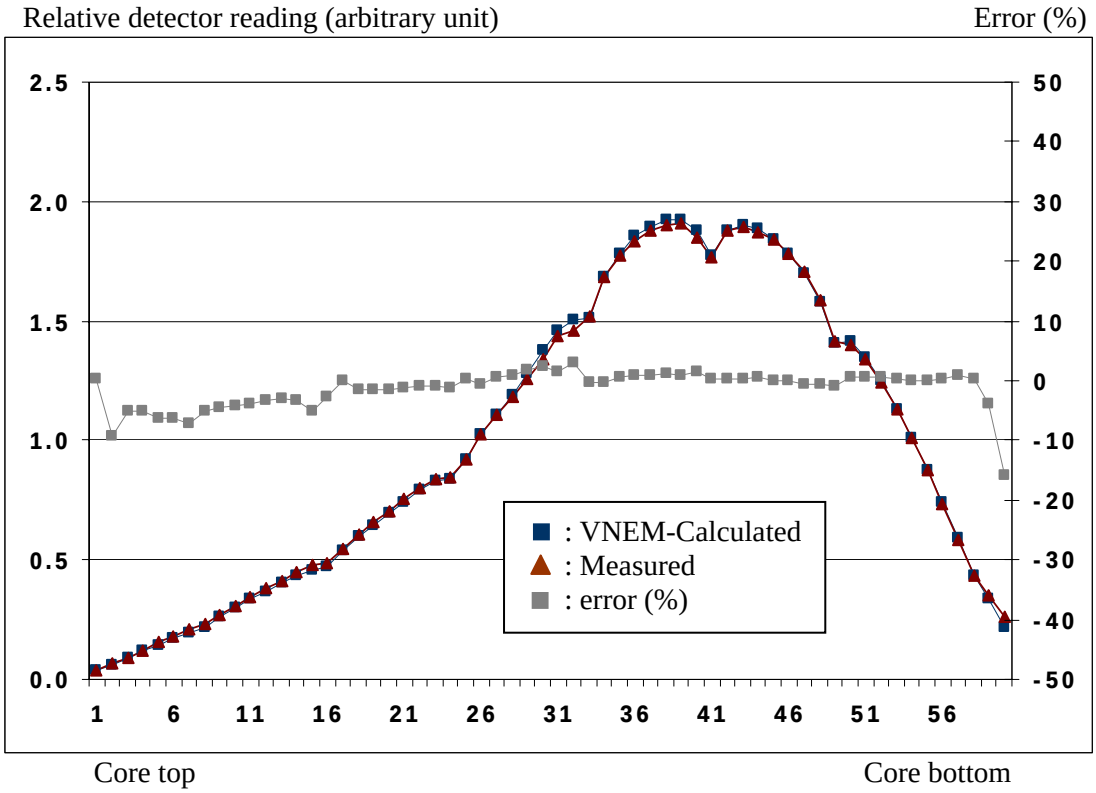

Fig.1.5.4 Comparison of core average axial detector readings, Case 2.
The readings are relative to their average.

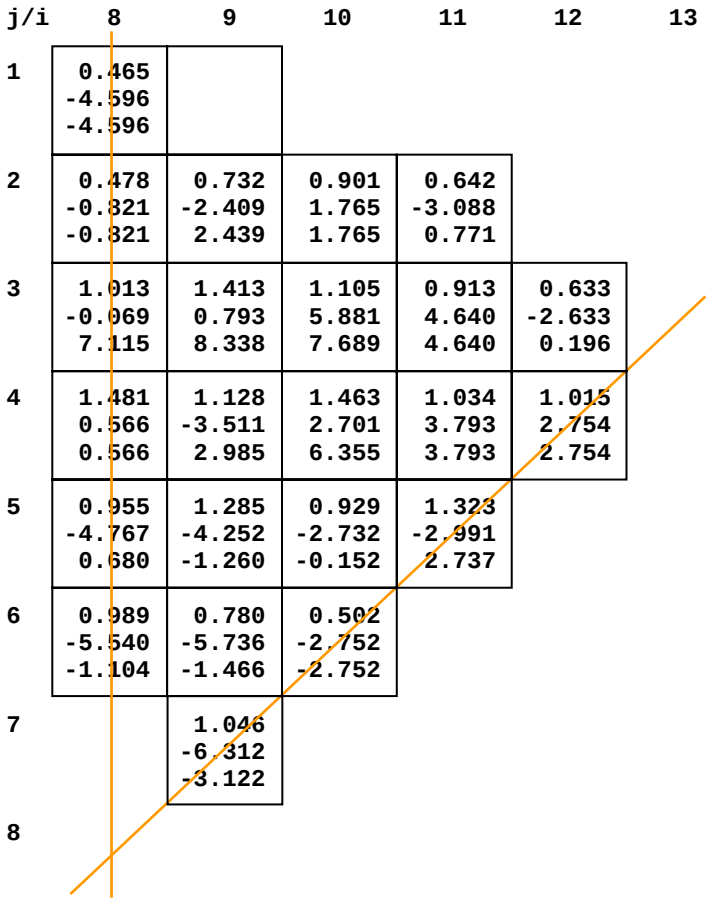

j/i	8	9	10	11	12	13	14
1	0.465 -4.596 -4.596						
2	0.478 -0.321 -0.321	0.732 -2.409 2.439	0.901 1.765 1.765	0.642 -3.088 0.771			
3	1.013 -0.069 7.115	1.413 0.793 8.338	1.105 5.881 7.689	0.913 4.640 4.640	0.633 -2.633 0.196		
4	1.481 0.566 0.566	1.128 -3.511 2.985	1.463 2.701 6.355	1.034 3.793 3.793	1.015 2.754 2.754		
5	0.955 -4.767 0.680	1.285 -4.252 -1.260	0.929 -2.732 -0.152	1.323 -2.991 2.737			
6	0.989 -5.540 -1.104	0.780 -5.736 -1.466	0.502 -2.752 -2.752				
7		1.046 -6.312 -3.122					
8							

Octant symmetry lines

Fig.1.5.5 Comparison of assembly average radial detector readings, Case 2. The readings are relative to their average.

Line 1: Calculated reading by VNEM
Line 2: VNEM – Upper bound of measured in %
Line 3: VNEM – Lower bound of measured in %

The upper and the lower bounds are taken from the maximum and the minimum readings of assemblies at octant-symmtric positions.

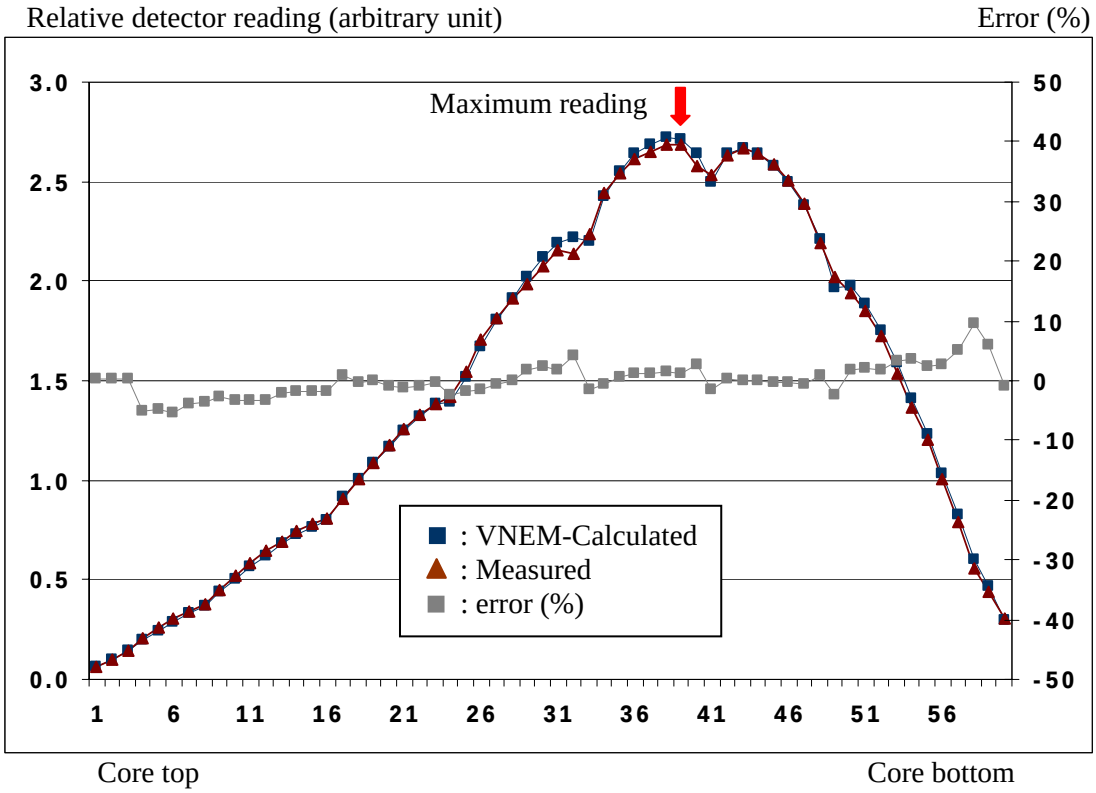

Fig.1.5.6 Comparison of detector readings in assembly H4 (i = 8, j = 4, see Fig.1.5.5 for the assembly position in the core), where the maximum reading is observed in Case 2.

The readings are relative to their average over all the measured positions in the core.

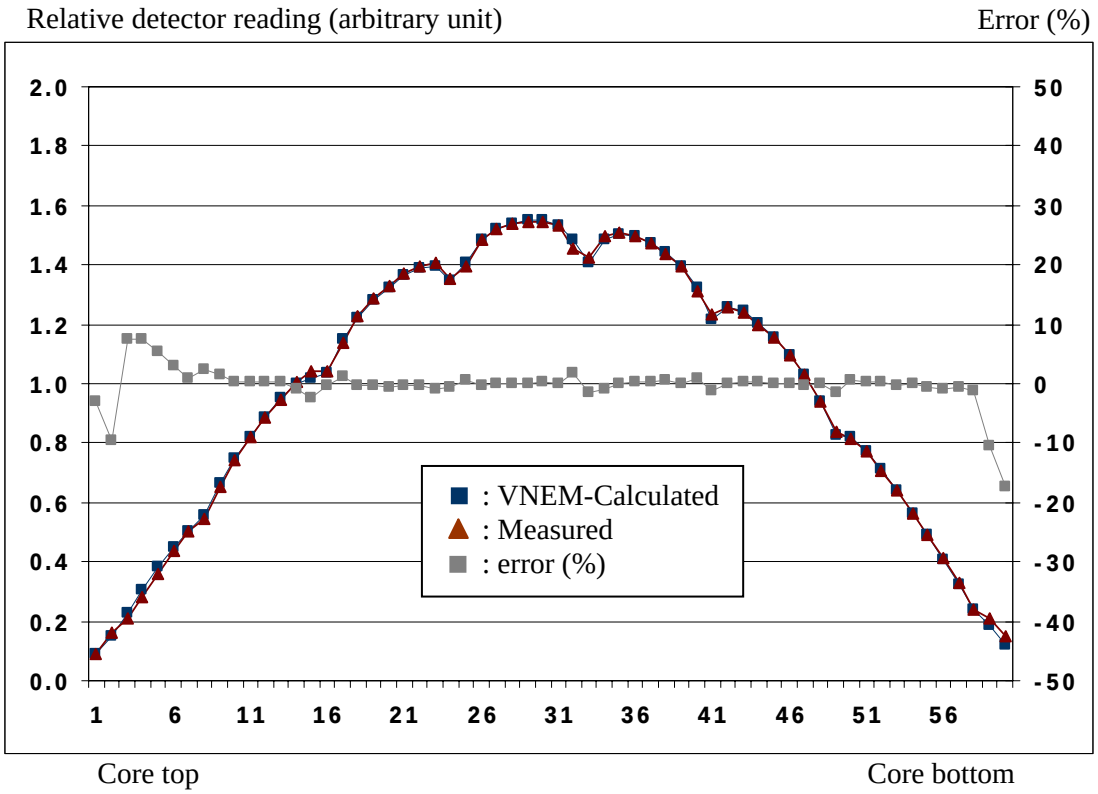

Fig.1.5.7 Comparison of core average axial detector readings, Case 3.
The readings are relative to their average.

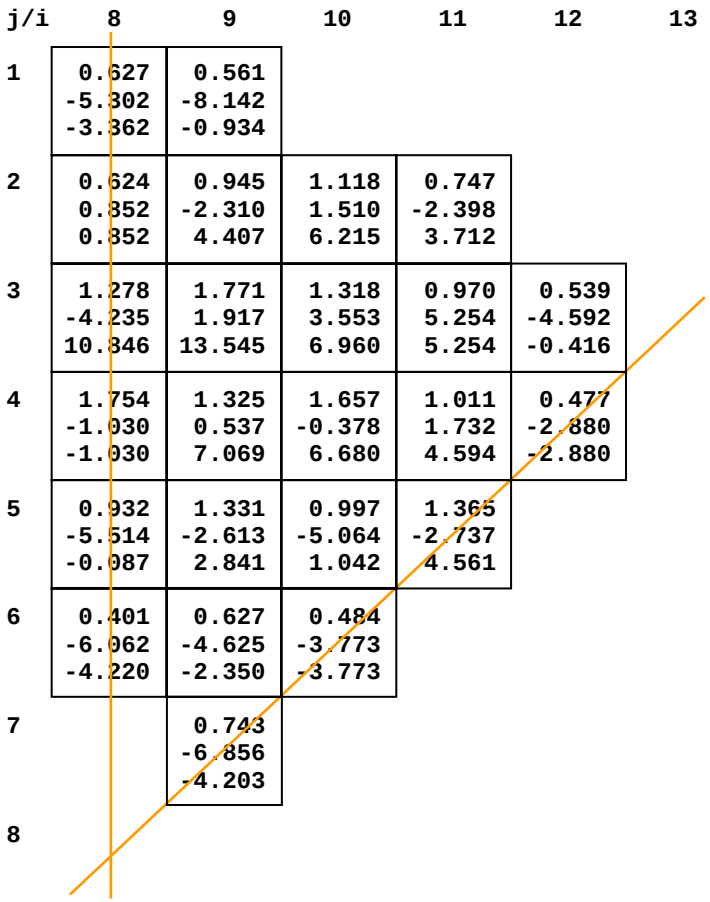

j/i	8	9	10	11	12	13	14
1	0.627 -5.302 -3.362	0.561 -8.142 -0.934					
2	0.624 0.852 0.852	0.945 -2.310 4.407	1.118 1.510 6.215	0.747 -2.398 3.712			
3	1.278 -4.235 10.846	1.771 1.917 13.545	1.318 3.553 6.960	0.970 5.254 5.254	0.539 -4.592 -0.416		
4	1.754 -1.030 -1.030	1.325 0.537 7.069	1.657 -0.378 6.680	1.011 1.732 4.594	0.477 -2.880 -2.880		
5	0.932 -5.514 -0.087	1.331 -2.613 2.841	0.997 -5.064 1.042	1.365 -2.737 4.561			
6	0.401 -6.062 -4.220	0.627 -4.625 -2.350	0.484 -3.773 -3.773				
7		0.743 -6.856 -4.203					
8							

Octant symmetry lines

Fig.1.5.8 Comparison of assembly average radial detector readings, Case 3. The readings are relative to their average.

Line 1: Calculated reading by VNEM
Line 2: VNEM – Upper bound of measured in %
Line 3: VNEM – Lower bound of measured in %

The upper and the lower bounds are taken from the maximum and the minimum readings of assemblies at octant-symmtric positions.

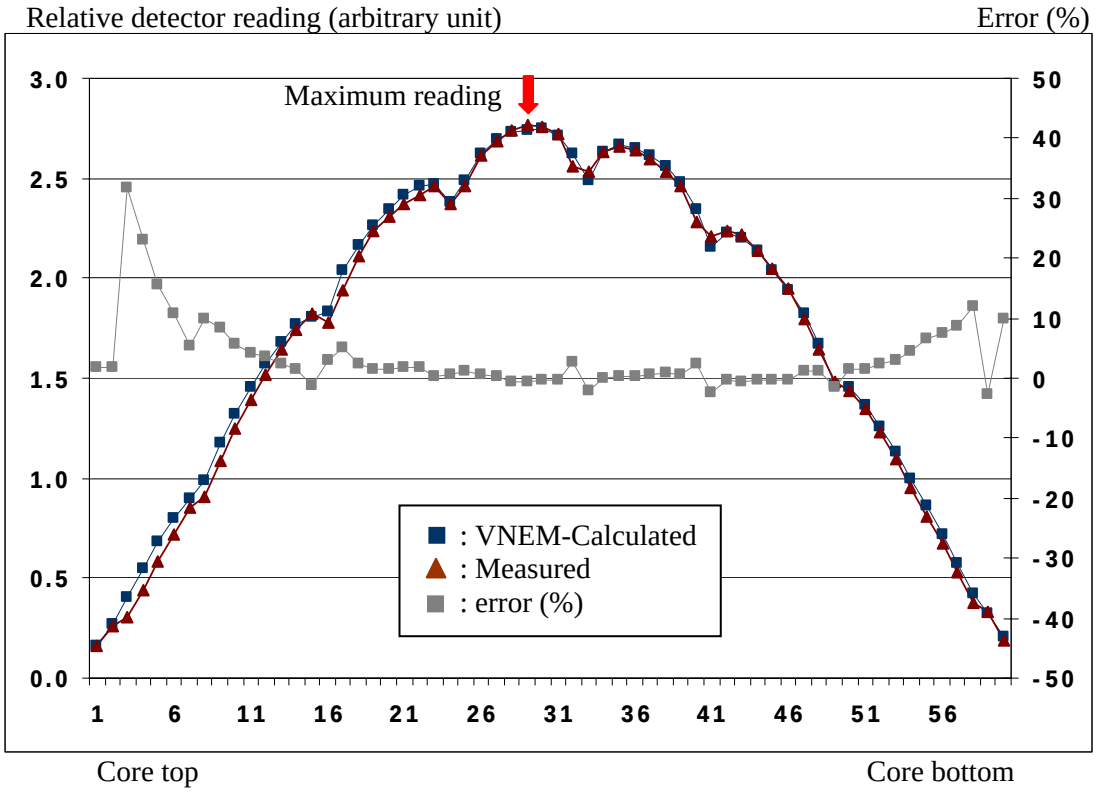

Fig.1.5.9 Comparison of detector readings in assembly J3 (i = 7, j = 3, which is equivalent to i = 9, j = 3, see Fig.1.5.8 for the assembly position in the core), where the maximum reading is observed in Case 3.

The readings are relative to their average over all the measured positions in the core.

Appendix A: Mathematical Method of VNEM3D

A.1 Synthetic Flux Moment Expansion

We first assume that we can expand the g-th group neutron flux moment $\phi_{l,\,m,\,g}(\mathbf{r})$ for the angular index (l, m) at spatial position $\mathbf{r}$ = (x, y, z) as:

$$\begin{aligned}\phi_{l,\,m,\,g}(\mathbf{r}) = &\sum_{nr,\,nz} F^{S}_{nr,\,nz,\,g}\,\varphi^{S}_{nr,\,l,\,m,\,g}(x,\,y)\,Rz_{nz}(z)\\ &+\sum_{pp}\sum_{il,\,im,\,sr,\,nz} F^{CB}_{pp,\,il,\,im,\,sr,\,nz,\,g}\,\varphi^{CB}_{pp,\,il,\,im,\,sr,\,l,\,m,\,g}(x,\,y)\,Rz_{nz}(z)\\ &+\sum_{pp}\sum_{il,\,im,\,sr,\,nz} F^{SB}_{pp,\,il,\,im,\,sr,\,nz,\,g}\,\varphi^{SB}_{pp,\,il,\,im,\,sr,\,l,\,m,\,g}(x,\,y)\,Rz_{nz}(z)\end{aligned} \tag{A.1.1}$$

where

$F^{S}_{nr,\,nz,\,g}$: source expansion coefficient (SEC)
$F^{CB}_{pp,\,il,\,im,\,sr,\,nz,\,g}$: real boundary value expansion coefficient (BVEC)
$F^{SB}_{pp,\,il,\,im,\,sr,\,nz,\,g}$: imaginary BVEC

are the expansion coefficients to be calculated by global core calculation of VNEM3D. The functions

$\varphi^{S}_{nr,\,l,\,m,\,g}(x,\,y)$: source expansion function (SEF)
$\varphi^{CB}_{pp,\,il,\,im,\,sr,\,l,\,m,\,g}(x,\,y)$: real boundary value expansion function (BVEF)
$\varphi^{SB}_{pp,\,il,\,im,\,sr,\,l,\,m,\,g}(x,\,y)$: imaginary BVEF

are the expansion functions obtained by 2-dimensional (2D) single assembly calculations. Their detailed definitions will be given later.

The subscripts are:

- nr : degree of 2-dimensional Legendre polynomial for radial source expansion
- nz : axial mesh index to define 1-dimensional (1D) tent functions for axial moment expansion
- pp : indexing of the 4 radial interfaces of the node, pp = XL (west), XR (east), YL (south), and YR (north) interfaces, respectively
- il : the angular l-index of the boundary value
- im : the angular m-index of the boundary value
- sr : degree of 1D Legendre polynomial for radial boundary value expansion along x- or y-direction

and the superscripts mean:

- S : source expansion coefficient, or function
- CB : radial boundary value expansion coefficient, or function, real part
- SB : radial boundary value expansion coefficient, or function, imaginary part

and the spatial position $\mathbf{r}$ = (x, y, z), the angular indices l and il = 0, 2, ..., m and im = 0, 2, ..., l. Note that we neglected moments with odd m indices because it has been observed that the contributions of them are several orders smaller than the even components.

The height of a node $z \in [\, z_0 , z_N \,]$ is divided by mesh points z_{nz} (nz = 0, 1, 2, ..., N), and the tent function $Rz_{nz}(z)$ is defined by

$$Rz_{nz}(z) = 1 \text{ at } z = z_{nz}$$
$$Rz_{nz}(z) = 1.0 - (z_{nz} - z) / (z_{nz} - z_{nz-1}) \quad \text{for } z = [\, z_{nz-1} , z_{nz} \,] \text{ and } nz \geq 1$$
$$Rz_{nz}(z) = 1.0 - (z - z_{nz}) / (z_{nz+1} - z_{nz}) \quad \text{for } z = [\, z_{nz} , z_{nz+1} \,] \text{ and } nz \leq N \qquad \text{(A.1.2)}$$

In this expansion the axial shape of the flux moments are approximated by a piecewise linear function.

A.2 Variational Derivation of Equations for Source Expansion Coefficients

The source expansion coefficient $F^S_{nr, nz, g}$ is determined from a variational principle (the Ritz method). The real part of the functional to be minimized is, for **r** = (x, y, z):

$$\begin{aligned} F^c_{l, m, g} [\phi^c_{l, m, g}] \\ \equiv \int_{core} d\mathbf{r} \{ & \quad aabb1_{l, m, g}(\mathbf{r}) \quad [\, \partial/\partial x \, \phi^c_{l, m, g}(\mathbf{r}) \,]^2 \\ & + aabb1_{l, m, g}(\mathbf{r}) \quad [\, \partial/\partial y \, \phi^c_{l, m, g}(\mathbf{r}) \,]^2 \\ & + egge_{l, m, g}(\mathbf{r}) \quad [\, \partial/\partial z \, \phi^c_{l, m, g}(\mathbf{r}) \,]^2 \\ & + \Sigma_g(\mathbf{r}) \, \phi^c_{l, m, g}(\mathbf{r})^2 - 2 \, Q^c_{l, m, g}(\mathbf{r}) \, \phi^c_{l, m, g}(\mathbf{r}) \, \} \end{aligned} \qquad \text{(A.2.1)}$$

The imaginary part is:

$$\begin{aligned} F^s_{l, m, g} [\phi^s_{l, m, g}] \\ \equiv \int_{core} d\mathbf{r} \{ & \quad aabb1_{l, m, g}(\mathbf{r}) \quad [\, \partial/\partial x \, \phi^s_{l, m, g}(\mathbf{r}) \,]^2 \\ & + aabb1_{l, m, g}(\mathbf{r}) \quad [\, \partial/\partial y \, \phi^s_{l, m, g}(\mathbf{r}) \,]^2 \\ & + egge_{l, m, g}(\mathbf{r}) \quad [\, \partial/\partial z \, \phi^s_{l, m, g}(\mathbf{r}) \,]^2 \\ & + \Sigma_g(\mathbf{r}) \, \phi^s_{l, m, g}(\mathbf{r})^2 - 2 \, Q^s_{l, m, g}(\mathbf{r}) \, \phi^s_{l, m, g}(\mathbf{r}) \, \} \end{aligned} \qquad \text{(A.2.2)}$$

The overall functional is defined by:

$$\begin{aligned} F[\phi] \equiv & \sum_g \sum_{l = 0, L, \text{even}} \sum_{m = 0, l} F^c_{l, m, g} [\phi^c_{l, m, g}] \\ & + \sum_g \sum_{l = 2, L, \text{even}} \sum_{m = 1, l} F^s_{l, m, g} [\phi^s_{l, m, g}] \end{aligned} \qquad \text{(A.2.3)}$$

where $\phi^c_{l, m, g}$ and $\phi^s_{l, m, g}$ are the real and the imaginary parts of $\phi_{l, m, g}$, and

$$\phi = \{ [\phi^c_{l, m, g} ; l = 0, L, \text{even}, m = 0, l \,], [\phi^s_{l, m, g} ; l = 2, L, \text{even}, m = 1, l \,] \} \qquad \text{(A.2.4)}$$
$$egge_{l, m, g}(\mathbf{r}) \equiv eg_{l, m; l+1, m, g}(\mathbf{r}) + ge_{l, m; l-1, m, g}(\mathbf{r}) \qquad \text{(A.2.5)}$$
$$eg_{l, m; l', m', g}(\mathbf{r}) = T_g(\mathbf{r}) \; \eta_{l, m} \; \gamma_{l', m'} \qquad \text{(A.2.6)}$$
$$ge_{l, m; l', m', g}(\mathbf{r}) = T_g(\mathbf{r}) \; \gamma_{l, m} \; \eta_{l', m'} \qquad \text{(A.2.7)}$$
$$\eta_{l, m} = [\, (l + m + 1) (l - m + 1) \,]^{1/2} / (2 l + 1) \qquad \text{(A.2.8)}$$
$$\gamma_{l, m} = [\, (l + m) (l - m) \,]^{1/2} / (2 l + 1) \qquad \text{(A.2.9)}$$
$$T_g(\mathbf{r}) = 1 / \Sigma_g(\mathbf{r}) \qquad \text{(A.2.10)}$$
$$aabb1_{l, m, g}(\mathbf{r}) = T_g(\mathbf{r}) (\alpha_{l, m+1} \alpha_{l+1, m} + \beta_{l, m-1} \beta_{l+1, m}$$

$$+ \beta_{l,\,m+1}\,\beta_{l-1,\,m} + \alpha_{l,\,m-1}\,\alpha_{l-1,\,m}) \qquad \text{(A.2.11)}$$

$$\alpha_{l,\,m} = [\,(l+m)\,(l+m+1)\,]^{1/2} / 2 / (2\,l+1) \qquad \text{(A.2.12)}$$

$$\beta_{l,\,m} = \alpha_{l,\,-m} \qquad \text{(A.2.13)}$$

$\Sigma_g(\mathbf{r})$ is the g-th group total cross section.

By variational method, if one substitute the expansion (A.1.1) into the overall functional (A.2.3), and differentiate the result with respect to the source expansion coefficient $F^S_{nr,\,nz,\,g}$, one obtains, for each of all the parameters g, nr, and for nz = 1, 2, ..., N – 1.

$$\begin{aligned}
&\sum_{nr',nz'} F^S_{nr',\,nz',\,g}\,(\,ANN_{nr,\,nr';\,g}\,RzRz_{nz,\,nz'} + ANN20_{nr,\,nr';\,g}\,RzzRzz_{nz,\,nz'} \\
&\qquad + ANN00_{nr,\,nr';\,g}\,RzzRzz_{nz,\,nz'}\,) \\
&+ \sum_{pp,\,lmcq,\,nz'} F^{CB}_{pp,\,lmcq,\,nz',\,g}\,(\,ANC20_{nr,\,pp,\,lmcq;\,g}\,RzzRzz_{nz,\,nz'} \\
&\qquad + ANC00_{nr,\,pp,\,lmcq;\,g}\,RzzRzz_{nz,\,nz'}\,) \\
&+ \sum_{pp,\,lmsq,\,nz'} F^{SB}_{pp,\,lmsq,\,nz',\,g}\,(\,ANS20_{nr,\,pp,\,lmsq;\,g}\,RzzRzz_{nz,nz'} \\
&\qquad + ANS00_{nr,\,pp,\,lmsq;\,g}\,RzzRzz_{nz,nz'}\,) \\
=\ &\sum_{g'}\,(\,\sum_{nr',\,nz'} F^S_{nr',\,nz',\,g'}\,ANNS_{nr,\,nr';\,g,\,g'}\,RzRz_{nz,nz'} \\
&+ \sum_{pp,\,lmcq,\,nz'} F^{CB}_{pp,\,lmcq,\,nz',\,g'}\,ANCS_{nr,\,pp,\,lmcq;\,g,\,g'}\,RzRz_{nz,\,nz'} \\
&+ \sum_{pp,\,lmsq,\,nz'} F^{SB}_{pp,\,lmsq,\,nz',\,g'}\,ANSS_{nr,\,pp,\,lmsq;\,g,\,g'}\,RzRz_{nz,\,nz'}\,) \\
&+ (\,1/\lambda\,)\,\chi_g\,\sum_{g'}\,(\,\sum_{nr',\,nz'} F^S_{nr',\,nz',\,g'}\,ANNF_{nr,\,nr';\,g,\,g'}\,RzRz_{nz,nz'} \\
&\qquad + \sum_{pp,\,lmcq,\,nz'} F^{CB}_{pp,\,lmcq,\,nz',\,g'}\,ANCF_{nr,\,pp,\,lmcq;\,g,\,g'}\,RzRz_{nz,\,nz'} \\
&\qquad + \sum_{pp,\,lmsq,\,nz'} F^{SB}_{pp,\,lmsq,\,nz',\,g'}\,ANSF_{nr,\,pp,\,lmsq;\,g,\,g'}\,RzRz_{nz,\,nz'}\,)
\end{aligned} \qquad \text{(A.2.14)}$$

for each of the combination of indices (nr, nz, g). The index lmcq = (il, im, sr) for the real boundary expansion function: $\varphi^{CB}_{pp,\,il,\,im,\,sr,\,l,\,m,\,g}(x, y)$, and lmsq = (il, im, sr) for the imaginary boundary expansion function: $\varphi^{SB}_{pp,\,il,\,im,\,sr,\,l,\,m,\,g}(x, y)$, respectively, λ is the core eigenvalue, and χ_g is the fission neutron spectrum.

The coefficients of Eq.(A.2.14) are defined by:

$$ANN_{nr,\,nr';\,g} = \int_{node} dr\ \varphi^S_{nr,\,l=0,\,m=0,\,g}(\mathbf{r})\ S^{\infty}_g(\mathbf{r})\ P_{nr'}(\mathbf{r}) \qquad \text{(A.2.15)}$$

$$ANN20_{nr,\,nr';\,g} = -2/3 \int_{node} dr\ \varphi^S_{nr,\,l=0,\,m=0,\,g}(\mathbf{r})\ T_g(\mathbf{r})\ \varphi^S_{nr',\,l=2,\,m=0,\,g}(\mathbf{r}) \qquad \text{(A.2.16)}$$

$$ANN00_{nr,\,nr';\,g} = -1/3 \int_{node} dr\ \varphi^S_{nr,\,l=0,\,m=0,\,g}(\mathbf{r})\ T_g(\mathbf{r})\ \varphi^S_{nr',\,l=0,\,m=0,\,g}(\mathbf{r}) \qquad \text{(A.2.17)}$$

$$ANC20_{nr,\,pp,\,lmcq;\,g} = -2/3 \int_{node} dr\ \varphi^S_{nr,\,l=0,\,m=0,\,g}(\mathbf{r})\ T_g(\mathbf{r})\ \varphi^{CB}_{pp,\,lmcq,\,l=2,\,m=0,\,g}(\mathbf{r}) \qquad \text{(A.2.18)}$$

$$ANC00_{nr,\,pp,\,lmcq;\,g} = -1/3 \int_{node} dr\ \varphi^S_{nr,\,l=0,\,m=0,\,g}(\mathbf{r})\ T_g(\mathbf{r})\ \varphi^{CB}_{pp,\,lmcq,\,l=0,\,m=0,\,g}(\mathbf{r}) \qquad \text{(A.2.19)}$$

$$ANS20_{nr,\,pp,\,lmsq;\,g} = -2/3 \int_{node} dr\ \varphi^S_{nr,\,l=0,\,m=0,\,g}(\mathbf{r})\ T_g(\mathbf{r})\ \varphi^{SB}_{pp,\,lmsq,\,l=2,\,m=0,\,g}(\mathbf{r}) \qquad \text{(A.2.20)}$$

$$ANS00_{nr,\,pp,\,lmsq;\,g} = -1/3 \int_{node} dr\ \varphi^S_{nr,\,l=0,\,m=0,\,g}(\mathbf{r})\ T_g(\mathbf{r})\ \varphi^{SB}_{pp,\,lmsq,\,l=0,\,m=0,\,g}(\mathbf{r}) \qquad \text{(A.2.21)}$$

$$ANNS_{nr,\,nr';\,g,\,g'} = \int_{node} dr\ \varphi^S_{nr,\,l=0,\,m=0,\,g}(\mathbf{r})\ \Sigma_{g,\,g'}(\mathbf{r})\ \varphi^S_{nr',\,l=0,\,m=0,\,g'}(\mathbf{r}) \qquad \text{(A.2.22)}$$

$$ANCS_{nr,\,pp,\,lmcq;\,g,\,g'} = \int_{node} dr\ \varphi^{S}_{nr,\,l=0,\,m=0,\,g}(\mathbf{r})\ \Sigma_{g,\,g'}(\mathbf{r})\ \varphi^{CB}_{pp,\,lmcq,\,l=0,\,m=0,\,g'}(\mathbf{r}) \quad \text{(A.2.23)}$$

$$ANSS_{nr,\,pp,\,lmsq;\,g,\,g'} = \int_{node} dr\ \varphi^{S}_{nr,\,l=0,\,m=0,\,g}(\mathbf{r})\ \Sigma_{g,\,g'}(\mathbf{r})\ \varphi^{SB}_{pp,\,lmsq,\,l=0,\,m=0,\,g'}(\mathbf{r}) \quad \text{(A.2.24)}$$

$$ANNF_{nr,\,nr';\,g,\,g'} = \int_{node} dr\ \varphi^{S}_{nr,\,l=0,\,m=0,\,g}(\mathbf{r})\ \nu\Sigma f_{g'}(\mathbf{r})\ \varphi^{S}_{nr',\,l=0,\,m=0,\,g'}(\mathbf{r}) \quad \text{(A.2.25)}$$

$$ANCF_{nr,\,pp,\,lmcq;\,g,\,g'} = \int_{node} dr\ \varphi^{S}_{nr,\,l=0,\,m=0,\,g}(\mathbf{r})\ \nu\Sigma f_{g'}(\mathbf{r})\ \varphi^{CB}_{pp,\,lmcq,\,l=0,\,m=0,\,g'}(\mathbf{r}) \quad \text{(A.2.26)}$$

$$ANSF_{nr,\,pp,\,lmsq;\,g,\,g'} = \int_{node} dr\ \varphi^{S}_{nr,\,l=0,\,m=0,\,g}(\mathbf{r})\ \nu\Sigma f_{g'}(\mathbf{r})\ \varphi^{SB}_{pp,\,lmsq,\,l=0,\,m=0,\,g'}(\mathbf{r}) \quad \text{(A.2.27)}$$

$$\begin{aligned} RzRz_{nz,\,nz'} &= 1/6\,(z_{nz} - z_{nz-1}), && \text{if } nz' = nz - 1 \\ &= 1/3\,(z_{nz+1} - z_{nz-1}), && \text{if } nz' = nz \\ &= 1/6\,(z_{nz+1} - z_{nz}), && \text{if } nz' = nz + 1 \\ &= 0 && \text{otherwise} \end{aligned} \quad \text{(A.2.28)}$$

$$\begin{aligned} RzzRzz_{nz,\,nz'} &= 1/(z_{nz} - z_{nz-1}), && \text{if } nz' = nz - 1 \\ &= -1/(z_{nz} - z_{nz-1}) - 1/(z_{nz+1} - z_{nz}), && \text{if } nz' = nz \\ &= 1/(z_{nz+1} - z_{nz}), && \text{if } nz' = nz + 1 \\ &= 0 && \text{otherweise} \end{aligned} \quad \text{(A.2.29)}$$

where in these definitions $\mathbf{r} = (x, y)$, $\int_{node} dr$ is the integration over radial volume of a node, $P_{nr}(\mathbf{r})$ is the 2D Legendre polynomial of order nr, $S^{\infty}_{g}(\mathbf{r})$ is the infinite-lattice source for g-th group, $\Sigma_{g,\,g'}(\mathbf{r})$ is group transfer (from g' to g by scattering) cross section, and $\nu\Sigma f_{g}(\mathbf{r})$ is the fission cross section multiplied by the number of neutrons generated in a fission.

From Eqs.(A.2.28 - 29) it can be seen that Eq.(A.2.14) is of the same form as the 3-point finite-difference equation in axial (z) direction. The top and bottom coefficients ($F^{S}_{nr',\,nz',\,g'}$ for nz = 0 and nz = N) are not included in Eq.(A.2.14) and are determined by the continuity condition in the axial direction (see Section A.4).

A.3 Continuity Condition at Radial Node Interface

The boundary value expansion coefficients $F^{CB}_{pp,\,lmcq,\,nz,\,g}$ and $F^{SB}_{pp,\,lmsq,\,nz,\,g}$ are determined by the continuity condition of the neutron angular current moments (this is equivalent to the current continuity in the case of the diffusion theory approximation) at the radial node interface. The flux continuity condition is satisfied by using the same boundary value coefficients at the common interface of radially neighboring nodes.

According to PL-transport theory, the even l component of the angular current in x and y directions can be written as:

$$\begin{aligned} J^{x}_{l,\,m,\,g}(\mathbf{r}) &= -\alpha_{l,\,m+1}\,\phi_{l+1,\,m+1,\,g}(\mathbf{r}) + \beta_{l,\,m-1}\,\phi_{l+1,\,m-1,\,g}(\mathbf{r}) \\ &\quad + \beta_{l,\,m+1}\,\phi_{l-1,\,m+1,\,g}(\mathbf{r}) - \alpha_{l,\,m-1}\,\phi_{l-1,\,m-1,\,g}(\mathbf{r}) \\ J^{y}_{l,\,m,\,g}(\mathbf{r}) &= i\,\{-\alpha_{l,\,m+1}\,\phi_{l+1,\,m+1,\,g}(\mathbf{r}) - \beta_{l,\,m-1}\,\phi_{l+1,\,m-1,\,g}(\mathbf{r}) \\ &\quad + \beta_{l,\,m+1}\,\phi_{l-1,\,m+1,\,g}(\mathbf{r}) + \alpha_{l,\,m-1}\,\phi_{l-1,\,m-1,\,g}(\mathbf{r})\,\} \end{aligned} \quad \text{(A.3.1)}$$

where $\alpha_{l,\,m}$ and $\beta_{l,\,m}$ are defined by Eqs.(A.2.12) and (A.2.13).

The right side of Eqs.(A.3.1) include odd ($l \pm 1$) components for even l. By using the even-odd formulation of Spherical harmonics expantion of angular functions, the right side can also

be represented only by even l components. For the x-direction, from the continuity condition of the angular current, we request the continuity of:

$$
\begin{aligned}
J^{x}_{l,m,g}(\mathbf{r}) = T_g(\mathbf{r})\,\{ & \\
& -\alpha_{l,m+1}\alpha_{l+1,m+2}\ (\partial/\partial x)\ \phi_{l+2,m+2,g}(\mathbf{r}) \\
& +\alpha_{l,m+1}\beta_{l+1,m}\ (\partial/\partial x)\ \phi_{l+2,m,g}(\mathbf{r}) \\
& +\beta_{l,m-1}\alpha_{l+1,m}\ (\partial/\partial x)\ \phi_{l+2,m,g}(\mathbf{r}) \\
& -\beta_{l,m-1}\beta_{l+1,m-2}\ (\partial/\partial x)\ \phi_{l+2,m-2,g}(\mathbf{r}) \\
& +\alpha_{l,m+1}\beta_{l+1,m+2}\ (\partial/\partial x)\ \phi_{l,m+2,g}(\mathbf{r}) \\
& +\beta_{l,m+1}\alpha_{l-1,m+2}\ (\partial/\partial x)\ \phi_{l,m+2,g}(\mathbf{r}) \\
& -\alpha_{l,m+1}\alpha_{l+1,m}\ (\partial/\partial x)\ \phi_{l,m,g}(\mathbf{r}) \\
& -\beta_{l,m-1}\beta_{l+1,m}\ (\partial/\partial x)\ \phi_{l,m,g}(\mathbf{r}) \\
& -\beta_{l,m+1}\beta_{l-1,m}\ (\partial/\partial x)\ \phi_{l,m,g}(\mathbf{r}) \\
& -\alpha_{l,m-1}\alpha_{l-1,m}\ (\partial/\partial x)\ \phi_{l,m,g}(\mathbf{r}) \\
& +\beta_{l,m-1}\alpha_{l+1,m-2}\ (\partial/\partial x)\ \phi_{l,m-2,g}(\mathbf{r}) \\
& +\alpha_{l,m-1}\beta_{l-1,m-2}\ (\partial/\partial x)\ \phi_{l,m-2,g}(\mathbf{r}) \\
& -\beta_{l,m+1}\beta_{l-1,m+2}\ (\partial/\partial x)\ \phi_{l-2,m+2,g}(\mathbf{r}) \\
& +\beta_{l,m+1}\alpha_{l-1,m}\ (\partial/\partial x)\ \phi_{l-2,m,g}(\mathbf{r}) \\
& +\alpha_{l,m-1}\beta_{l-1,m}\ (\partial/\partial x)\ \phi_{l-2,m,g}(\mathbf{r}) \\
& -\alpha_{l,m-1}\alpha_{l-1,m-2}\ (\partial/\partial x)\ \phi_{l-2,m-2,g}(\mathbf{r})\ \} \\
= & -\mathrm{aap}_{l,m,g}(\mathbf{r})\ (\partial/\partial x)\ \phi_{l+2,m+2,g}(\mathbf{r}) \\
& +\mathrm{abbap1}_{l,m,g}(\mathbf{r})\ (\partial/\partial x)\ \phi_{l+2,m,g}(\mathbf{r}) \\
& -\mathrm{bbp}_{l,m,g}(\mathbf{r})\ (\partial/\partial x)\ \phi_{l+2,m-2,g}(\mathbf{r}) \\
& +\mathrm{abba01}_{l,m,g}(\mathbf{r})\ (\partial/\partial x)\ \phi_{l,m+2,g}(\mathbf{r}) \\
& -\mathrm{aabb1}_{l,m,g}(\mathbf{r})\ (\partial/\partial x)\ \phi_{l,m,g}(\mathbf{r}) \\
& +\mathrm{abba02}_{l,m,g}(\mathbf{r})\ (\partial/\partial x)\ \phi_{l,m-2,g}(\mathbf{r}) \\
& -\mathrm{bbm}_{l,m,g}(\mathbf{r})\ (\partial/\partial x)\ \phi_{l-2,m+2,g}(\mathbf{r}) \\
& +\mathrm{abbam1}_{l,m,g}(\mathbf{r})\ (\partial/\partial x)\ \phi_{l-2,m,g}(\mathbf{r}) \\
& -\mathrm{aam}_{l,m,g}(\mathbf{r})\ (\partial/\partial x)\ \phi_{l-2,m-2,g}(\mathbf{r}) \qquad \text{(A.3.2)}
\end{aligned}
$$

at node interfaces that are perpendicular to the x-axis. Here,

$$
\begin{aligned}
\mathrm{aap}_{l,m,g}(\mathbf{r}) &= T_g(\mathbf{r})\ \alpha_{l,m+1}\alpha_{l+1,m+2} && \text{(A.3.3)}\\
\mathrm{abbap1}_{l,m,g}(\mathbf{r}) &= T_g(\mathbf{r})\,(\ \alpha_{l,m+1}\beta_{l+1,m}+\beta_{l,m-1}\alpha_{l+1,m}\ ) && \text{(A.3.4)}\\
\mathrm{bbp}_{l,m,g}(\mathbf{r}) &= T_g(\mathbf{r})\ \beta_{l,m-1}\beta_{l+1,m-2} && \text{(A.3.5)}\\
\mathrm{abba01}_{l,m,g}(\mathbf{r}) &= T_g(\mathbf{r})\,(\ \alpha_{l,m+1}\beta_{l+1,m+2}+\beta_{l,m+1}\alpha_{l-1,m+2}\ ) && \text{(A.3.6)}\\
\mathrm{abba02}_{l,m,g}(\mathbf{r}) &= T_g(\mathbf{r})\,(\ \beta_{l,m-1}\alpha_{l+1,m-2}+\alpha_{l,m-1}\beta_{l-1,m-2}\ ) && \text{(A.3.7)}\\
\mathrm{bbm}_{l,m,g}(\mathbf{r}) &= T_g(\mathbf{r})\ \beta_{l,m+1}\beta_{l-1,m+2} && \text{(A.3.8)}\\
\mathrm{abbaml}_{l,m,g}(\mathbf{r}) &= T_g(\mathbf{r})\,(\ \beta_{l,m+1}\alpha_{l-1,m}+\alpha_{l,m-1}\beta_{l-1,m}\ ) && \text{(A.3.9)}\\
\mathrm{aam}_{l,m,g}(\mathbf{r}) &= T_g(\mathbf{r})\ \alpha_{l,m-1}\alpha_{l-1,m-2} && \text{(A.3.10)}
\end{aligned}
$$

and aabb1 is defined by Eq.(A.2.11).

Substitute the expansion (A.1.1) into (A.3.2), and define:

$$
\begin{aligned}
J^{Sx}_{nr,l,m,g}(\mathbf{r}) = & -\mathrm{aap}_{l,m,g}(\mathbf{r})\ (\partial/\partial x)\ \varphi^{S}_{nr,l+2,m+2,g}(\mathbf{r}) \\
& +\mathrm{abbap1}_{l,m,g}(\mathbf{r})\ (\partial/\partial x)\ \varphi^{S}_{nr,l+2,m,g}(\mathbf{r}) \\
& -\mathrm{bbp}_{l,m,g}(\mathbf{r})\ (\partial/\partial x)\ \varphi^{S}_{nr,l+2,m-2,g}(\mathbf{r}) \\
& +\mathrm{abba01}_{l,m,g}(\mathbf{r})\ (\partial/\partial x)\ \varphi^{S}_{nr,l,m+2,g}(\mathbf{r}) \\
& -\mathrm{aabb1}_{l,m,g}(\mathbf{r})\ (\partial/\partial x)\ \varphi^{S}_{nr,l,m,g}(\mathbf{r}) \\
& +\mathrm{abba02}_{l,m,g}(\mathbf{r})\ (\partial/\partial x)\ \varphi^{S}_{nr,l,m-2,g}(\mathbf{r})
\end{aligned}
$$

$$
\begin{aligned}
&- \mathrm{bbm}_{l,\mathrm{m},\mathrm{g}}(\mathbf{r}) \quad (\partial/\partial \mathrm{x})\, \varphi^{\mathrm{S}}_{\mathrm{nr},\, l-2,\, \mathrm{m}+2,\ \mathrm{g}}(\mathbf{r}) \\
&+ \mathrm{abbam1}_{l,\mathrm{m},\mathrm{g}}(\mathbf{r}) \, (\partial/\partial \mathrm{x})\, \varphi^{\mathrm{S}}_{\mathrm{nr},\, l-2,\, \mathrm{m},\ \mathrm{g}}(\mathbf{r}) \\
&- \mathrm{aam}_{l,\mathrm{m},\mathrm{g}}(\mathbf{r}) \quad (\partial/\partial \mathrm{x})\, \varphi^{\mathrm{S}}_{\mathrm{nr},\, l-2,\, \mathrm{m}-2,\ \mathrm{g}}(\mathbf{r}) \qquad \text{(A.3.11)}
\end{aligned}
$$

$$
\begin{aligned}
J^{\mathrm{CBx}}_{\mathrm{pp},\,\mathrm{lmcq},\,l,\,\mathrm{m},\,\mathrm{g}}(\mathbf{r}) = \;
&- \mathrm{aap}_{l,\mathrm{m},\mathrm{g}}(\mathbf{r}) \quad (\partial/\partial \mathrm{x})\, \varphi^{\mathrm{CB}}_{\mathrm{pp},\,\mathrm{lmcq},\, l+2,\, \mathrm{m}+2,\ \mathrm{g}}(\mathbf{r}) \\
&+ \mathrm{abbap1}_{l,\mathrm{m},\mathrm{g}}(\mathbf{r}) \, (\partial/\partial \mathrm{x})\, \varphi^{\mathrm{CB}}_{\mathrm{pp},\,\mathrm{lmcq},\, l+2,\, \mathrm{m},\ \mathrm{g}}(\mathbf{r}) \\
&- \mathrm{bbp}_{l,\mathrm{m},\mathrm{g}}(\mathbf{r}) \quad (\partial/\partial \mathrm{x})\, \varphi^{\mathrm{CB}}_{\mathrm{pp},\,\mathrm{lmcq},\, l+2,\, \mathrm{m}-2,\ \mathrm{g}}(\mathbf{r}) \\
&+ \mathrm{abba01}_{l,\mathrm{m},\mathrm{g}}(\mathbf{r}) \, (\partial/\partial \mathrm{x})\, \varphi^{\mathrm{CB}}_{\mathrm{pp},\,\mathrm{lmcq},\, l,\, \mathrm{m}+2,\ \mathrm{g}}(\mathbf{r}) \\
&- \mathrm{aabb1}_{l,\mathrm{m},\mathrm{g}}(\mathbf{r}) \, (\partial/\partial \mathrm{x})\, \varphi^{\mathrm{CB}}_{\mathrm{pp},\,\mathrm{lmcq},\, l,\, \mathrm{m},\ \mathrm{g}}(\mathbf{r}) \\
&+ \mathrm{abba02}_{l,\mathrm{m},\mathrm{g}}(\mathbf{r}) \, (\partial/\partial \mathrm{x})\, \varphi^{\mathrm{CB}}_{\mathrm{pp},\,\mathrm{lmcq},\, l,\, \mathrm{m}-2,\ \mathrm{g}}(\mathbf{r}) \\
&- \mathrm{bbm}_{l,\mathrm{m},\mathrm{g}}(\mathbf{r}) \quad (\partial/\partial \mathrm{x})\, \varphi^{\mathrm{CB}}_{\mathrm{pp},\,\mathrm{lmcq},\, l-2,\, \mathrm{m}+2,\ \mathrm{g}}(\mathbf{r}) \\
&+ \mathrm{abbam1}_{l,\mathrm{m},\mathrm{g}}(\mathbf{r}) \, (\partial/\partial \mathrm{x})\, \varphi^{\mathrm{CB}}_{\mathrm{pp},\,\mathrm{lmcq},\, l-2,\, \mathrm{m},\ \mathrm{g}}(\mathbf{r}) \\
&- \mathrm{aam}_{l,\mathrm{m},\mathrm{g}}(\mathbf{r}) \quad (\partial/\partial \mathrm{x})\, \varphi^{\mathrm{CB}}_{\mathrm{pp},\,\mathrm{lmcq},\, l-2,\, \mathrm{m}-2,\ \mathrm{g}}(\mathbf{r}) \qquad \text{(A.3.12)}
\end{aligned}
$$

$$
\begin{aligned}
J^{\mathrm{SBx}}_{\mathrm{pp},\,\mathrm{lmsq},\,l,\,\mathrm{m},\,\mathrm{g}}(\mathbf{r}) = \;
&- \mathrm{aap}_{l,\mathrm{m},\mathrm{g}}(\mathbf{r}) \quad (\partial/\partial \mathrm{x})\, \varphi^{\mathrm{SB}}_{\mathrm{pp},\,\mathrm{lmsq},\, l+2,\, \mathrm{m}+2,\ \mathrm{g}}(\mathbf{r}) \\
&+ \mathrm{abbap1}_{l,\mathrm{m},\mathrm{g}}(\mathbf{r}) \, (\partial/\partial \mathrm{x})\, \varphi^{\mathrm{SB}}_{\mathrm{pp},\,\mathrm{lmsq},\, l+2,\, \mathrm{m},\ \mathrm{g}}(\mathbf{r}) \\
&- \mathrm{bbp}_{l,\mathrm{m},\mathrm{g}}(\mathbf{r}) \quad (\partial/\partial \mathrm{x})\, \varphi^{\mathrm{SB}}_{\mathrm{pp},\,\mathrm{lmsq},\, l+2,\, \mathrm{m}-2,\ \mathrm{g}}(\mathbf{r}) \\
&+ \mathrm{abba01}_{l,\mathrm{m},\mathrm{g}}(\mathbf{r}) \, (\partial/\partial \mathrm{x})\, \varphi^{\mathrm{SB}}_{\mathrm{pp},\,\mathrm{lmsq},\, l,\, \mathrm{m}+2,\ \mathrm{g}}(\mathbf{r}) \\
&- \mathrm{aabb1}_{l,\mathrm{m},\mathrm{g}}(\mathbf{r}) \, (\partial/\partial \mathrm{x})\, \varphi^{\mathrm{SB}}_{\mathrm{pp},\,\mathrm{lmsq},\, l,\, \mathrm{m},\ \mathrm{g}}(\mathbf{r}) \\
&+ \mathrm{abba02}_{l,\mathrm{m},\mathrm{g}}(\mathbf{r}) \, (\partial/\partial \mathrm{x})\, \varphi^{\mathrm{SB}}_{\mathrm{pp},\,\mathrm{lmsq},\, l,\, \mathrm{m}-2,\ \mathrm{g}}(\mathbf{r}) \\
&- \mathrm{bbm}_{l,\mathrm{m},\mathrm{g}}(\mathbf{r}) \quad (\partial/\partial \mathrm{x})\, \varphi^{\mathrm{SB}}_{\mathrm{pp},\,\mathrm{lmsq},\, l-2,\, \mathrm{m}+2,\ \mathrm{g}}(\mathbf{r}) \\
&+ \mathrm{abbam1}_{l,\mathrm{m},\mathrm{g}}(\mathbf{r}) \, (\partial/\partial \mathrm{x})\, \varphi^{\mathrm{SB}}_{\mathrm{pp},\,\mathrm{lmsq},\, l-2,\, \mathrm{m},\ \mathrm{g}}(\mathbf{r}) \\
&- \mathrm{aam}_{l,\mathrm{m},\mathrm{g}}(\mathbf{r}) \quad (\partial/\partial \mathrm{x})\, \varphi^{\mathrm{SB}}_{\mathrm{pp},\,\mathrm{lmsq},\, l-2,\, \mathrm{m}-2,\ \mathrm{g}}(\mathbf{r}) \qquad \text{(A.3.13)}
\end{aligned}
$$

where $\mathbf{r} = (\mathrm{x}, \mathrm{y})$ in Eqs.(A.3.11 through 13). One obtains:

$$
\begin{aligned}
J^{\mathrm{x}}_{l,\mathrm{m},\mathrm{g}}(\mathrm{x},\mathrm{y},\mathrm{z}) = \;
&\sum_{\mathrm{nr},\,\mathrm{nz}} F^{\mathrm{S}}_{\mathrm{nr},\,\mathrm{nz},\,\mathrm{g}}\, J^{\mathrm{Sx}}_{\mathrm{nr},\,l,\,\mathrm{m},\,\mathrm{g}}(\mathrm{x},\mathrm{y})\, \mathrm{Rz}_{\mathrm{nz}}(\mathrm{z}) \\
&+ \sum_{\mathrm{pp}} \sum_{\mathrm{lmcq},\,\mathrm{nz}} F^{\mathrm{CB}}_{\mathrm{pp},\,\mathrm{lmcq},\,\mathrm{nz},\,\mathrm{g}}\, J^{\mathrm{CBx}}_{\mathrm{pp},\,\mathrm{lmcq},\,l,\,\mathrm{m},\,\mathrm{g}}(\mathrm{x},\mathrm{y})\, \mathrm{Rz}_{\mathrm{nz}}(\mathrm{z}) \\
&+ \sum_{\mathrm{pp}} \sum_{\mathrm{lmsq},\,\mathrm{nz}} F^{\mathrm{SB}}_{\mathrm{pp},\,\mathrm{lmsq},\,\mathrm{nz},\,\mathrm{g}}\, J^{\mathrm{SBx}}_{\mathrm{pp},\,\mathrm{lmsq},\,l,\,\mathrm{m},\,\mathrm{g}}(\mathrm{x},\mathrm{y})\, \mathrm{Rz}_{\mathrm{nz}}(\mathrm{z}) \\
&\qquad\qquad\qquad\qquad\qquad\qquad\qquad\qquad\qquad\qquad\qquad\qquad \text{(A.3.14)}
\end{aligned}
$$

To determine the boundary value coefficients, we request the continuity of the spatial moments of $J^{\mathrm{x}}_{l,\mathrm{m},\mathrm{g}}(\mathrm{x},\mathrm{y},\mathrm{z})$ over a surface (perpendicular to the x-axis) of a node, which is defined by:

$$
J^{\mathrm{x}}_{l,\,\mathrm{m},\,\mathrm{sr}',\,\mathrm{nz}',\,\mathrm{g}}(\mathrm{x_s}) = \int_{\mathrm{pp}} \mathrm{dy}\, \mathrm{dz}\, P_{\mathrm{sr}'}(\mathrm{y})\, \mathrm{Rz}_{\mathrm{nz}'}(\mathrm{z})\, J^{\mathrm{x}}_{l,\,\mathrm{m},\,\mathrm{g}}(\mathrm{x_s},\mathrm{y},\mathrm{z}) \qquad \text{(A.3.15)}
$$

for all the combination of indices lmcq' (= l, m, sr') and nz' = 1, 2, ..., N – 1, where $\int_{\mathrm{pp}} \mathrm{dy}\, \mathrm{dz}$ is the integration over the node surface which is perpendicular to the x-axis, $P_{\mathrm{sr}'}(\mathrm{y})$ is 1D Legendre function along y-axis, and $\mathrm{x_s}$ is the x-coordinate of the node surface.

From the real part of Eq.(A.3.15), we obtain a set of linear equations for $F^{\mathrm{CB}}_{\mathrm{pp},\,\mathrm{lmcq},\,\mathrm{nz},\,\mathrm{g}}$ along x-direction:

$$
\begin{aligned}
&- \sum_{\mathrm{nr},\,\mathrm{nz}'} F^{\mathrm{S}}_{\mathrm{nr},\,\mathrm{nz}',\,\mathrm{g}}\, \mathrm{JCN}_{\mathrm{pp},\,\mathrm{lmcq},\,\mathrm{nr},\,\mathrm{g}}\, \mathrm{RzRz}_{\mathrm{nz},\,\mathrm{nz}'} \\
&- \sum_{\mathrm{pp}'} \sum_{\mathrm{lmcq}',\,\mathrm{nz}'} F^{\mathrm{CB}}_{\mathrm{pp}',\,\mathrm{lmcq}',\,\mathrm{nz}',\,\mathrm{g}}\, \mathrm{JCC}_{\mathrm{pp},\,\mathrm{lmcq},\,\mathrm{pp}',\,\mathrm{lmcq}',\,\mathrm{g}}\, \mathrm{RzRz}_{\mathrm{nz},\,\mathrm{nz}'} \\
&- \sum_{\mathrm{pp}'} \sum_{\mathrm{lmsq},\,\mathrm{nz}'} F^{\mathrm{SB}}_{\mathrm{pp}',\,\mathrm{lmsq},\,\mathrm{nz}',\,\mathrm{g}}\, \mathrm{JCS}_{\mathrm{pp},\,\mathrm{lmcq},\,\mathrm{pp}',\,\mathrm{lmsq},\,\mathrm{g}}\, \mathrm{RzRz}_{\mathrm{nz},\,\mathrm{nz}'} \quad \text{for the left node} \\
&= \sum_{\mathrm{nr},\,\mathrm{nz}'} F^{\mathrm{S}}_{\mathrm{nr},\,\mathrm{nz}',\,\mathrm{g}}\, \mathrm{JCN}_{\mathrm{pp},\,\mathrm{lmcq},\,\mathrm{nr},\,\mathrm{g}}\, \mathrm{RzRz}_{\mathrm{nz},\,\mathrm{nz}'}
\end{aligned}
$$

$$+\sum_{pp'}\sum_{lmcq',\,nz'} F^{CB}_{pp',\,lmcq',\,nz',\,g}\,JCC_{pp,\,lmcq,\,pp',\,lmcq',\,g}\,RzRz_{nz,\,nz'}$$
$$+\sum_{pp'}\sum_{lmsq,\,nz'} F^{SB}_{pp',\,lmsq,\,nz',\,g}\,JCS_{pp,\,lmcq,\,pp',\,lmsq,\,g}\,RzRz_{nz,\,nz'} \quad \text{for the right node} \tag{A.3.16}$$

where

$$JCN_{pp,\,lmcq,\,nr,\,g} = \int_{pp} dy\, P_{sr}(y)\, Re[J^{Sx}_{nr,\,l,\,m,\,g}(x_s, y)] \tag{A.3.17}$$
$$JCC_{pp,\,lmcq,\,pp',\,lmcq',\,g} = \int_{pp} dy\, P_{sr}(y)\, Re[J^{CBx}_{pp',\,lmcq',\,l,\,m,\,g}(x_s, y)] \tag{A.3.18}$$
$$JCS_{pp,\,lmcq,\,pp',\,lmsq,\,g} = \int_{pp} dy\, P_{sr}(y)\, Re[J^{SBx}_{pp',\,lmsq,\,l,\,m,\,g}(x_s, y)] \tag{A.3.19}$$

where Re[] means the real part.

Similarly, from the imaginary part of Eq.(A.3.15), we obtain:

$$-\sum_{nr,\,nz'} F^{S}_{nr,\,nz',\,g}\,JSN_{pp,\,lmsq,\,nr,\,g}\,RzRz_{nz,\,nz'}$$
$$-\sum_{pp'}\sum_{lmcq,\,nz'} F^{CB}_{pp',\,lmcq,\,nz',\,g}\,JSC_{pp,\,lmsq,\,pp',\,lmcq,\,g}\,RzRz_{nz,\,nz'}$$
$$-\sum_{pp'}\sum_{lmsq',\,nz'} F^{SB}_{pp',\,lmsq',\,nz',\,g}\,JSS_{pp,\,lmsq,\,pp',\,lmsq',\,g}\,RzRz_{nz,\,nz'} \quad \text{for the left node}$$
$$=\sum_{nr,\,nz'} F^{S}_{nr,\,nz',\,g}\,JSN_{pp,\,lmsq,\,nr,\,g}\,RzRz_{nz,\,nz'}$$
$$+\sum_{pp'}\sum_{lmcq,\,nz'} F^{CB}_{pp',\,lmcq,\,nz',\,g}\,JSC_{pp,\,lmsq,\,pp',\,lmcq,\,g}\,RzRz_{nz,\,nz'}$$
$$+\sum_{pp'}\sum_{lmsq',\,nz'} F^{SB}_{pp',\,lmsq',\,nz',\,g}\,JSS_{pp,\,lmsq,\,pp',\,lmsq',\,g}\,RzRz_{nz,\,nz'} \quad \text{for the right node} \tag{A.3.20}$$

where

$$JSN_{pp,\,lmsq,\,nr,\,g} = \int_{pp} dy\, P_{sr}(y)\, Im[J^{Sx}_{nr,\,l,\,m,\,g}(x_s, y)] \tag{A.3.21}$$
$$JSC_{pp,\,lmsq,\,pp',\,lmcq,\,g} = \int_{pp} dy\, P_{sr}(y)\, Im[J^{CBx}_{pp',\,lmcq,\,l,\,m,\,g}(x_s, y)] \tag{A.3.22}$$
$$JSS_{pp,\,lmsq,\,pp',\,lmsq',\,g} = \int_{pp} dy\, P_{sr}(y)\, Im[J^{SBx}_{pp',\,lmsq',\,l,\,m,\,g}(x_s, y)] \tag{A.3.23}$$

Similar equations are obtained along the y-direction in the same way.

A.4 Continuity Condition at Axial Node Interface

At the axial node interfaces (which are perpendicular to the z-axis) the expansion coefficients $F^{S}_{nr,\,nz,\,g}$, $F^{CB}_{pp,\,lmcq,\,nz,\,g}$ and $F^{SB}_{pp,\,lmsq,\,nz,\,g}$ for nz = 0 (of the upper node of the axial interface) and nz = N (of the lower node of the axial interface) are determined by requesting the continuity of the flux moments and the angular current densities across the axial interfaces.

As we expand the flux moment by Eq.(A.1.1), it is obvious that if we request the continuity of each term in the expansion:

$$F^{S}_{nr,\,nz=N,\,g}\,Re[\varphi^{S}_{nr,\,l,\,m,\,g}(x, y)]\,|_{\text{lower node}} = F^{S}_{nr,\,nz=0,\,g}\,Re[\varphi^{S}_{nr,\,l,\,m,\,g}(x, y)]\,|_{\text{upper node}} \tag{A.4.1}$$
$$F^{S}_{nr,\,nz=N,\,g}\,Im[\varphi^{S}_{nr,\,l,\,m,\,g}(x, y)]\,|_{\text{lower node}} = F^{S}_{nr,\,nz=0,\,g}\,Im[\varphi^{S}_{nr,\,l,\,m,\,g}(x, y)]\,|_{\text{upper node}} \tag{A.4.2}$$
$$F^{CB}_{pp,\,lmcq,\,nz=N,\,g}\,Re[\varphi^{CB}_{pp,\,lmcq,\,l,\,m,\,g}(x, y)]\,|_{\text{lower node}} = F^{CB}_{pp,\,lmcq,\,nz=0,\,g}\,Re[\varphi^{CB}_{pp,\,lmcq,\,l,\,m,\,g}(x, y)]\,|_{\text{upper node}} \tag{A.4.3}$$

$$F^{CB}_{pp,\,lmcq,\,nz=N,\,g}\ \mathrm{Im}[\varphi^{CB}_{pp,\,lmcq,\,l,\,m,\,g}(x,y)]\,|_{\text{lower node}} = F^{CB}_{pp,\,lmcq,\,nz=0,\,g}\ \mathrm{Im}[\varphi^{CB}_{pp,\,lmcq,\,l,\,m,\,g}(x,y)]\,|_{\text{upper node}} \quad \text{(A.4.4)}$$

$$F^{SB}_{pp,\,lmsq,\,nz=N,\,g}\ \mathrm{Re}[\varphi^{SB}_{pp,\,lmsq,\,l,\,m,\,g}(x,y)\,|_{\text{lower node}} = F^{SB}_{pp,\,lmsq,\,nz=0,\,g}\ \mathrm{Re}[\varphi^{SB}_{pp,\,lmsq,\,l,\,m,\,g}(x,y)\,|_{\text{upper node}} \quad \text{(A.4.5)}$$

$$F^{SB}_{pp,\,lmsq,\,nz=N,\,g}\ \mathrm{Im}[\varphi^{SB}_{pp,\,lmsq,\,l,\,m,\,g}(x,y)\,|_{\text{lower node}} = F^{SB}_{pp,\,lmsq,\,nz=0,\,g}\ \mathrm{Im}[\varphi^{SB}_{pp,\,lmsq,\,l,\,m,\,g}(x,y)\,|_{\text{upper node}} \quad \text{(A.4.6)}$$

then, by using the fact that $Rz_{nz}(z) = 1$ at the top and the bottom of a node, the expanded flux moments become continuous across the axial interfaces between nodes.

Because the number of expansion coefficients is not enough to hold the precise continuity as requested by Eqs.(A.4.1 through 6), we have to relax the requested continuity by [as we did in deriving Eq.(A.3.15)] making weighted average of the continuity as:

$$\begin{aligned} &F^{S}_{nr,\,nz=N,\,g}\ \int_{node} dr \sum_{l,\,m} \{\, WC^{S}_{nr,\,l,\,m,\,g}(x,y)\ \mathrm{Re}[\varphi^{S}_{nr,\,l,\,m,\,g}(x,y)] \\ &\qquad + WS^{S}_{nr,\,l,\,m,\,g}(x,y)\ \mathrm{Im}[\varphi^{S}_{nr,\,l,\,m,\,g}(x,y)]\,\}\,|_{\text{lower node}} \\ =\ &F^{S}_{nr,\,nz=0,\,g}\ \int_{node} dr \sum_{l,\,m} \{\, WC^{S}_{nr,\,l,\,m,\,g}(x,y)\ \mathrm{Re}[\varphi^{S}_{nr,\,l,\,m,\,g}(x,y)] \\ &\qquad + WS^{S}_{nr,\,l,\,m,\,g}(x,y)\ \mathrm{Im}[\varphi^{S}_{nr,\,l,\,m,\,g}(x,y)]\,\}\,|_{\text{upper node}} \end{aligned} \quad \text{(A.4.7)}$$

$$\begin{aligned} &F^{CB}_{pp,\,lmcq,\,nz=N,\,g} \\ &\quad .\int_{node} dr \sum_{l,\,m} \{\, WC^{CB}_{pp,\,lmcq,\,l,\,m,\,g}(x,y)\ \mathrm{Re}[\varphi^{CB}_{pp,\,lmcq,\,l,\,m,\,g}(x,y)] \\ &\qquad + WS^{CB}_{pp,\,lmcq,\,l,\,m,\,g}(x,y)\ \mathrm{Im}[\varphi^{CB}_{pp,\,lmcq,\,l,\,m,\,g}(x,y)]\,\}\,|_{\text{lower node}} \\ =\ &F^{CB}_{pp,\,lmcq,\,nz=0,\,g} \\ &\quad .\int_{node} dr \sum_{l,\,m} \{\, WC^{CB}_{pp,\,lmcq,\,l,\,m,\,g}(x,y)\ \mathrm{Re}[\varphi^{CB}_{pp,\,lmcq,\,l,\,m,\,g}(x,y)] \\ &\qquad + WS^{CB}_{pp,\,lmcq,\,l,\,m,\,g}(x,y)\ \mathrm{Im}[\varphi^{CB}_{pp,\,lmcq,\,l,\,m,\,g}(x,y)]\,\}\,|_{\text{upper node}} \end{aligned} \quad \text{(A.4.8)}$$

$$\begin{aligned} &F^{SB}_{pp,\,lmsq,\,nz=N,\,g} \\ &\quad .\int_{node} dr \sum_{l,\,m} \{\, WC^{SB}_{pp,\,lmsq,\,l,\,m,\,g}(x,y)\ \mathrm{Re}[\varphi^{SB}_{pp,\,lmsq,\,l,\,m,\,g}(x,y)] \\ &\qquad + WS^{SB}_{pp,\,lmsq,\,l,\,m,\,g}(x,y)\ \mathrm{Im}[\varphi^{SB}_{pp,\,lmsq,\,l,\,m,\,g}(x,y)]\,\}\,|_{\text{lower node}} \\ =\ &F^{SB}_{pp,\,lmsq,\,nz=0,\,g} \\ &\quad .\int_{node} dr \sum_{l,\,m} \{\, WC^{SB}_{pp,\,lmsq,\,l,\,m,\,g}(x,y)\ \mathrm{Re}[\varphi^{SB}_{pp,\,lmsq,\,l,\,m,\,g}(x,y)] \\ &\qquad + WS^{SB}_{pp,\,lmsq,\,l,\,m,\,g}(x,y)\ \mathrm{Im}[\varphi^{SB}_{pp,\,lmsq,\,l,\,m,\,g}(x,y)]\,\}\,|_{\text{upper node}} \end{aligned} \quad \text{(A.4.9)}$$

where $\int_{node} dr$ is the integration with respect to the radial coordinate x, y over the axial node surface. The weights WC^{S}, WS^{S}, WC^{CB}, WS^{CB}, WC^{SB}, WS^{SB} will be discussed later.

Similar continuity conditions are derived for the angular current. From PL-transport theory, the axial angular current is defined by:

$$J^{z}_{l,\,m,\,g}(\mathbf{r}) = \eta_{l,\,m}\,\phi_{l+1,\,m,\,g}(\mathbf{r}) + \gamma_{l,\,m}\,\phi_{l-1,\,m,\,g}(\mathbf{r}) \quad \text{(A.4.10)}$$

where

$$\eta_{l,\,m} = [\,(l + m + 1)\,(l - m + 1)\,]^{1/2} / (2\,l + 1) \quad \text{(A.4.11)}$$

$$\gamma_{l,\,m} = [\,(l + m)\,(l - m)\,]^{1/2} / (2\,l + 1) \quad \text{(A.4.12)}$$

As in the case of the radial direction, by using the even-odd formulation of Spherical harmonics expantion of angular functions, the right side of Eq.(A.4.10) can also be represented only by even l components, as

$$J^{z}_{l,m,g}(\mathbf{r}) = -\,eep_{l,m,g}(\mathbf{r})\;(\partial/\partial z)\,\phi_{l+2,m,g}(\mathbf{r}) - egge_{l,m,g}(\mathbf{r})\;(\partial/\partial z)\,\phi_{l,m,g}(\mathbf{r}) - ggm_{l,m,g}(\mathbf{r})\;(\partial/\partial z)\,\phi_{l-2,m,g}(\mathbf{r}) \quad \text{(A.4.13)}$$

where

$$egge_{l,m,g}(\mathbf{r}) = (\eta_{l,m}\,\gamma_{l+1,m} + \gamma_{l,m}\,\eta_{l-1,m,g})\,T_g(\mathbf{r}) \quad \text{(A.4.14)}$$

$$eep_{l,m,g}(\mathbf{r}) = \eta_{l,m}\,\eta_{l+1,m}\,T_g(\mathbf{r}) \quad \text{(A.4.15)}$$

$$ggm_{l,m,g}(\mathbf{r}) = \gamma_{l,m}\,\gamma_{l-1,m}\,T_g(\mathbf{r}) \quad \text{(A.4.16)}$$

From the assumption that a node is homogeneous along the axial direction, the spatial position **r** can be replaced by (x, y) in Eqs.(A.4.14 through 16). By substituting (A.1.1) into the right side of (A.4.13), and defining:

$$J^{Sz}_{nr,l,m,g}(x,y) = -\,eep_{l,m,g}(x,y)\;\varphi^{S}_{nr,l+2,m,g}(x,y) - egge_{l,m,g}(x,y)\;\varphi^{S}_{nr,l,m,g}(x,y) - ggm_{l,m,g}(x,y)\;\varphi^{S}_{nr,l-2,m,g}(x,y) \quad \text{(A.4.17)}$$

$$J^{CBz}_{pp,lmcq,l,m,g}(x,y) = -\,eep_{l,m,g}(x,y)\;\varphi^{CB}_{pp,lmcq,l+2,m,g}(x,y) - egge_{l,m,g}(x,y)\;\varphi^{CB}_{pp,lmcq,l,m,g}(x,y) - ggm_{l,m,g}(x,y)\;\varphi^{CB}_{pp,lmcq,l-2,m,g}(x,y) \quad \text{(A.4.18)}$$

$$J^{SBz}_{pp,lmsq,l,m,g}(x,y) = -\,eep_{l,m,g}(x,y)\;\varphi^{SB}_{pp,lmsq,l+2,m,g}(x,y) - egge_{l,m,g}(x,y)\;\varphi^{SB}_{pp,lmsq,l,m,g}(x,y) - ggm_{l,m,g}(x,y)\;\varphi^{SB}_{pp,lmsq,l-2,m,g}(x,y) \quad \text{(A.4.19)}$$

we obtain

$$J^{z}_{l,m,g}(\mathbf{r}) = \sum_{nr,nz} F^{S}_{nr,nz,g}\,J^{Sz}_{nr,l,m,g}(x,y)\,(\partial/\partial z)\,Rz_{nz}(z) + \sum_{pp}\sum_{lmcq,nz} F^{CB}_{pp,lmcq,nz,g}\,J^{CBz}_{pp,lmcq,l,m,g}(x,y)\,(\partial/\partial z)\,Rz_{nz}(z) + \sum_{pp}\sum_{lmsq,nz} F^{SB}_{pp,lmsq,nz,g}\,J^{SBz}_{pp,lmsq,l,m,g}(x,y)\,(\partial/\partial z)\,Rz_{nz}(z) \quad \text{(A.4.20)}$$

The current defined by Eq.(A.4.20) must be continuous across the axial interface between nodes. This can be achieved by requesting continuity of each of the terms as follows [similar to Eqs.(A.4.1 through 6) for the case of the flux moment continuity]

$$F^{S}_{nr,nz=N,g}\,\mathrm{Re}[J^{Sz}_{nr,l,m,g}(x,y)]\,(\partial/\partial z)\,Rz_{nz}(z)\,|_{\text{lower node}} = F^{S}_{nr,nz=0,g}\,\mathrm{Re}[J^{Sz}_{nr,l,m,g}(x,y)]\,(\partial/\partial z)\,Rz_{nz}(z)\,|_{\text{upper node}} \quad \text{(A.4.21)}$$

$$F^{S}_{nr,nz=N,g}\,\mathrm{Im}[J^{Sz}_{nr,l,m,g}(x,y)]\,(\partial/\partial z)\,Rz_{nz}(z)\,|_{\text{lower node}} = F^{S}_{nr,nz=0,g}\,\mathrm{Im}[J^{Sz}_{nr,l,m,g}(x,y)]\,(\partial/\partial z)\,Rz_{nz}(z)\,|_{\text{upper node}} \quad \text{(A.4.22)}$$

$$F^{CB}_{pp,lmcq,nz=N,g}\,\mathrm{Re}[J^{CBz}_{pp,lmcq,l,m,g}(x,y)]\,(\partial/\partial z)\,Rz_{nz}(z)\,|_{\text{lower node}} = F^{CB}_{pp,lmcq,nz=0,g}\,\mathrm{Re}[J^{CBz}_{pp,lmcq,l,m,g}(x,y)]\,(\partial/\partial z)\,Rz_{nz}(z)\,|_{\text{upper node}} \quad \text{(A.4.23)}$$

$$F^{CB}_{pp,lmcq,nz=N,g}\,\mathrm{Im}[J^{CBz}_{pp,lmcq,l,m,g}(x,y)]\,(\partial/\partial z)\,Rz_{nz}(z)\,|_{\text{lower node}} = F^{CB}_{pp,lmcq,nz=0,g}\,\mathrm{Im}[J^{CBz}_{pp,lmcq,l,m,g}(x,y)]\,(\partial/\partial z)\,Rz_{nz}(z)\,|_{\text{upper node}} \quad \text{(A.4.24)}$$

$$F^{SB}_{pp,lmsq,nz=N,g}\,\mathrm{Re}[J^{SBz}_{pp,lmsq,l,m,g}(x,y)\,(\partial/\partial z)\,Rz_{nz}(z)\,|_{\text{lower node}} = F^{SB}_{pp,lmsq,nz=0,g}\,\mathrm{Re}[J^{SBz}_{pp,lmsq,l,m,g}(x,y)\,(\partial/\partial z)\,Rz_{nz}(z)\,|_{\text{upper node}} \quad \text{(A.4.25)}$$

$$F^{SB}_{pp,lmsq,nz=N,g}\,\mathrm{Im}[J^{SBz}_{pp,lmsq,l,m,g}(x,y)\,(\partial/\partial z)\,Rz_{nz}(z)\,|_{\text{lower node}} = F^{SB}_{pp,lmsq,nz=0,g}\,\mathrm{Im}[J^{SBz}_{pp,lmsq,l,m,g}(x,y)\,(\partial/\partial z)\,Rz_{nz}(z)\,|_{\text{upper node}} \quad \text{(A.4.26)}$$

Also similar to the case of the flux moment continuity, the number of expansion coefficients is not enough to hold the precise continuity as requested by Eqs.(A.4.21 through 26), we have to relax the requested continuity by making weighted average of the continuity as:

$$
\begin{aligned}
& F^{S}_{nr,\, nz = N,\, g} \\
& \quad . \int_{node} dr \sum_{l,\, m} \{ WC^{\,S}_{nr,\, l,\, m,\, g}(x, y)\ \ Re[J^{Sz}_{nr,\, l,\, m,\, g}(x, y)] \\
& \qquad\qquad + WS^{\,S}_{nr,\, l,\, m,\, g}(x, y)\ \ Im[J^{Sz}_{nr,\, l,\, m,\, g}(x, y)] \}\ (\partial/\partial z)\, Rz_{nz}(z) \,|_{\text{lower node}} \\
= \ & F^{S}_{nr,\, nz = 0,\, g} \\
& \quad . \int_{node} dr \sum_{l,\, m} \{ WC^{\,S}_{nr,\, l,\, m,\, g}(x, y)\ \ Re[J^{Sz}_{nr,\, l,\, m,\, g}(x, y)] \\
& \qquad\qquad + WS^{\,S}_{nr,\, l,\, m,\, g}(x, y)\ \ Im[J^{Sz}_{nr,\, l,\, m,\, g}(x, y)] \}\ (\partial/\partial z)\, Rz_{nz}(z) \,|_{\text{upper node}}
\end{aligned}
\qquad \text{(A.4.27)}
$$

$$
\begin{aligned}
& F^{CB}_{pp,\, lmcq,\, nz = N,\, g} \\
& \quad . \int_{node} dr \sum_{l,\, m} \{ WC^{\,CB}_{pp,\, lmcq,\, l,\, m,\, g}(x, y)\ \ Re[J^{CBz}_{pp,\, lmcq,\, l,\, m,\, g}(x, y)] \\
& \qquad\qquad + WS^{\,CB}_{pp,\, lmcq,\, l,\, m,\, g}(x, y)\ \ Im[J^{CBz}_{pp,\, lmcq,\, l,\, m,\, g}(x, y)] \} \\
& \qquad\qquad . (\partial/\partial z)\, Rz_{nz}(z) \,|_{\text{lower node}} \\
= \ & F^{CB}_{pp,\, lmcq,\, nz = 0,\, g} \\
& \quad . \int_{node} dr \sum_{l,\, m} \{ WC^{\,CB}_{pp,\, lmcq,\, l,\, m,\, g}(x, y)\ \ Re[J^{CBz}_{pp,\, lmcq,\, l,\, m,\, g}(x, y)] \\
& \qquad\qquad + WS^{\,CB}_{pp,\, lmcq,\, l,\, m,\, g}(x, y)\ \ Im[J^{CBz}_{pp,\, lmcq,\, l,\, m,\, g}(x, y)] \} \\
& \qquad\qquad . (\partial/\partial z)\, Rz_{nz}(z) \,|_{\text{upper node}}
\end{aligned}
\qquad \text{(A.4.28)}
$$

$$
\begin{aligned}
& F^{SB}_{pp,\, lmsq,\, nz = N,\, g} \\
& \quad . \int_{node} dr \sum_{l,\, m} \{ WC^{\,SB}_{pp,\, lmsq,\, l,\, m,\, g}(x, y)\ \ Re[J^{SBz}_{pp,\, lmsq,\, l,\, m,\, g}(x, y)] \\
& \qquad\qquad + WS^{\,SB}_{pp,\, lmsq,\, l,\, m,\, g}(x, y)\ \ Im[J^{SBz}_{pp,\, lmsq,\, l,\, m,\, g}(x, y)] \} \\
& \qquad\qquad . (\partial/\partial z)\, Rz_{nz}(z) \,|_{\text{lower node}} \\
= \ & F^{SB}_{pp,\, lmsq,\, nz = 0,\, g} \\
& \quad . \int_{node} dr \sum_{l,\, m} \{ WC^{\,SB}_{pp,\, lmsq,\, l,\, m,\, g}(x, y)\ \ Re[J^{SBz}_{pp,\, lmsq,\, l,\, m,\, g}(x, y)] \\
& \qquad\qquad + WS^{\,SB}_{pp,\, lmsq,\, l,\, m,\, g}(x, y)\ \ Im[J^{SBz}_{pp,\, lmsq,\, l,\, m,\, g}(x, y)] \} \\
& \qquad\qquad . (\partial/\partial z)\, Rz_{nz}(z) \,|_{\text{upper node}}
\end{aligned}
\qquad \text{(A.4.29)}
$$

where $\int_{node} dr$ is the integration with respect to the radial coordinate x, y over the axial node surface.

The weights in Eqs.(A.4.7 through 9) and Eqs.(A.4.27 through 29) are defined by:

$$WC^{\,S}_{nr,\, l,\, m,\, g}(x, y) = P_{nr}(x, y)\, Re[\phi^{\infty}_{l,\, m,\, g}(x, y)] \qquad \text{(A.4.30)}$$

$$WS^{\,S}_{nr,\, l,\, m,\, g}(x, y) = P_{nr}(x, y)\, Im[\phi^{\infty}_{l,\, m,\, g}(x, y)] \qquad \text{(A.4.31)}$$

where $\phi^{\infty}_{l,\, m,\, g}(x, y)$ is the infinite-lattice flux moment.

$$
\begin{aligned}
WC^{\,CB}_{pp,\, lmcq,\, l,\, m,\, g}(x, y) &= P_{sr}(y) \quad \text{for pp = XL, XR} \\
&= P_{sr}(x) \quad \text{for pp = YL, YR} \qquad \text{(A.4.32)} \\
WS^{\,CB}_{pp,\, lmcq,\, l,\, m,\, g}(x, y) &= P_{sr}(y) \quad \text{for pp = XL, XR} \\
&= P_{sr}(x) \quad \text{for pp = YL, YR} \qquad \text{(A.4.33)} \\
WC^{\,SB}_{pp,\, lmsq,\, l,\, m,\, g}(x, y) &= P_{sr}(y) \quad \text{for pp = XL, XR} \\
&= P_{sr}(x) \quad \text{for pp = YL, YR} \qquad \text{(A.4.34)} \\
WS^{\,SB}_{pp,\, lmsq,\, l,\, m,\, g}(x, y) &= P_{sr}(y) \quad \text{for pp = XL, XR} \\
&= P_{sr}(x) \quad \text{for pp = YL, YR} \qquad \text{(A.4.35)}
\end{aligned}
$$

A.5 Calculation of Source Expansion Function

The source expansion function is calculated in the same way as the 2D case by solving:

$$\begin{aligned}
&\sum_{m' = m-2,\, m+2:\ \text{even}} D_{l,\, m;\, l+2,\, m',\, g}(x, y)\ \varphi^{S}_{nr,\, l+2,\, m',\, g}(x, y) \\
&+ \sum_{m' = m-2,\, m+2:\ \text{even}} D_{l,\, m;\, l,\, m',\, g}(x, y)\ \varphi^{S}_{nr,\, l,\, m',\, g}(x, y) \\
&+ \sum_{m' = m-2,\, m+2:\ \text{even}} D_{l,\, m;\, l-2,\, m',\, g}(x, y)\ \varphi^{S}_{nr,\, l-2,\, m',\, g}(x, y) + \Sigma^{r}_{l,\, m,\, g}(x, y)\ \varphi^{S}_{nr,\, l,\, m,\, g}(x, y) \\
&= S^{\infty}_{l,\, m,\, g}(x, y)\ P_{nr}(x, y) \quad \text{for } l \in [0, L; \text{even}],\ m \in [0, l\ ; \text{even}]
\end{aligned} \tag{A.5.1}$$

within a node, with the boundary condition:

$$\varphi^{S}_{nr,\, l,\, m,\, g}(x, y) = 0 \tag{A.5.2}$$

at the node interface. Equation (A.5.1) is the same as the 2D transport equation except that the source term is replaced by $S^{\infty}_{l,\, m,\, g}(x, y)\ P_{nr}(x, y)$. Here

$S^{\infty}_{l,\, m,\, g}(x, y)$: group-g neutron source term obtained by the single assembly, infinite-lattice case

$P_{nr}(x, y)$: 2D Legendre polynomial of degree nr, defined within a node

As we assume that the source term is isotropic,

$$S^{\infty}_{l,\, m,\, g}(x, y) = S^{\infty}_{0,\, 0,\, g}(x, y)\ \delta_{l,\, 0}\ \delta_{m,\, 0} \tag{A.5.3}$$

A.6 Calculation of Boundary Value Expansion Function

The real boundary value expansion function can be calculated in the same way as the 2D case by solving the equation:

$$\begin{aligned}
&\sum_{m' = m-2,\, m+2:\ \text{even}} D_{l,\, m;\, l+2,\, m',\, g}(x, y)\ \varphi^{CB}_{pp,\, lmcq,\, l+2,\, m',\, g}(x, y) \\
&+ \sum_{m' = m-2,\, m+2:\ \text{even}} D_{l,\, m;\, l,\, m',\, g}(x, y)\ \varphi^{CB}_{pp,\, lmcq,\, l,\, m',\, g}(x, y) \\
&+ \sum_{m' = m-2,\, m+2:\ \text{even}} D_{l,\, m;\, l-2,\, m',\, g}(x, y)\ \varphi^{CB}_{pp,\, lmcq,\, l-2,\, m',\, g}(x, y) \\
&+ \Sigma^{r}_{l,\, m,\, g}(x, y)\ \varphi^{CB}_{pp,\, lmcq,\, l,\, m,\, g}(x, y) \\
&= 0 \qquad \text{for } l \in [0, L; \text{even}],\ m \in [0, l\ ; \text{even}]
\end{aligned} \tag{A.6.1}$$

within a node, with the boundary condition:

$$\varphi^{CB}_{pp,\, lmcq,\, l,\, m,\, g}(x, y) = \delta_{pp,\, qq}\ \delta_{il,\, l}\ \delta_{im,\, m}\ P_{sr}(s_{pp}) \tag{A.6.2}$$

or

$$\varphi^{CB}_{pp,\, lmcq,\, l,\, m,\, g}(x, y) = \delta_{pp,\, qq}\ \delta_{il,\, l}\ \delta_{im,\, m}\ P_{sr}(s_{pp})\ \phi^{c,inf}_{l,\, m,\, g}(s_{pp}) \quad \text{for } il = im = 0 \tag{A.6.3}$$

on the node interfaces qq = XL, XR, YL, YR, where

$P_{sr}(s_{pp})$: 1D Legendre polynomial of degree $sr \in [0, Sr]$, defined on node interface pp

s_{pp}: 1D (x or y) coordinate taken along node interface pp

$\phi^{c,inf}_{l,\, m,\, g}(s_{pp})$: g-th group neutron flux moment of angular indices (l, m) obtained by the single assembly, infinite-lattice case

Here pp = XL, XR, YL, YR, lmcq = (il, im, sr) and $il \in [0, L; \text{even}]$, $im \in [0, il\ ; \text{even}]$.

The imaginary boundary value expansion function $\varphi^{SB}_{pp,\,lmsq,\,l,\,m,\,g}(\mathbf{r})$ is defined by the solution of

$$\begin{aligned}
&\sum_{m' = m-2,\,m+2:\,even} D_{l,\,m;\,l+2,\,m',\,g}(x, y)\,\varphi^{SB}_{pp,\,lmsq,\,l+2,\,m',\,g}(x, y) \\
&+ \sum_{m' = m-2,\,m+2:\,even} D_{l,\,m;\,l,\,m',\,g}(x, y)\,\varphi^{SB}_{pp,\,lmsq,\,l,\,m',\,g}(x, y) \\
&+ \sum_{m' = m-2,\,m+2:\,even} D_{l,\,m;\,l-2,\,m',\,g}(x, y)\,\varphi^{SB}_{pp,\,lmsq,\,l-2,\,m',\,g}(x, y) \\
&+ \Sigma^{r}_{l,\,m,\,g}(x, y)\,\varphi^{SB}_{pp,\,lmsq,\,l,\,m,\,g}(x, y) \\
&= 0 \qquad \text{for } l \in [0, L; \text{even}],\ m \in [0, l\,; \text{even}]
\end{aligned} \tag{A.6.4}$$

within a node, with the boundary condition:

$$\varphi^{SB}_{pp,\,lmsq,\,l,\,m,\,g}(x, y) = -\,i\,\delta_{pp,\,qq}\,\delta_{il,\,l}\,\delta_{im,\,m}\,P_{sr}(s_{pp}) \tag{A.6.5}$$

$$\text{or}\quad \varphi^{SB}_{pp,\,lmsq,\,l,\,m,\,g}(x, y) = -\,i\,\delta_{pp,\,qq}\,\delta_{il,\,l}\,\delta_{im,\,m}\,P_{sr}(s_{pp})\,\phi^{s,inf}_{l,\,m,\,g}(s_{pp}) \tag{A.6.6}$$

on the node interfaces qq = XL, XR, YL, YR, lmsq = (il, im, sr) where

$\phi^{s,inf}_{l,\,m,\,g}(s_{pp})$: $\phi^{s}_{l,\,m,\,g}(s_{pp})$ obtained by the single assembly, infinite-lattice case

A.7 Power density Calculation

By solving Equations (A.2.14), (A.3.16), (A.3.20), (A.4.7 through 9), (A.4.27 through 29) and similar equations of (A.3.16) and (A.3.20) for y-direction, we obtain the expansion coefficients of Eq.(A.1.1). From these coefficients (and expansion functions defined in Sections A.5 and A.6), we can calculate the flux moment $\phi_{l,\,m,\,g}(\mathbf{r})$ and associated quantities. From a practical viewpoint, the power density and the scalar flux are most important of them.

From Eq.(A.1.1), the scalar flux $\phi_{g}(\mathbf{r})$ is obtained by:

$$\begin{aligned}
\phi_{g}(\mathbf{r}) \;=\; &\sum_{nr,\,nz} F^{S}_{nr,\,nz,\,g}\,\varphi^{S}_{nr,\,0,\,0,\,g}(x, y)\,Rz_{nz}(z) \\
&+ \sum_{pp} \sum_{lmcq,\,nz} F^{CB}_{pp,\,lmcq,\,nz,\,g}\,\varphi^{CB}_{pp,\,lmcq,\,0,\,0,\,g}(x, y)\,Rz_{nz}(z) \\
&+ \sum_{pp} \sum_{lmsq,\,nz} F^{SB}_{pp,\,lmsq,\;nz,\,g}\,\varphi^{SB}_{pp,\,lmsq,\,0,\,0,\,g}(x, y)\,Rz_{nz}(z)
\end{aligned} \tag{A.7.1}$$

The fission power density P(**r**) is obtained by:

$$\begin{aligned}
P(\mathbf{r}) \;=\; &\sum_{nr,\,nz,\,g} F^{S}_{nr,\,nz,\,g}\,\Sigma f_{g}(\mathbf{r})\,\varphi^{S}_{nr,\,0,\,0,\,g}(x, y)\,Rz_{nz}(z) \\
&+ \sum_{pp} \sum_{lmcq,\,nz,\,g} F^{CB}_{pp,\,lmcq,\,nz,\,g}\,\Sigma f_{g}(\mathbf{r})\,\varphi^{CB}_{pp,\,lmcq,\,0,\,0,\,g}(x, y)\,Rz_{nz}(z) \\
&+ \sum_{pp} \sum_{lmsq,\,nz,\,g} F^{SB}_{pp,\,lmsq,\;nz,\,g}\,\Sigma f_{g}(\mathbf{r})\,\varphi^{SB}_{pp,\,lmsq,\,0,\,0,\,g}(x, y)\,Rz_{nz}(z)
\end{aligned} \tag{A.7.2}$$

where $\Sigma f_{g}(\mathbf{r})$ is the macro-cross section of the fission power generation.

If we define an operator of spatial averaging:

$$\langle f(\mathbf{r}) \rangle_{nreg} = \int_{nreg} f(\mathbf{r})\,dx\,dy\,dz \,/\, \int_{nreg} dx\,dy\,dz \tag{A.7.3}$$

where nreg means any spatial region in a node, the spatial average of the scalar flux $\phi_{nreg,\,g}$ and the power density $P_{nreg,\,g}$ in nreg are obtained by

$$\begin{aligned}\phi_{nreg,g} &= <\phi_g(\mathbf{r})>_{nreg} \\ &= \sum_{nr,nz} F^{S}_{nr,nz,g} <\varphi^{S}_{nr,0,0,g}(x,y)\, Rz_{nz}(z)>_{nreg} \\ &+ \sum_{pp}\sum_{lmcq,nz} F^{CB}_{pp,lmcq,nz,g} <\varphi^{CB}_{pp,lmcq,0,0,g}(x,y)\, Rz_{nz}(z)>_{nreg} \\ &+ \sum_{pp}\sum_{lmsq,nz} F^{SB}_{pp,lmsq,\ nz,g} <\varphi^{SB}_{pp,lmsq,0,0,g}(x,y)\, Rz_{nz}(z)>_{nreg}\end{aligned} \tag{A.7.4}$$

$$\begin{aligned}P_{nreg,g} &= <P(\mathbf{r})>_{nreg} \\ &= \sum_{nr,nz,g} F^{S}_{nr,nz,g} <\Sigma f_g(\mathbf{r})\,\varphi^{S}_{nr,0,0,g}(x,y)\, Rz_{nz}(z)>_{nreg} \\ &+ \sum_{pp}\sum_{lmcq,nz,g} F^{CB}_{pp,lmcq,nz,g} <\Sigma f_g(\mathbf{r})\,\varphi^{CB}_{pp,lmcq,0,0,g}(x,y)\, Rz_{nz}(z)>_{nreg} \\ &+ \sum_{pp}\sum_{lmsq,nz,g} F^{SB}_{pp,lmsq,\ nz,g} <\Sigma f_g(\mathbf{r})\,\varphi^{SB}_{pp,lmsq,0,0,g}(x,y)\, Rz_{nz}(z)>_{nreg}\end{aligned} \tag{A.7.5}$$

When we need to calculate the axial distribution of the fuel-rod powers within a node, we define

$$<f(\mathbf{r})>_{nrod} = \int_{nrod} f(\mathbf{r})\,dx\,dy \,/ \int_{nreg} dx\,dy \tag{A.7.6}$$

where nrod is the radial cross sectional area of a fuel rod. Operating this to Eq.(A.7.2), we obtain

$$\begin{aligned}P_{nrod,nz,g}(z) &= <P(\mathbf{r})>_{nrod} \\ &= \sum_{nr,nz,g} F^{S}_{nr,nz,g} <\Sigma f_g(\mathbf{r})\,\varphi^{S}_{nr,0,0,g}(x,y)>_{nrod} Rz_{nz}(z) \\ &+ \sum_{pp}\sum_{lmcq,nz,g} F^{CB}_{pp,lmcq,nz,g} <\Sigma f_g(\mathbf{r})\,\varphi^{CB}_{pp,lmcq,0,0,g}(x,y)>_{nrod} Rz_{nz}(z) \\ &+ \sum_{pp}\sum_{lmsq,nz,g} F^{SB}_{pp,lmsq,\ nz,g} <\Sigma f_g(\mathbf{r})\,\varphi^{SB}_{pp,lmsq,0,0,g}(x,y)>_{nrod} Rz_{nz}(z)\end{aligned} \tag{A.7.7}$$

As $Rz_{nz}(z)$ is a simple known function, we cal easily calculate axial distribution (z-dependence) of the power density within a node. From this we can obtain information on the power peaking etc.

Appendix B: Comparison for All Thimbles

B.1 Case 1

The following figures show the comparison of the measured and VNEM-calculated relative detector readings. Both are independently normalized so that the spatial average of the readings over all the measuring points becomes 1.0. Here in the figures:

■ : VNEM-calculated relative readings
— : Upper bound to the measured readings
— : Lower bound to the measured readings

The upper / lower bounds of the measured readings are defined by the maximum / minimum of the readings of the assemblies at the octant-symmetric positions in the core. The representative of the octant-symmetric positions (i, j) in the core is taken from the north-north-east portion (shown in Fig.1.5.2).

As in Fig.1.5.1, the horizontal axis indicates the axial measuring positions along a thimble that are numbered 1 through 60 from the top to the bottom of the core. The vertical axis indicates the relative detector readings in an arbitrary unit.

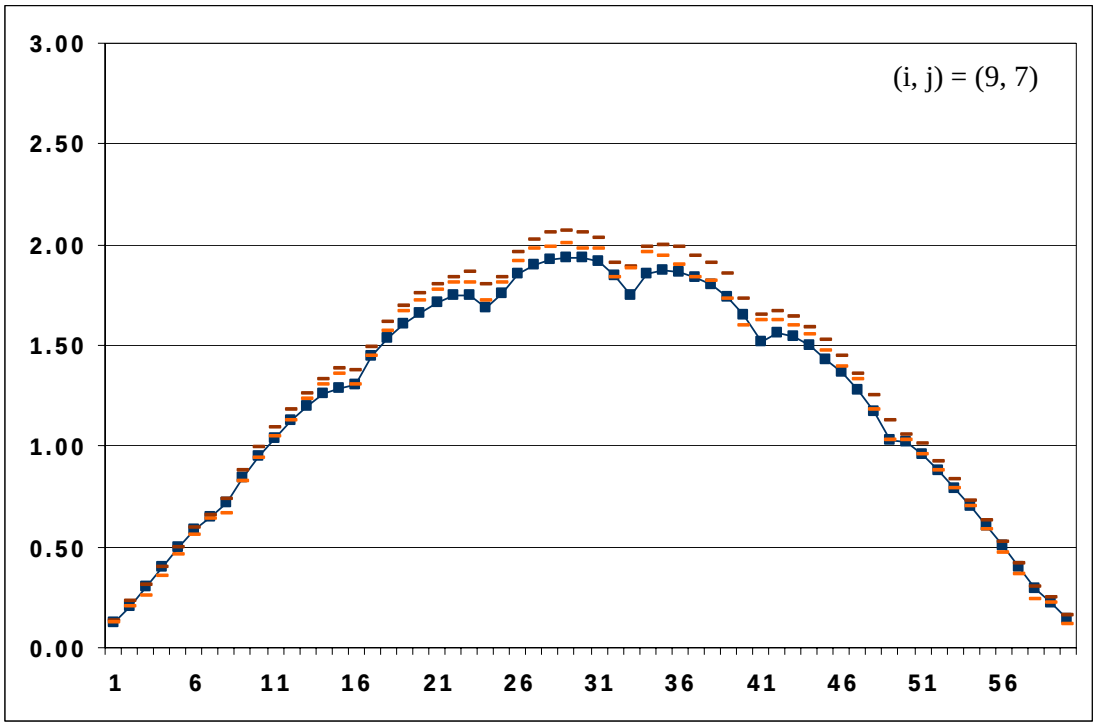
(i, j) = (9, 7)
3.00
2.50
2.00
1.50
1.00
0.50
0.00
1
6
11
16
21
26
31
36
41
46
51
56

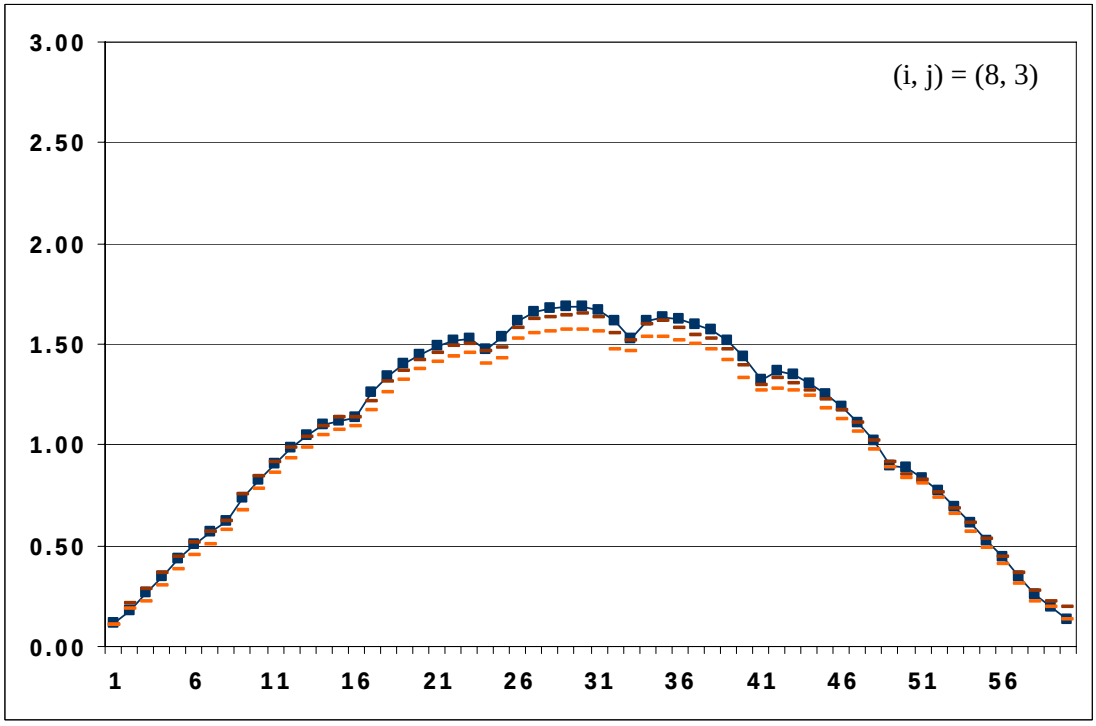
(i, j) = (8, 3)
3.00
2.50
2.00
1.50
1.00
0.50
0.00
1
6
11
16
21
26
31
36
41
46
51
56

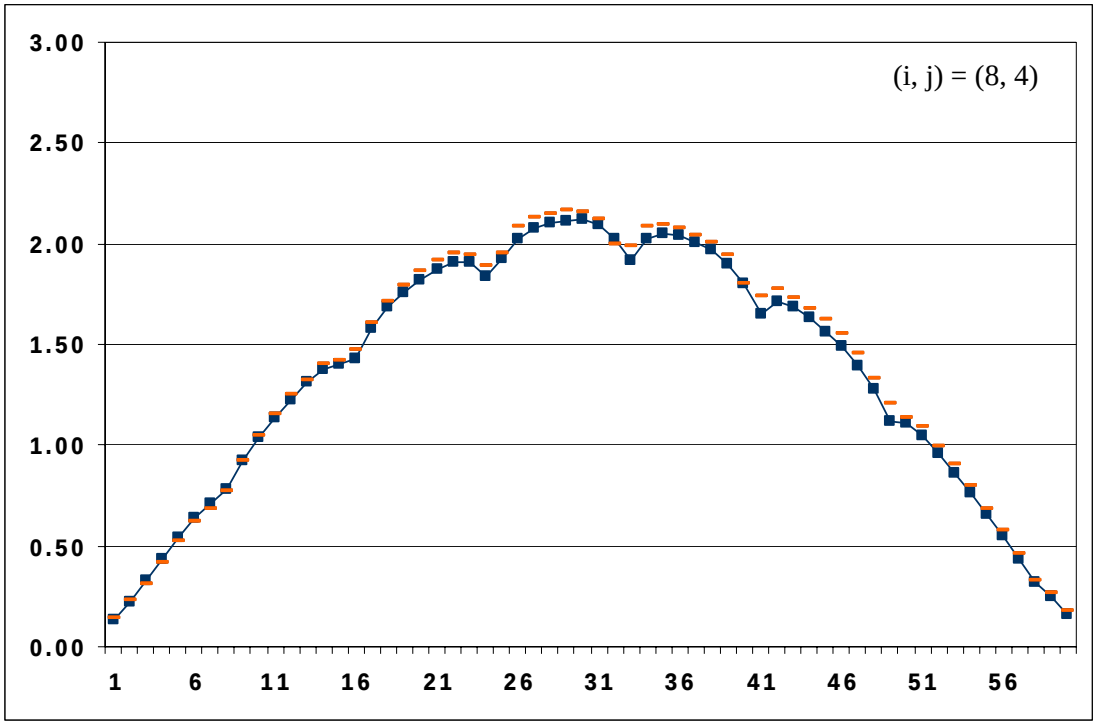
(i, j) = (8, 4)
3.00
2.50
2.00
1.50
1.00
0.50
0.00
1
6
11
16
21
26
31
36
41
46
51
56

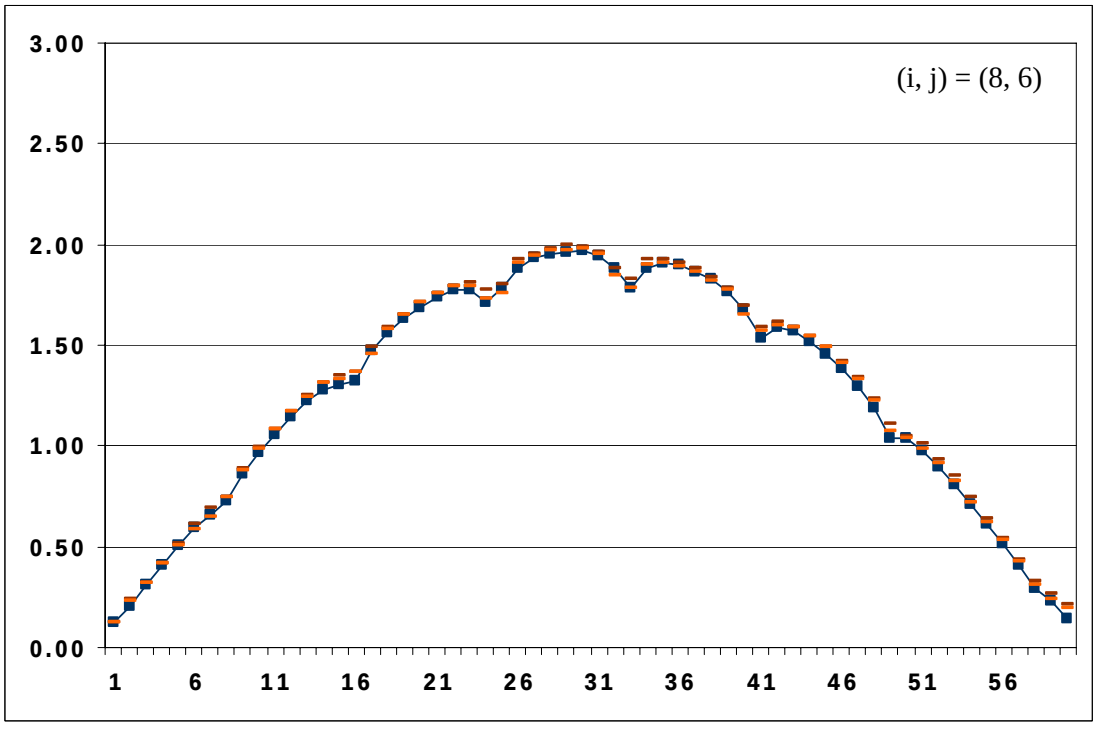
(i, j) = (8, 6)
3.00
2.50
2.00
1.50
1.00
0.50
0.00
1
6
11
16
21
26
31
36
41
46
51
56

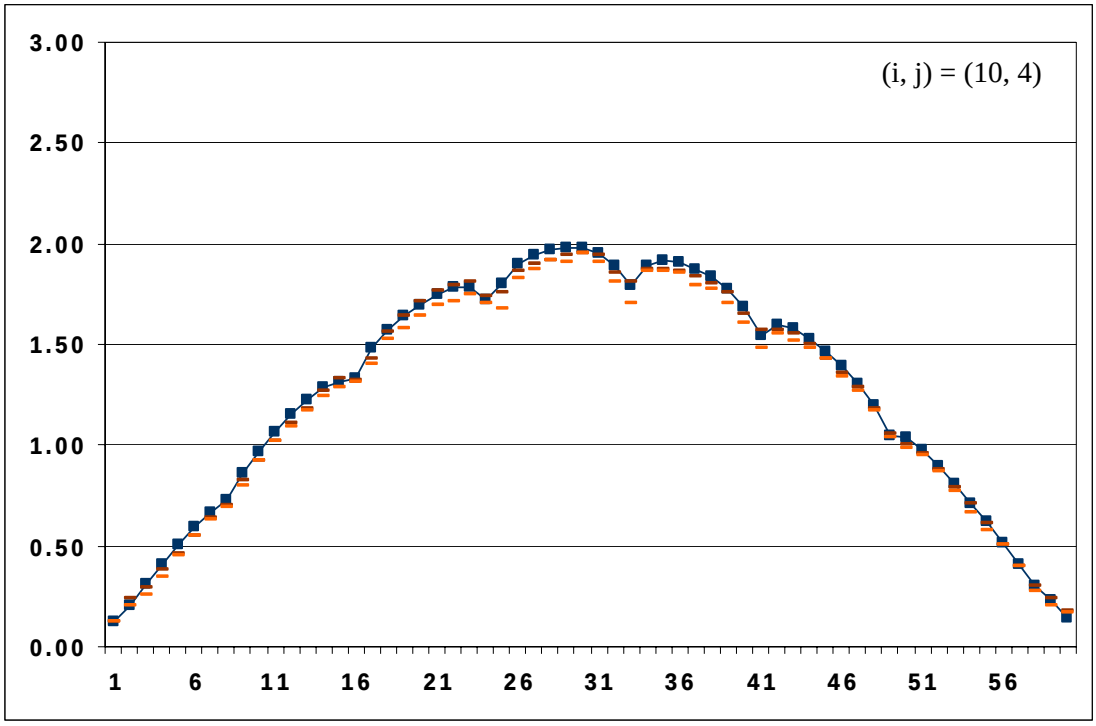
(i, j) = (10, 4)
3.00
2.50
2.00
1.50
1.00
0.50
0.00
1
6
11
16
21
26
31
36
41
46
51
56

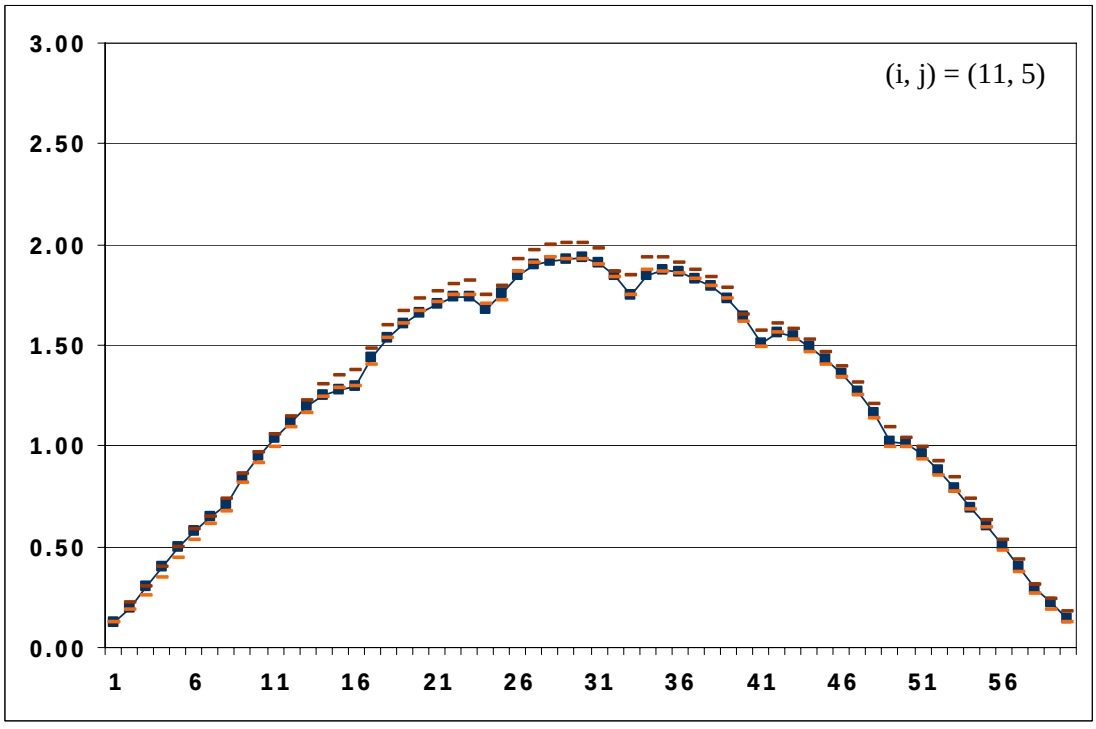
(i, j) = (11, 5)
3.00
2.50
2.00
1.50
1.00
0.50
0.00
1
6
11
16
21
26
31
36
41
46
51
56

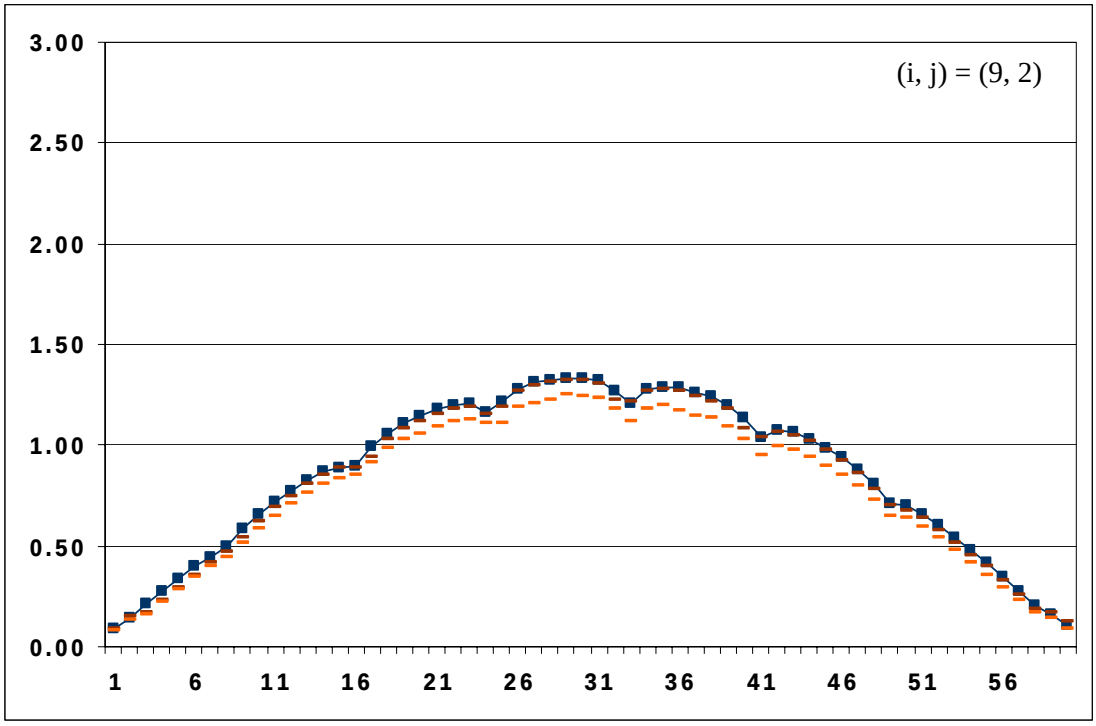
(i, j) = (9, 2)
3.00
2.50
2.00
1.50
1.00
0.50
0.00
1
6
11
16
21
26
31
36
41
46
51
56

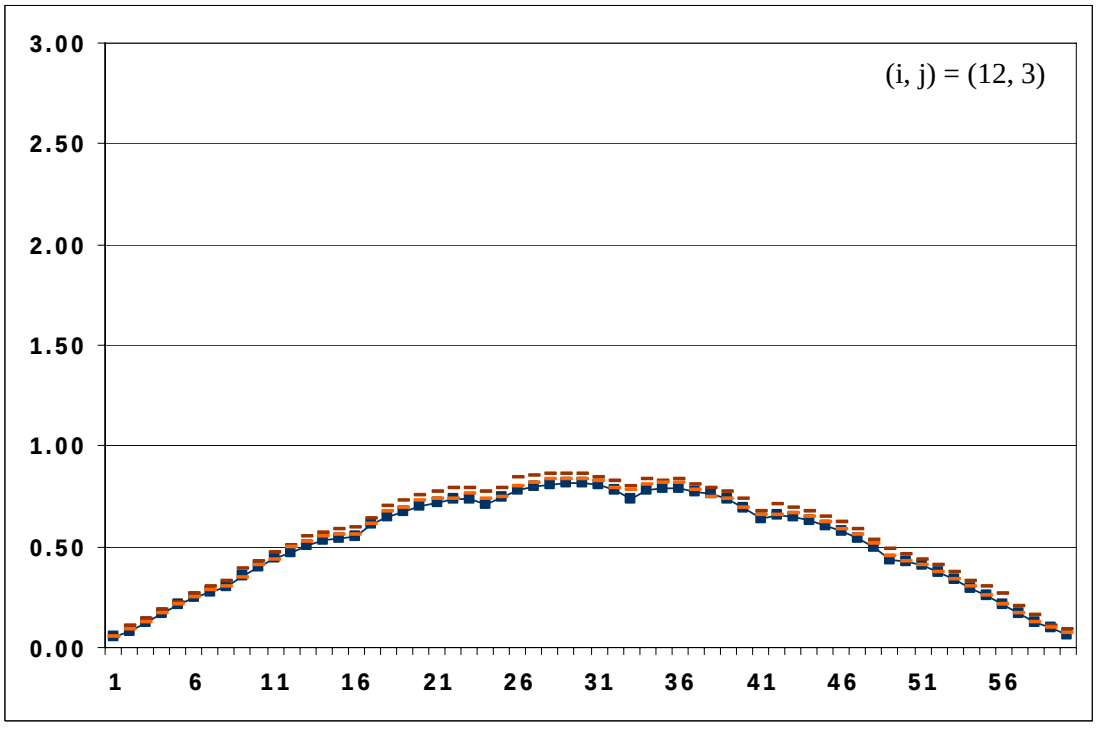
(i, j) = (12, 3)
3.00
2.50
2.00
1.50
1.00
0.50
0.00
1
6
11
16
21
26
31
36
41
46
51
56

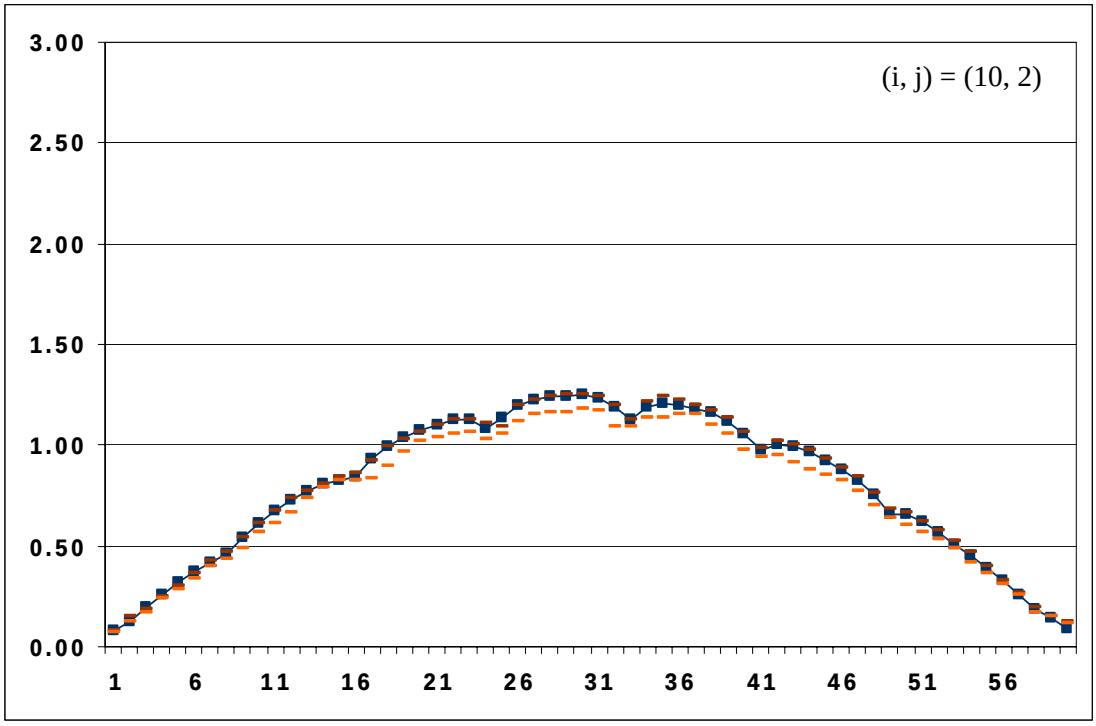
(i, j) = (10, 2)
3.00
2.50
2.00
1.50
1.00
0.50
0.00
1
6
11
16
21
26
31
36
41
46
51
56

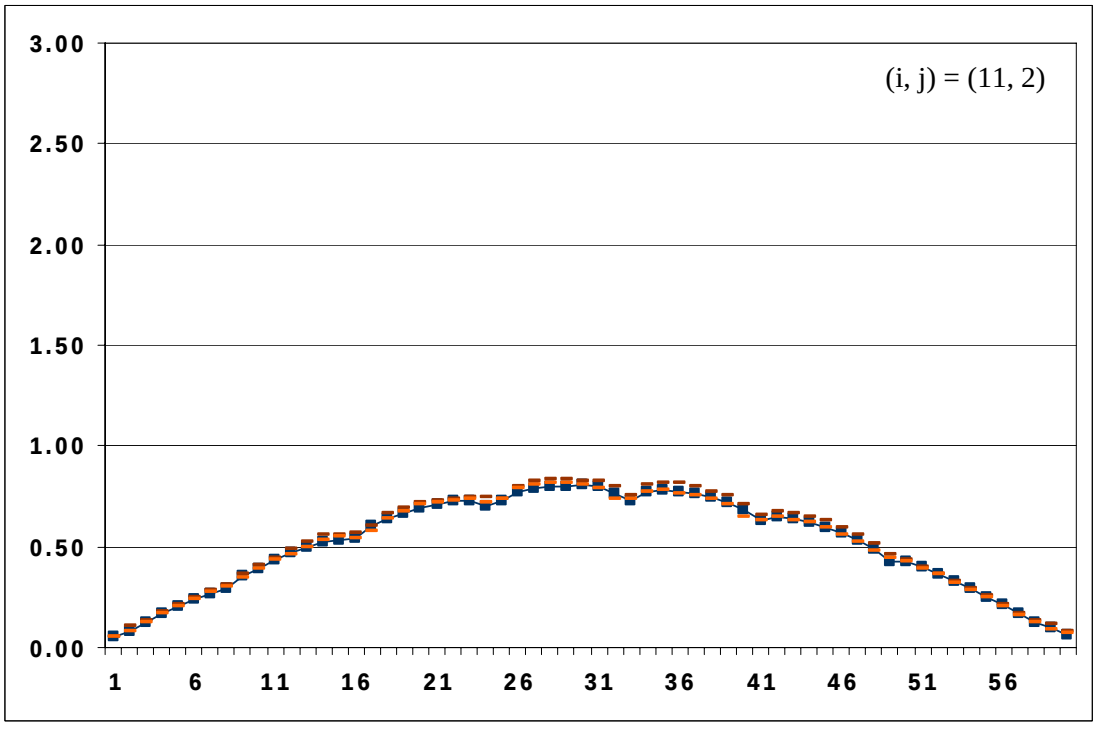
(i, j) = (11, 2)
3.00
2.50
2.00
1.50
1.00
0.50
0.00
1
6
11
16
21
26
31
36
41
46
51
56

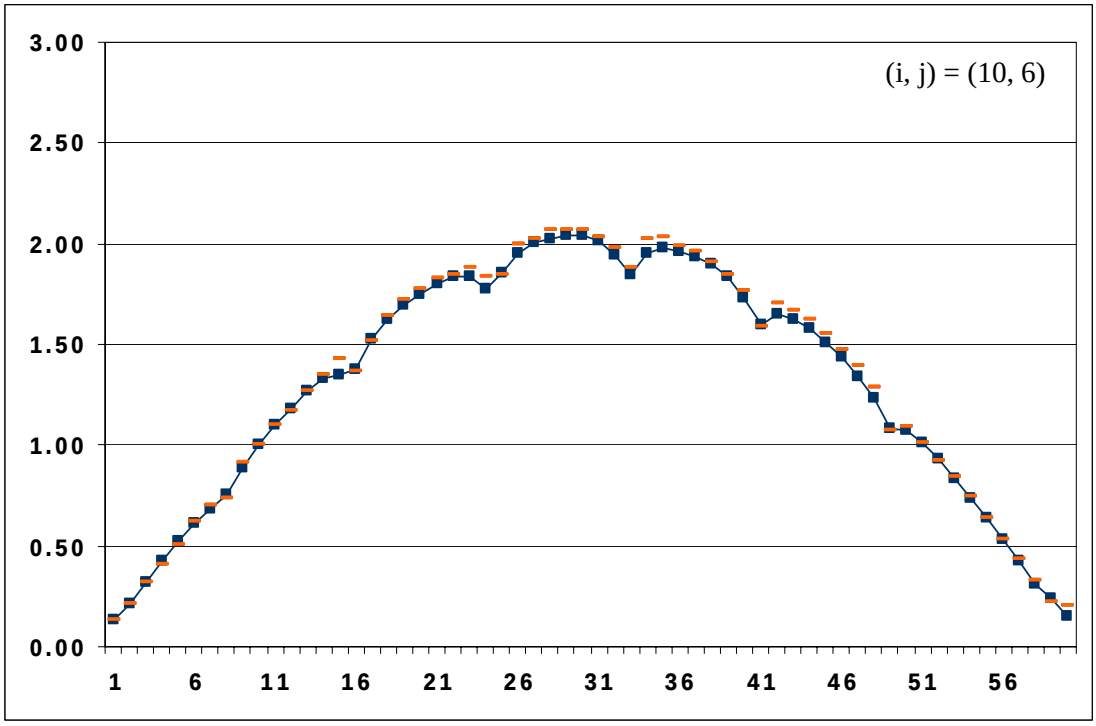
(i, j) = (10, 6)
3.00
2.50
2.00
1.50
1.00
0.50
0.00
1
6
11
16
21
26
31
36
41
46
51
56

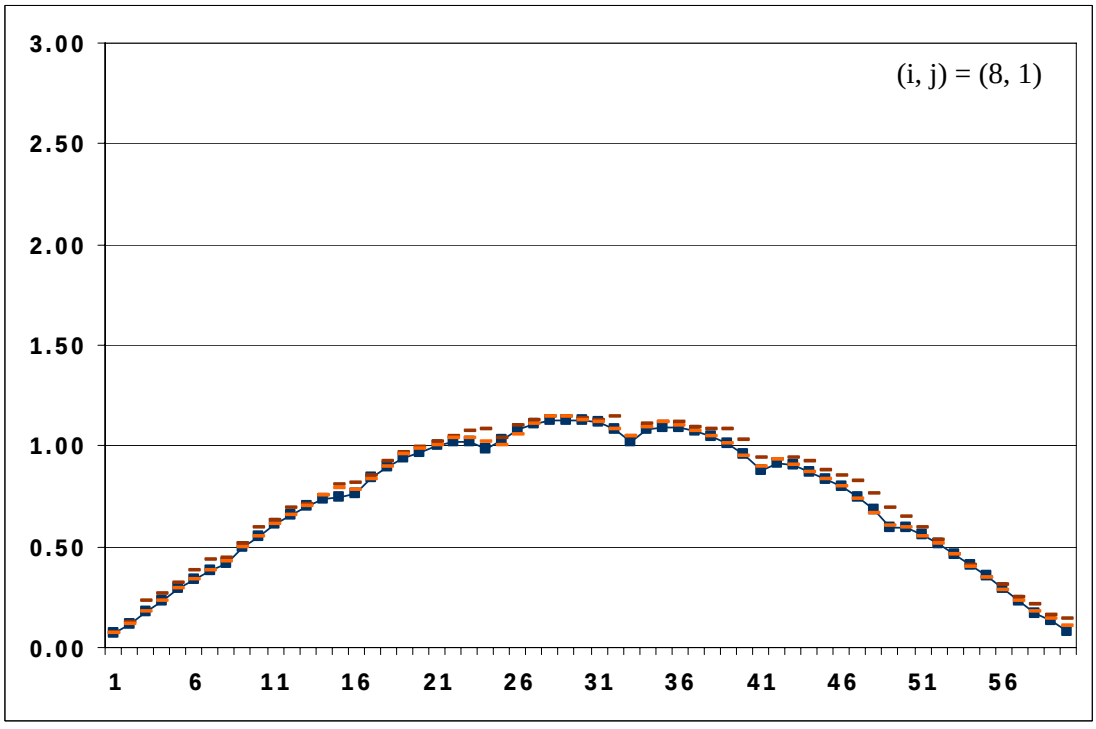
(i, j) = (8, 1)
3.00
2.50
2.00
1.50
1.00
0.50
0.00
1
6
11
16
21
26
31
36
41
46
51
56

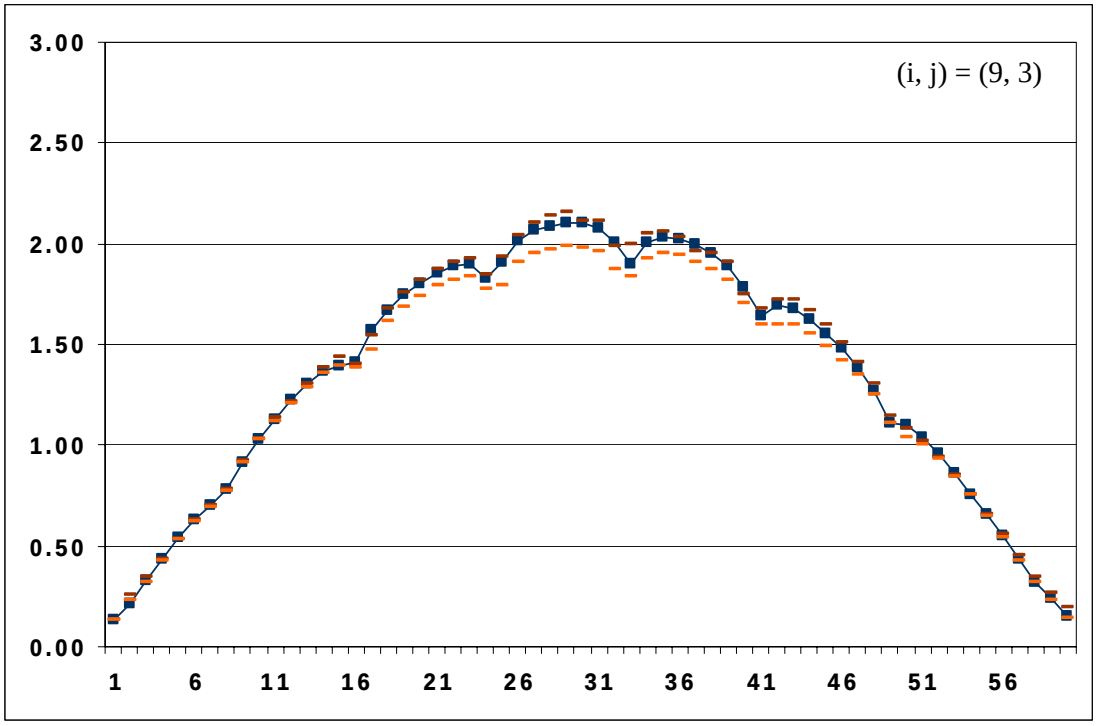
(i, j) = (9, 3)
3.00
2.50
2.00
1.50
1.00
0.50
0.00
1
6
11
16
21
26
31
36
41
46
51
56

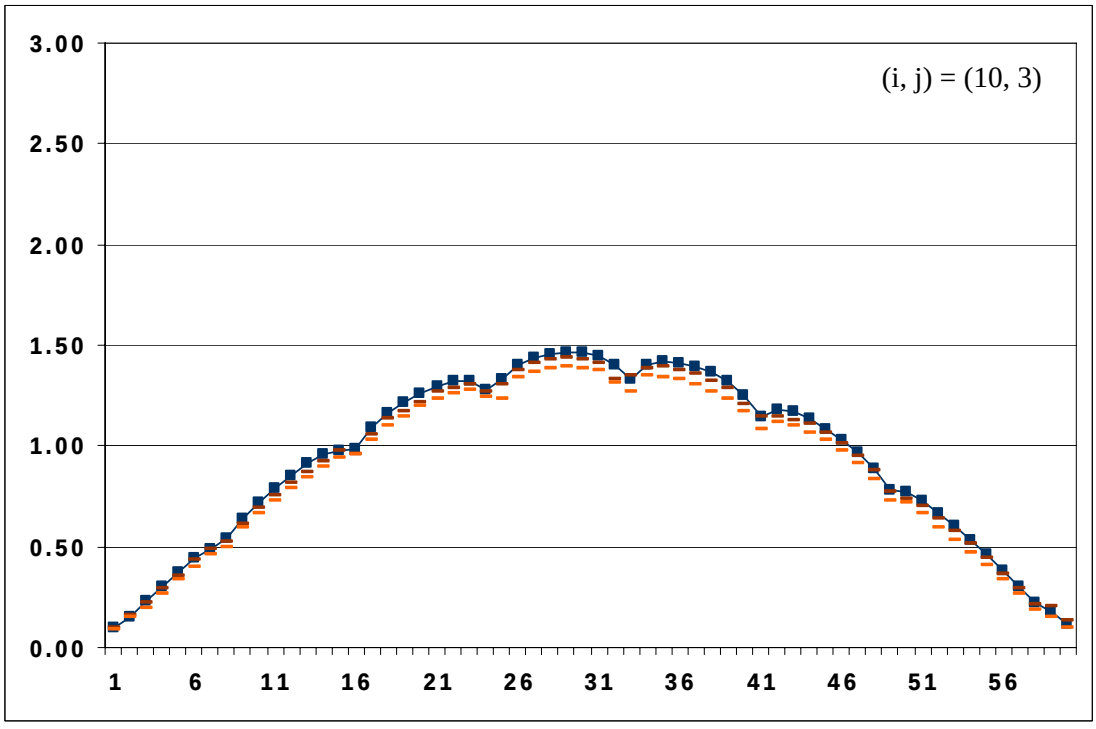
(i, j) = (10, 3)
3.00
2.50
2.00
1.50
1.00
0.50
0.00
1
6
11
16
21
26
31
36
41
46
51
56

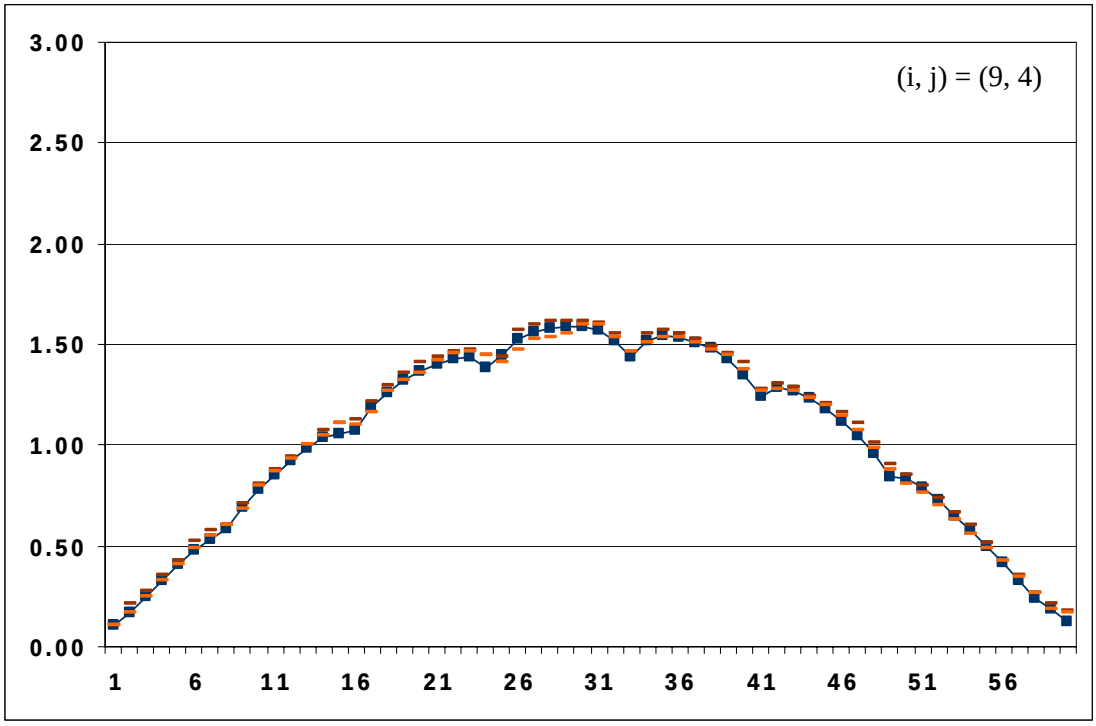
(i, j) = (9, 4)
3.00
2.50
2.00
1.50
1.00
0.50
0.00
1
6
11
16
21
26
31
36
41
46
51
56

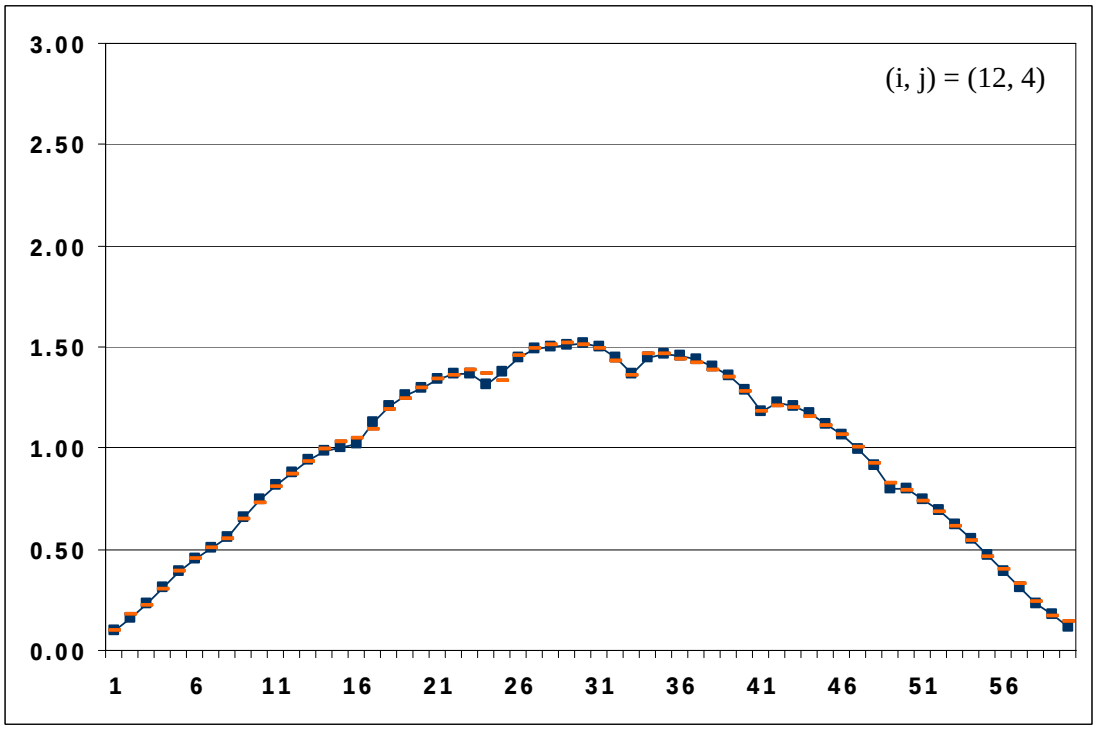
(i, j) = (12, 4)
3.00
2.50
2.00
1.50
1.00
0.50
0.00
1
6
11
16
21
26
31
36
41
46
51
56

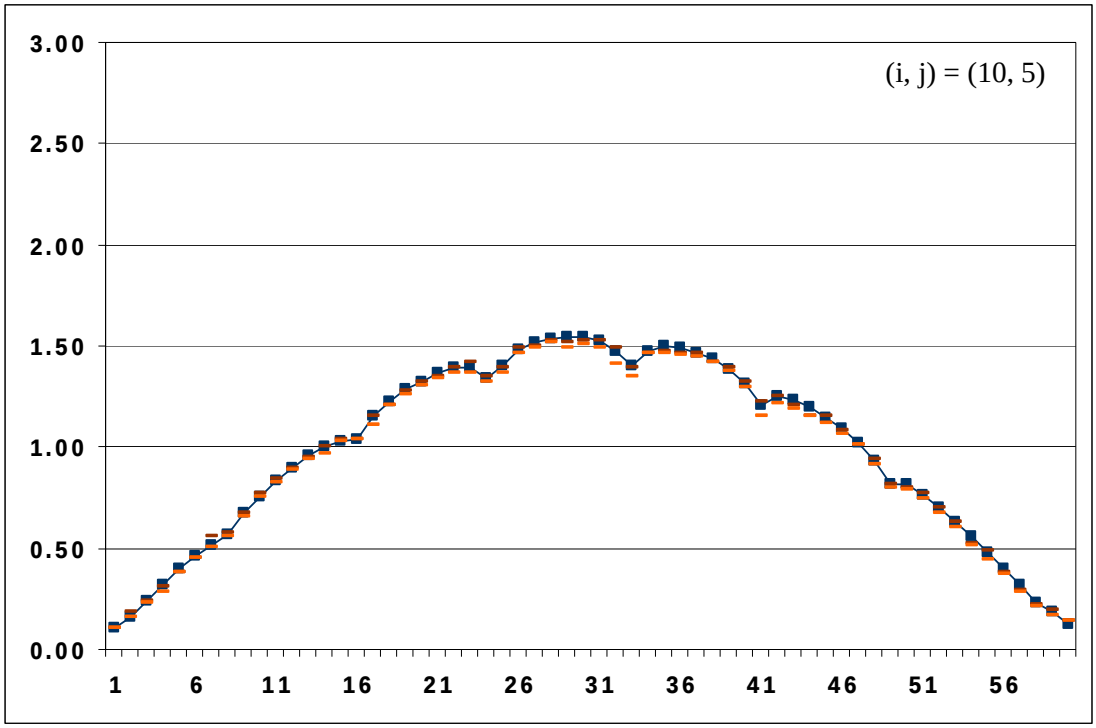
(i, j) = (10, 5)
3.00
2.50
2.00
1.50
1.00
0.50
0.00
1
6
11
16
21
26
31
36
41
46
51
56

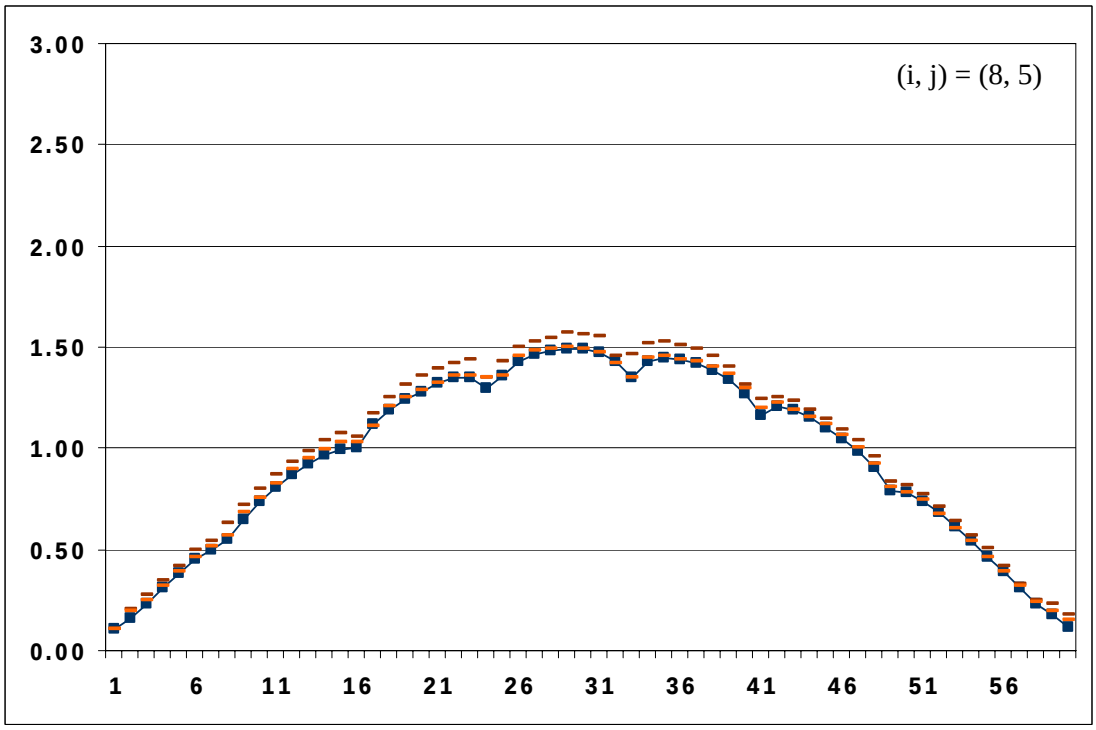
(i, j) = (8, 5)
3.00
2.50
2.00
1.50
1.00
0.50
0.00
1
6
11
16
21
26
31
36
41
46
51
56

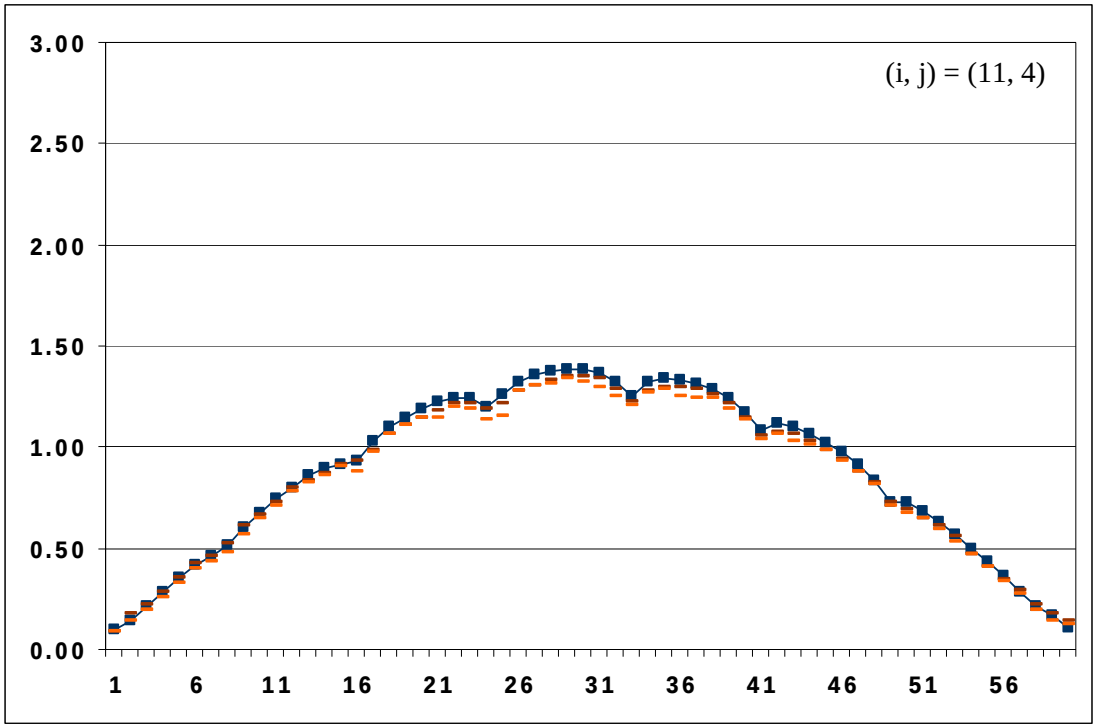
(i, j) = (11, 4)
3.00
2.50
2.00
1.50
1.00
0.50
0.00
1
6
11
16
21
26
31
36
41
46
51
56

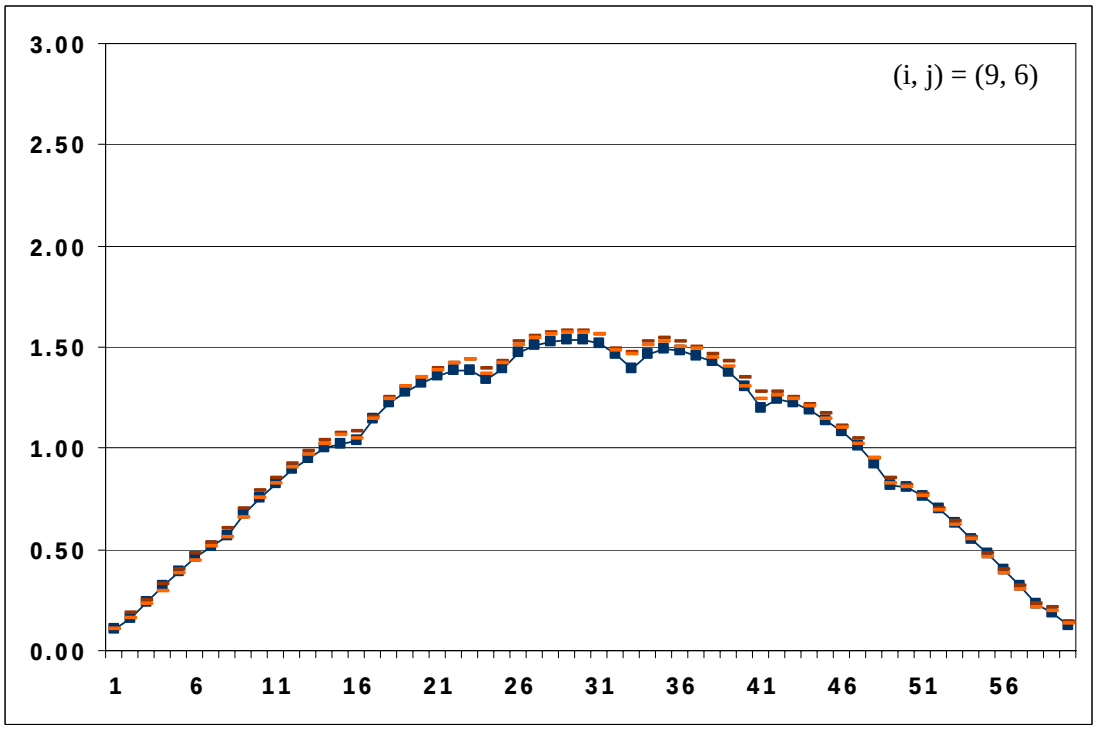
(i, j) = (9, 6)
3.00
2.50
2.00
1.50
1.00
0.50
0.00
1
6
11
16
21
26
31
36
41
46
51
56

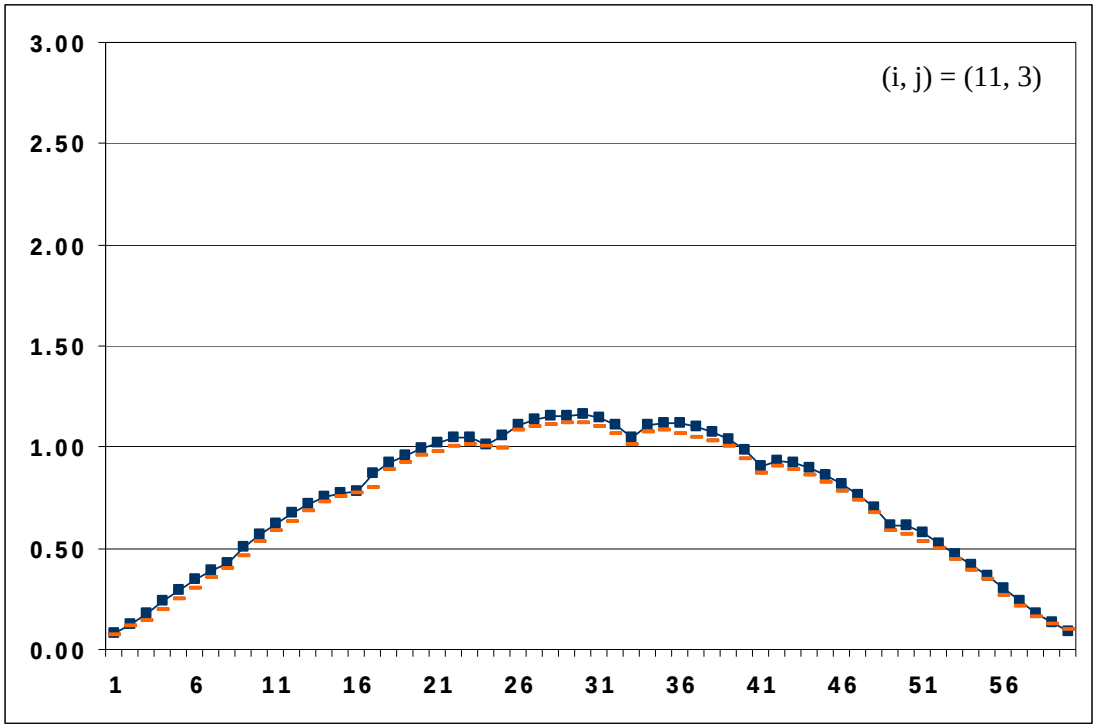
(i, j) = (11, 3)
3.00
2.50
2.00
1.50
1.00
0.50
0.00
1
6
11
16
21
26
31
36
41
46
51
56

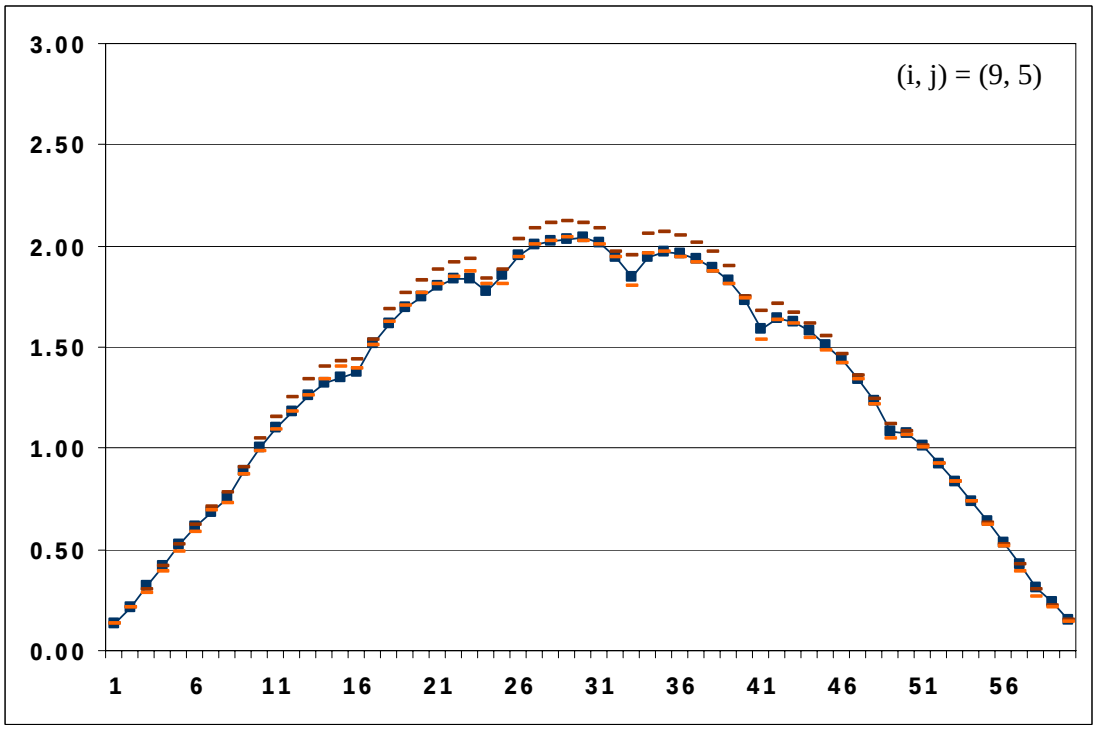
(i, j) = (9, 5)
3.00
2.50
2.00
1.50
1.00
0.50
0.00
1
6
11
16
21
26
31
36
41
46
51
56

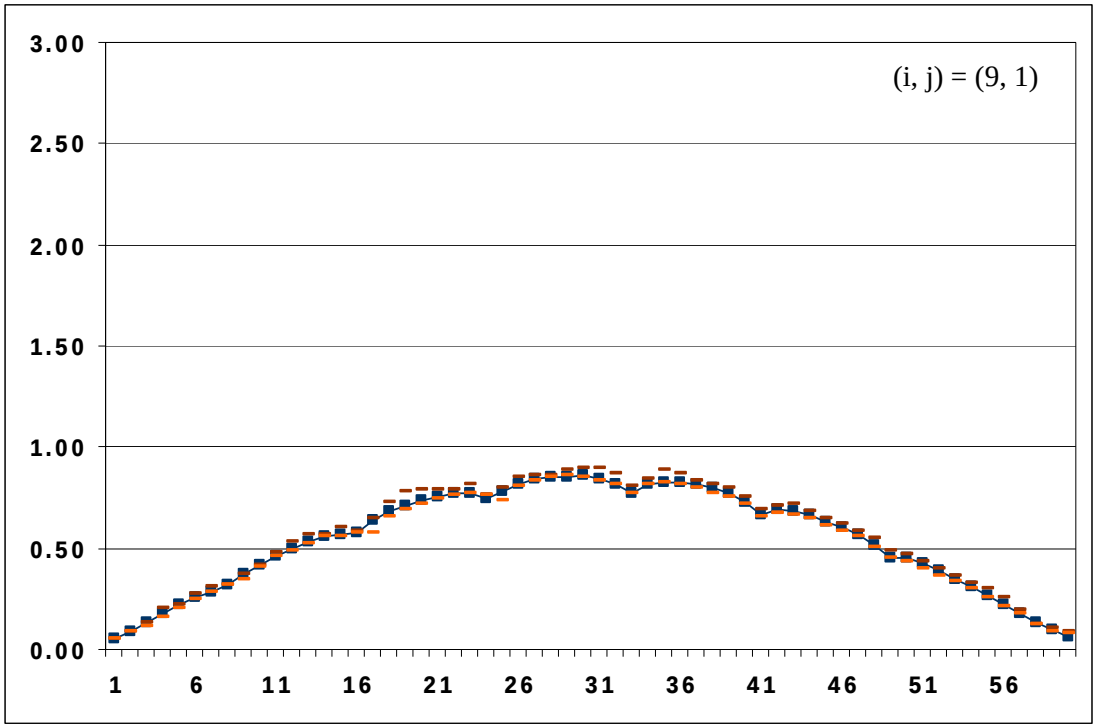
(i, j) = (9, 1)
3.00
2.50
2.00
1.50
1.00
0.50
0.00
1
6
11
16
21
26
31
36
41
46
51
56

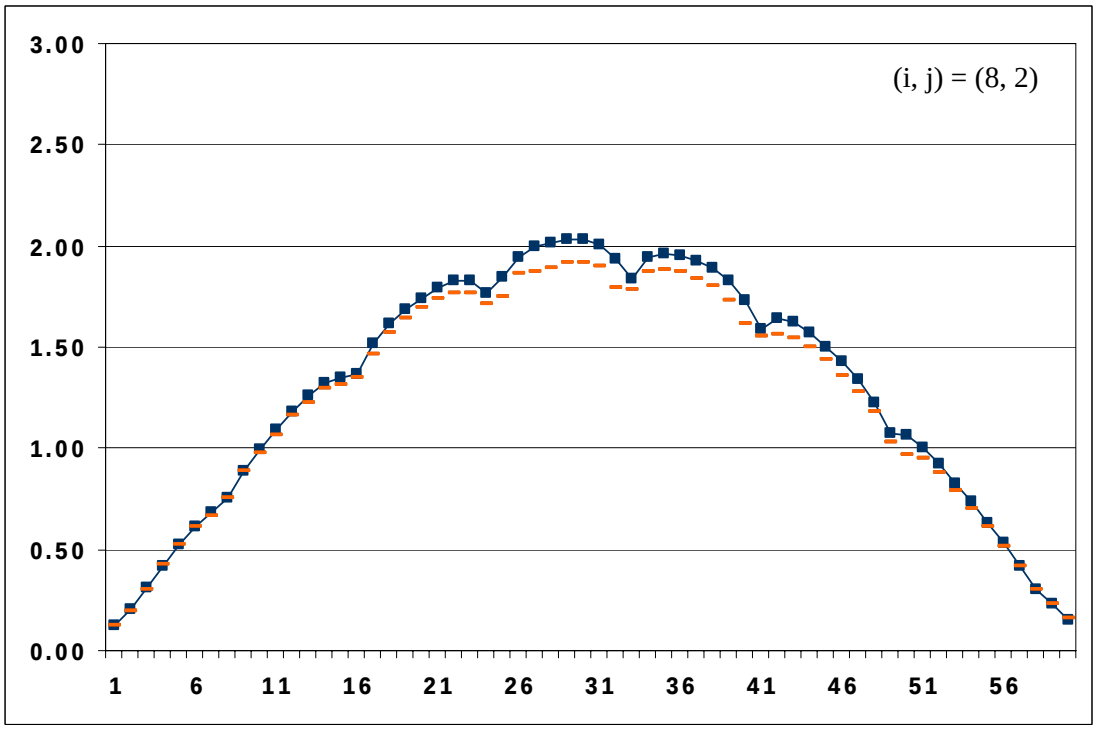
(i, j) = (8, 2)
3.00
2.50
2.00
1.50
1.00
0.50
0.00
1
6
11
16
21
26
31
36
41
46
51
56

B.2 Case 2

The following figures show the comparison of the measured and VNEM-calculated relative detector readings. Both are independently normalized so that the spatial average of the readings over all the measuring points becomes 1.0. Here in the figures:

- ■ : VNEM-calculated relative readings
- — : Upper bound to the measured readings
- — : Lower bound to the measured readings

The upper / lower bounds of the measured readings are defined by the maximum / minimum of the readings of the assemblies at the octant-symmetric positions in the core. The representative of the octant-symmetric positions (i, j) in the core is taken from the north-north-east portion (shown in Fig.1.5.5).

As in Fig.1.5.4, the horizontal axis indicates the axial measuring positions along a thimble that are numbered 1 through 60 from the top to the bottom of the core. The vertical axis indicates the relative detector readings in an arbitrary unit.

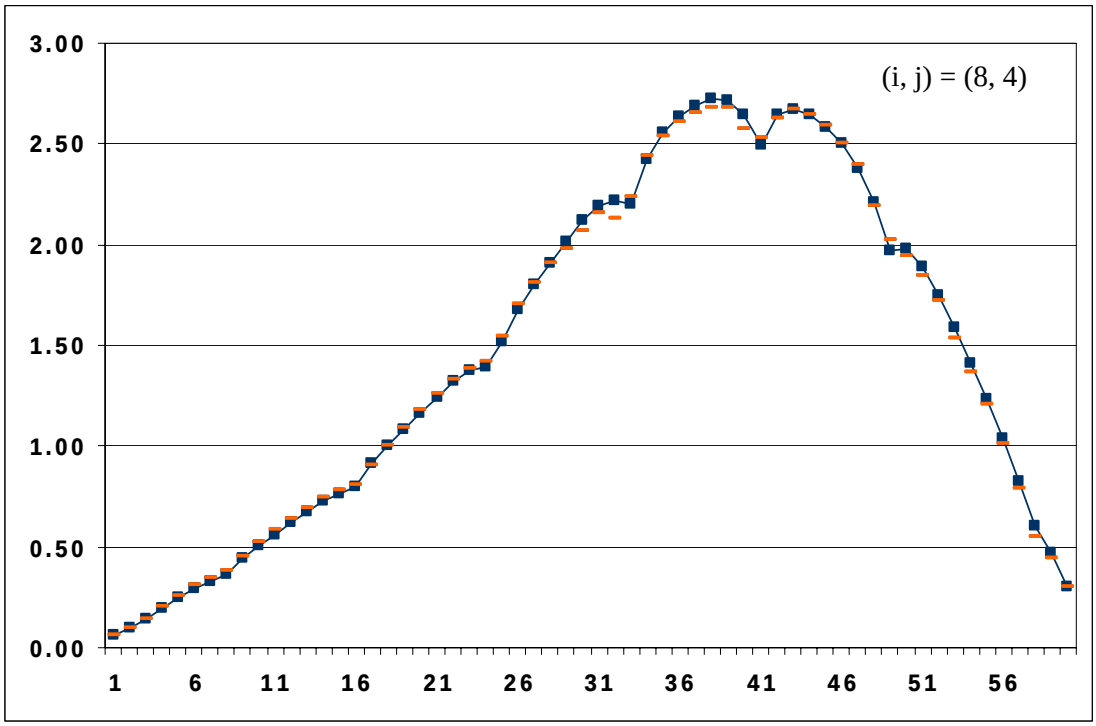
(i, j) = (8, 4)
3.00
2.50
2.00
1.50
1.00
0.50
0.00
1
6
11
16
21
26
31
36
41
46
51
56

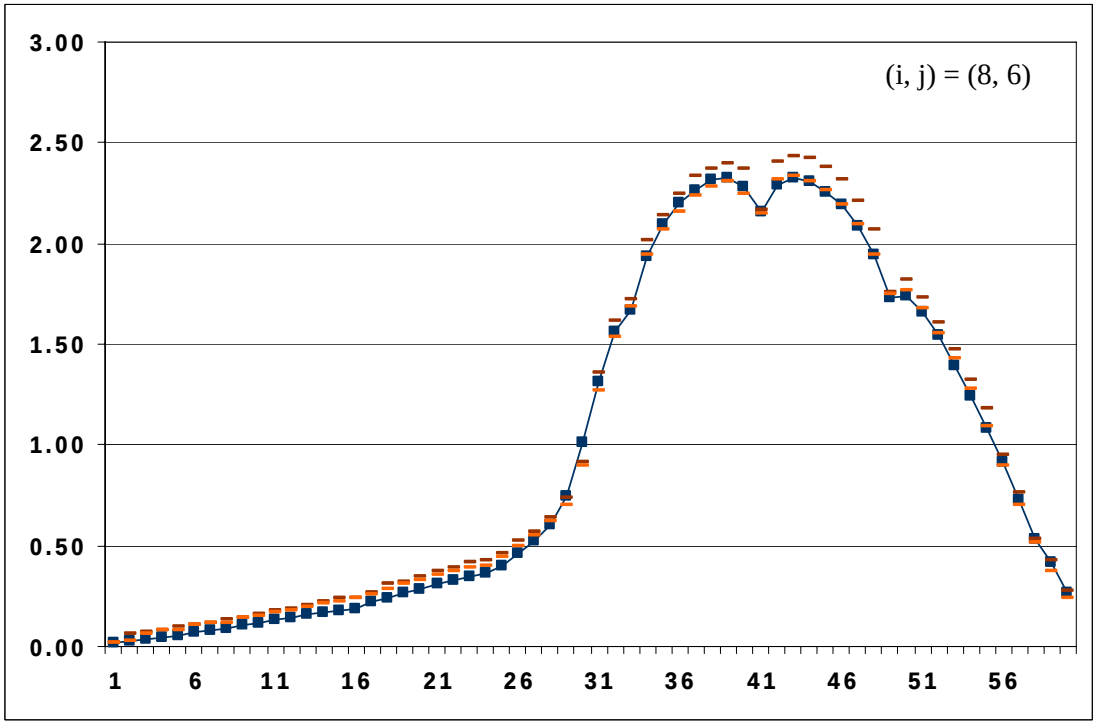
(i, j) = (8, 6)
3.00
2.50
2.00
1.50
1.00
0.50
0.00
1
6
11
16
21
26
31
36
41
46
51
56

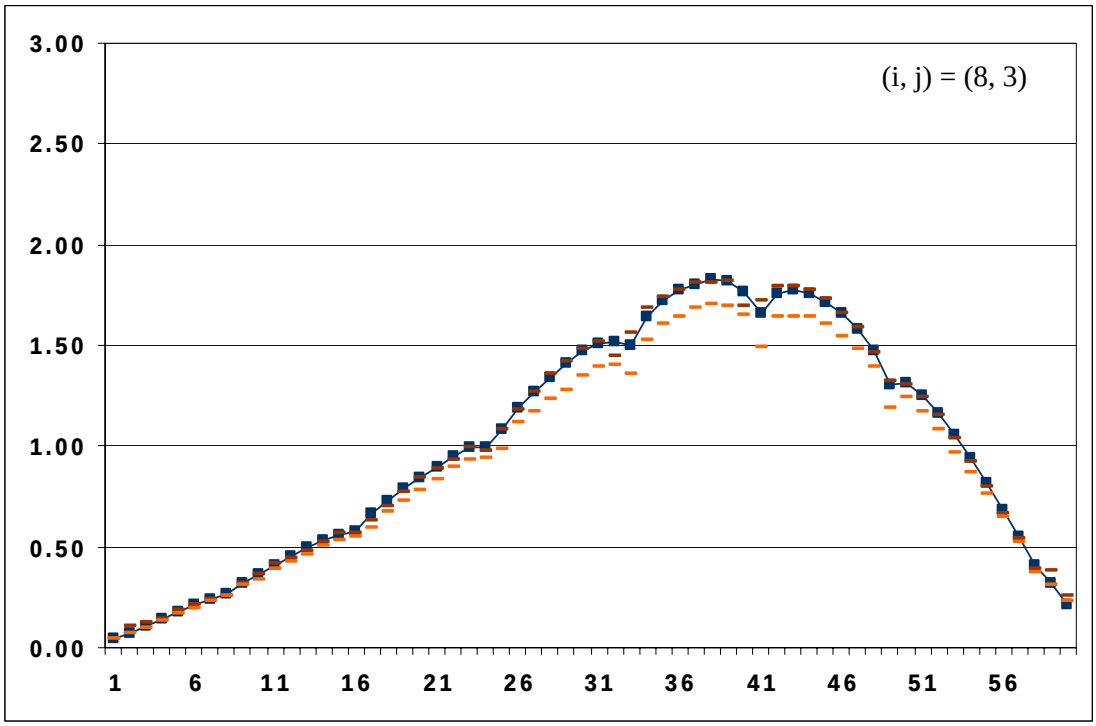
(i, j) = (8, 3)
3.00
2.50
2.00
1.50
1.00
0.50
0.00
1
6
11
16
21
26
31
36
41
46
51
56

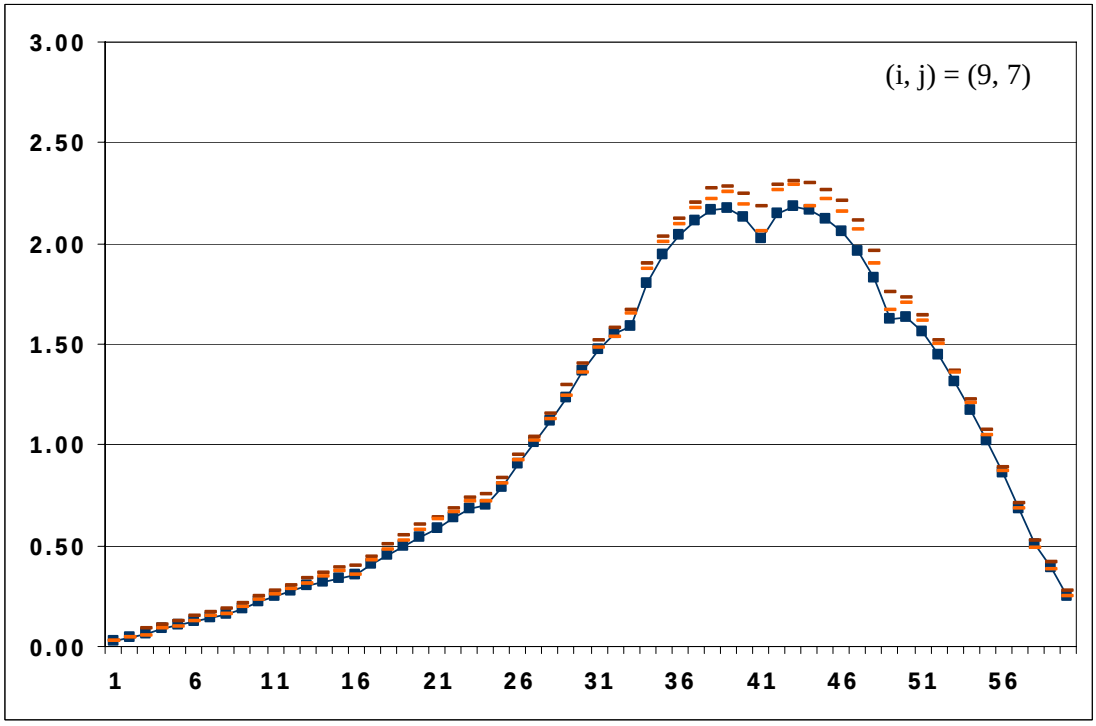
(i, j) = (9, 7)
3.00
2.50
2.00
1.50
1.00
0.50
0.00
1
6
11
16
21
26
31
36
41
46
51
56

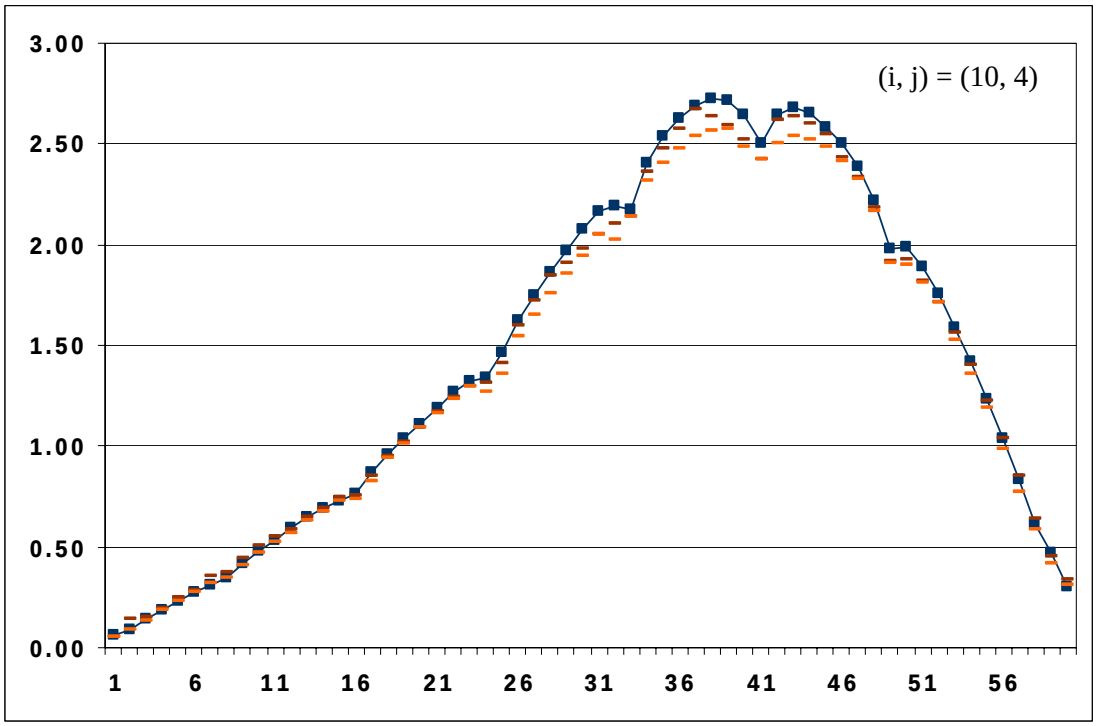
(i, j) = (10, 4)
3.00
2.50
2.00
1.50
1.00
0.50
0.00
1
6
11
16
21
26
31
36
41
46
51
56

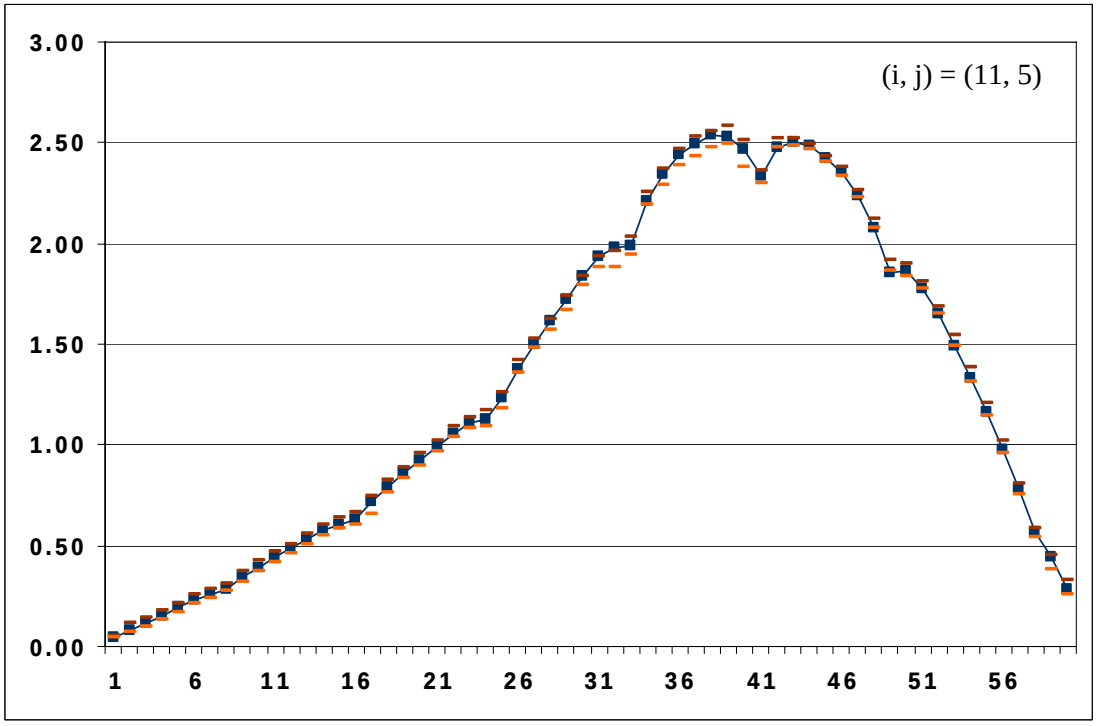
(i, j) = (11, 5)
3.00
2.50
2.00
1.50
1.00
0.50
0.00
1
6
11
16
21
26
31
36
41
46
51
56

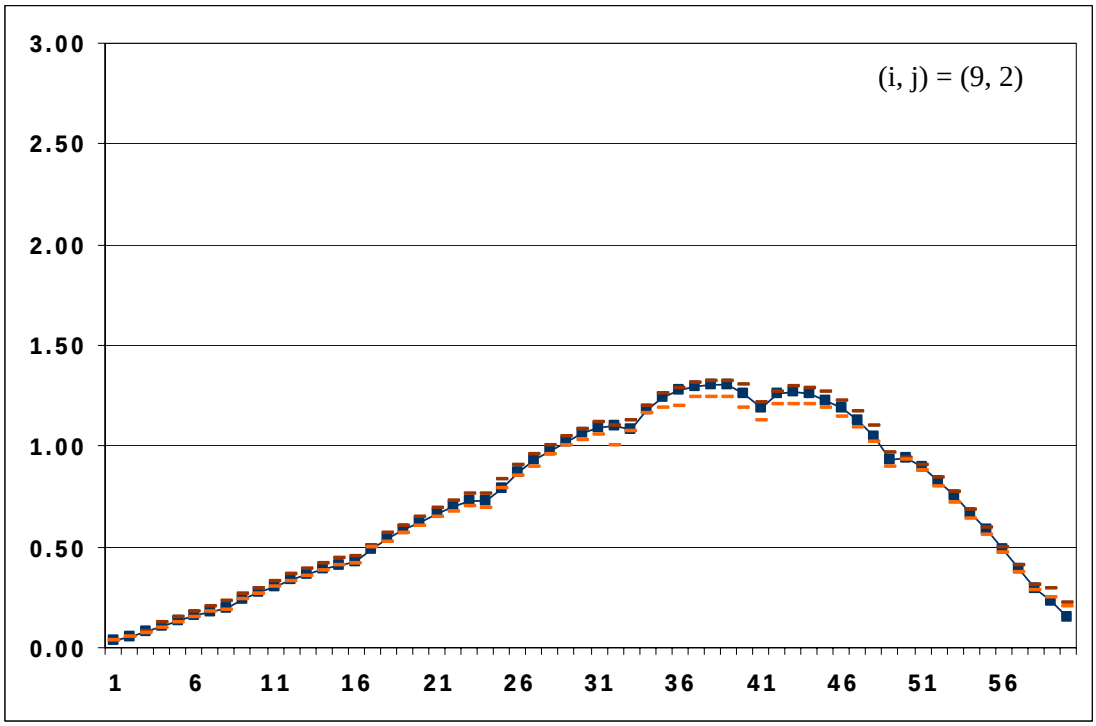
(i, j) = (9, 2)
3.00
2.50
2.00
1.50
1.00
0.50
0.00
1
6
11
16
21
26
31
36
41
46
51
56

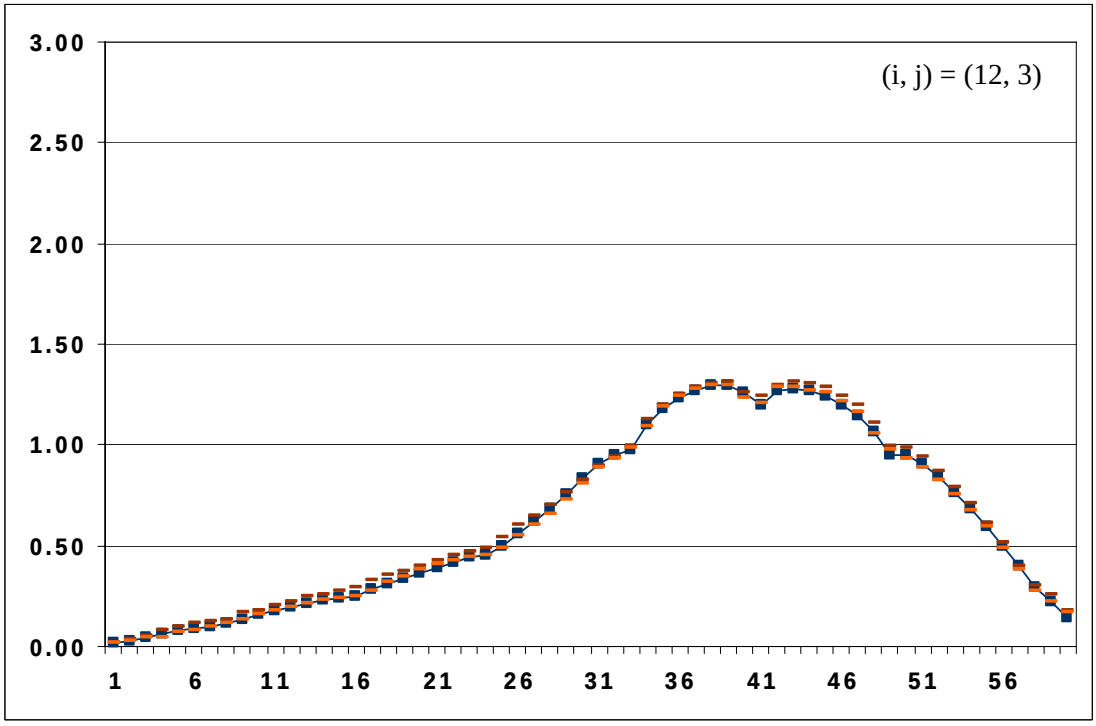
(i, j) = (12, 3)
3.00
2.50
2.00
1.50
1.00
0.50
0.00
1
6
11
16
21
26
31
36
41
46
51
56

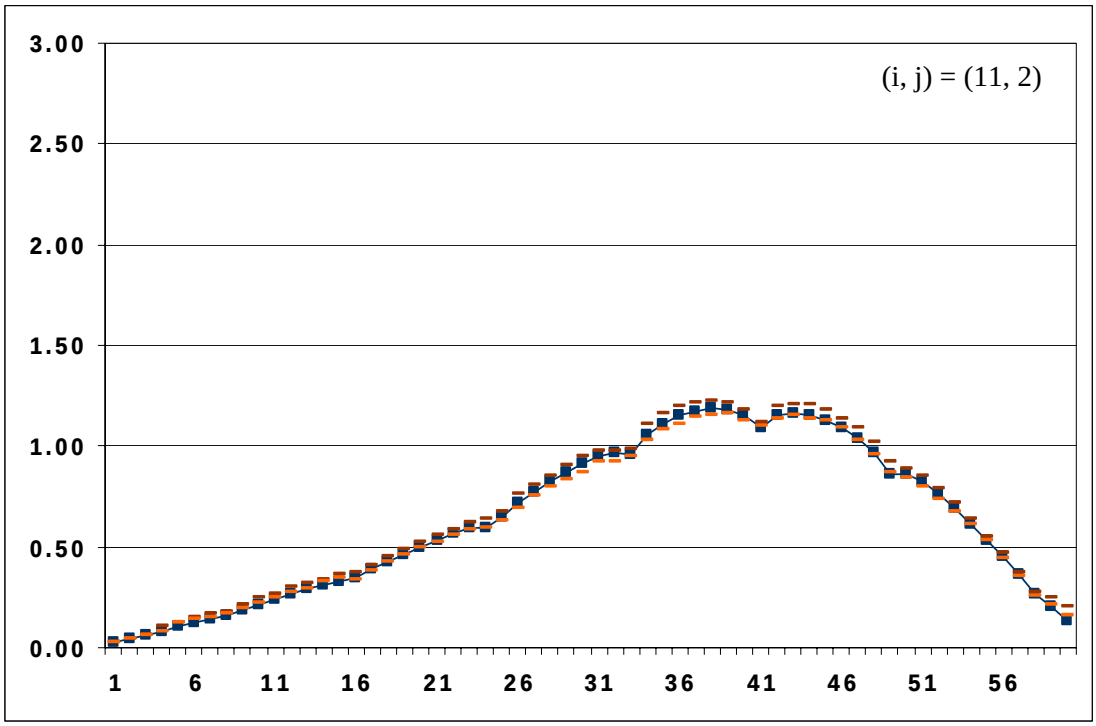
3.00
2.50
2.00
1.50
1.00
0.50
0.00
1
6
11
16
21
26
31
36
41
46
51
56
(i, j) = (11, 2)

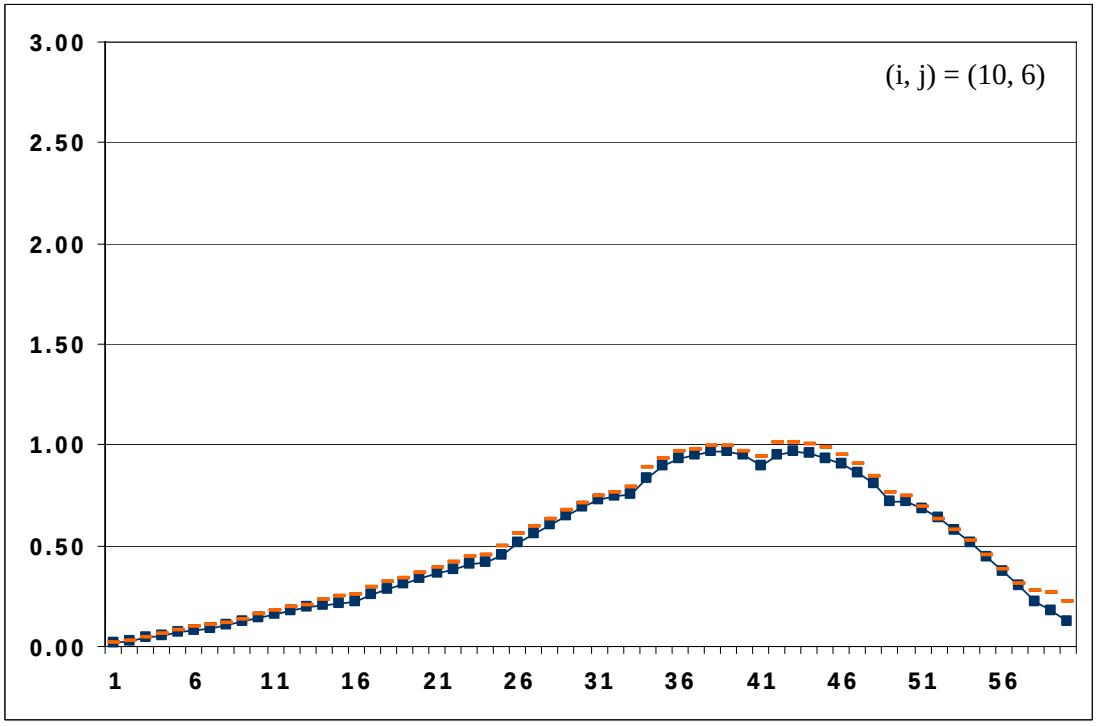
3.00
2.50
2.00
1.50
1.00
0.50
0.00
1
6
11
16
21
26
31
36
41
46
51
56
(i, j) = (10, 6)

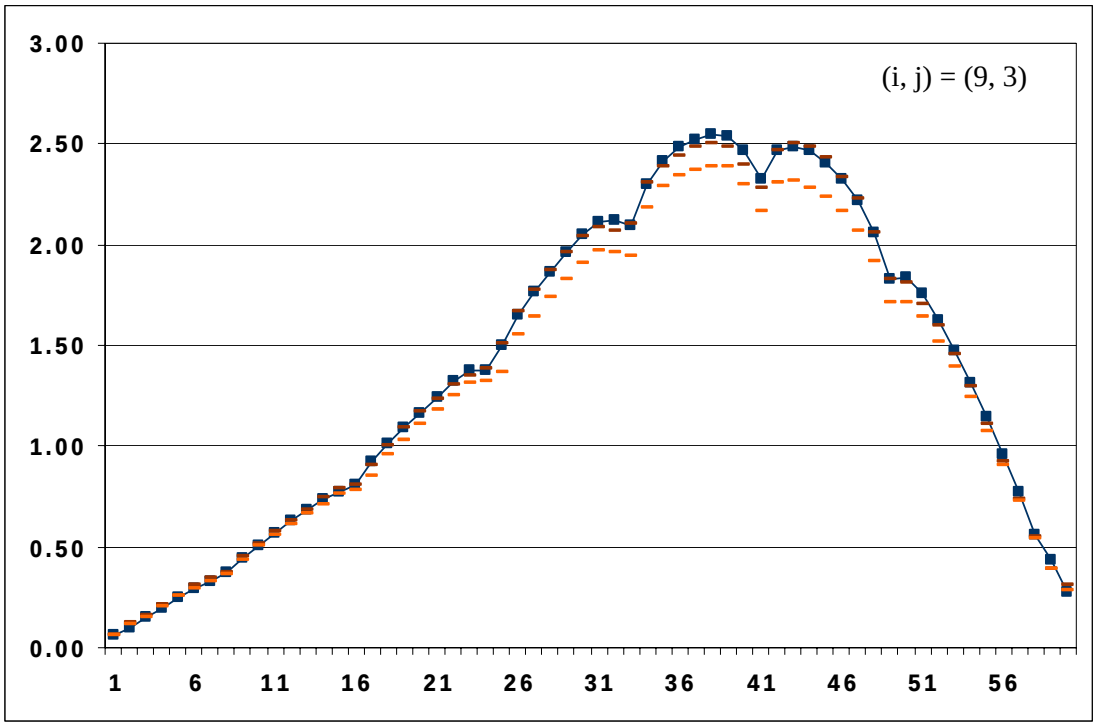
(i, j) = (9, 3)
3.00
2.50
2.00
1.50
1.00
0.50
0.00
1
6
11
16
21
26
31
36
41
46
51
56

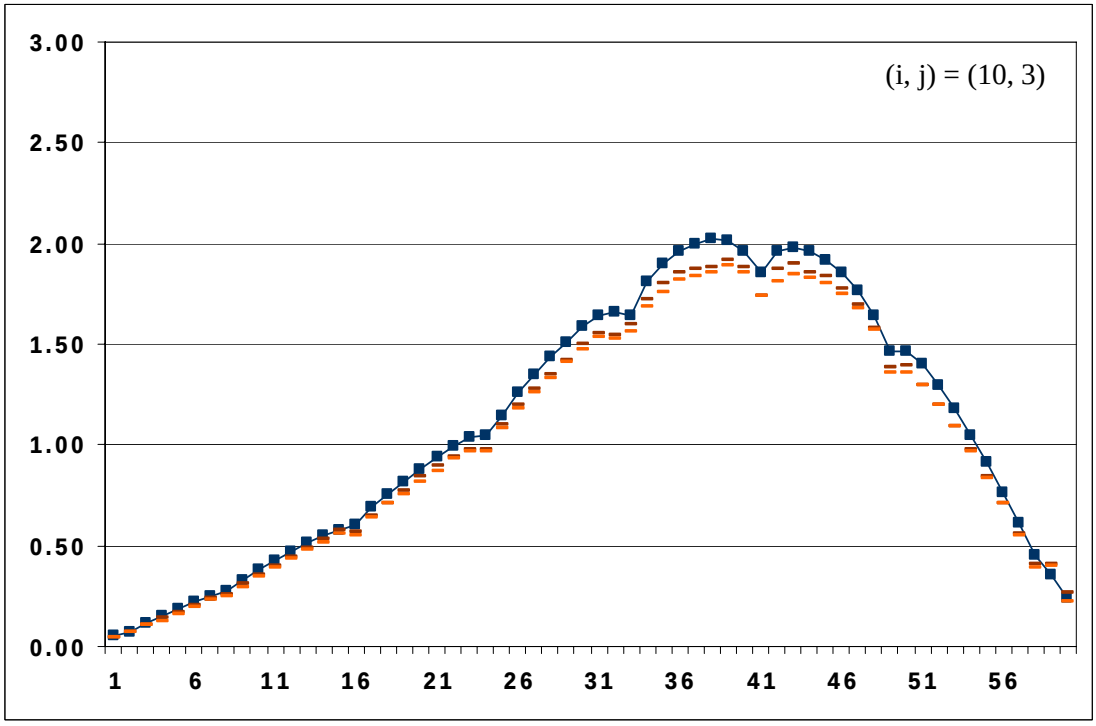
(i, j) = (10, 3)
3.00
2.50
2.00
1.50
1.00
0.50
0.00
1
6
11
16
21
26
31
36
41
46
51
56

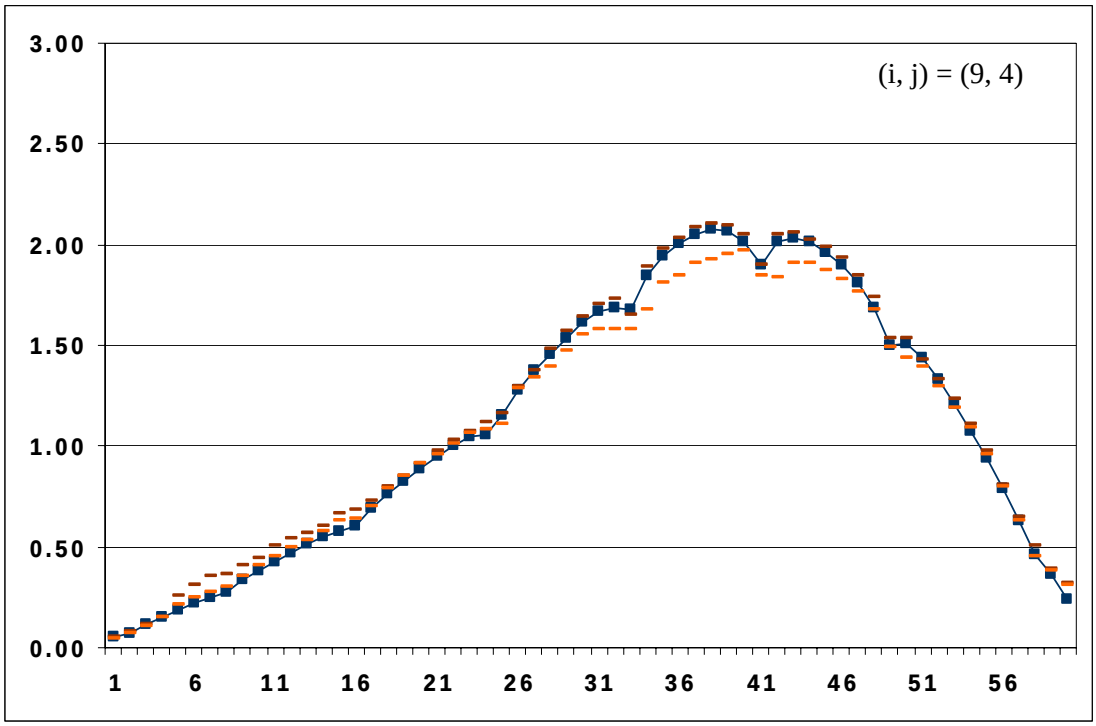
(i, j) = (9, 4)
3.00
2.50
2.00
1.50
1.00
0.50
0.00
1
6
11
16
21
26
31
36
41
46
51
56

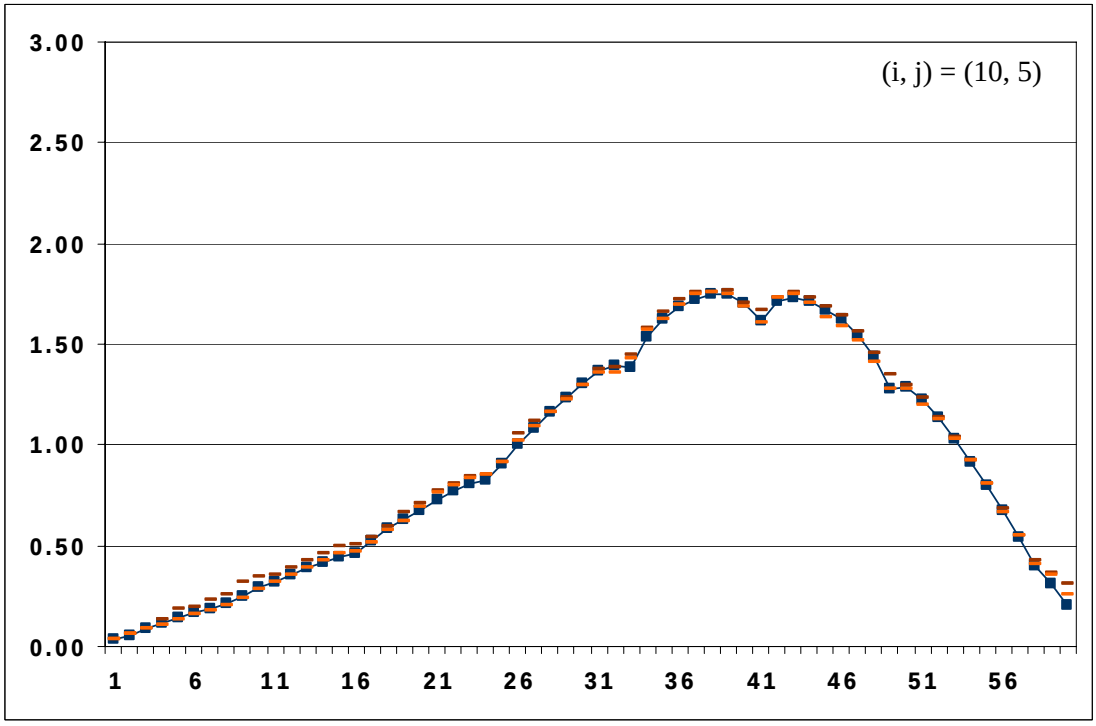
(i, j) = (10, 5)
3.00
2.50
2.00
1.50
1.00
0.50
0.00
1
6
11
16
21
26
31
36
41
46
51
56

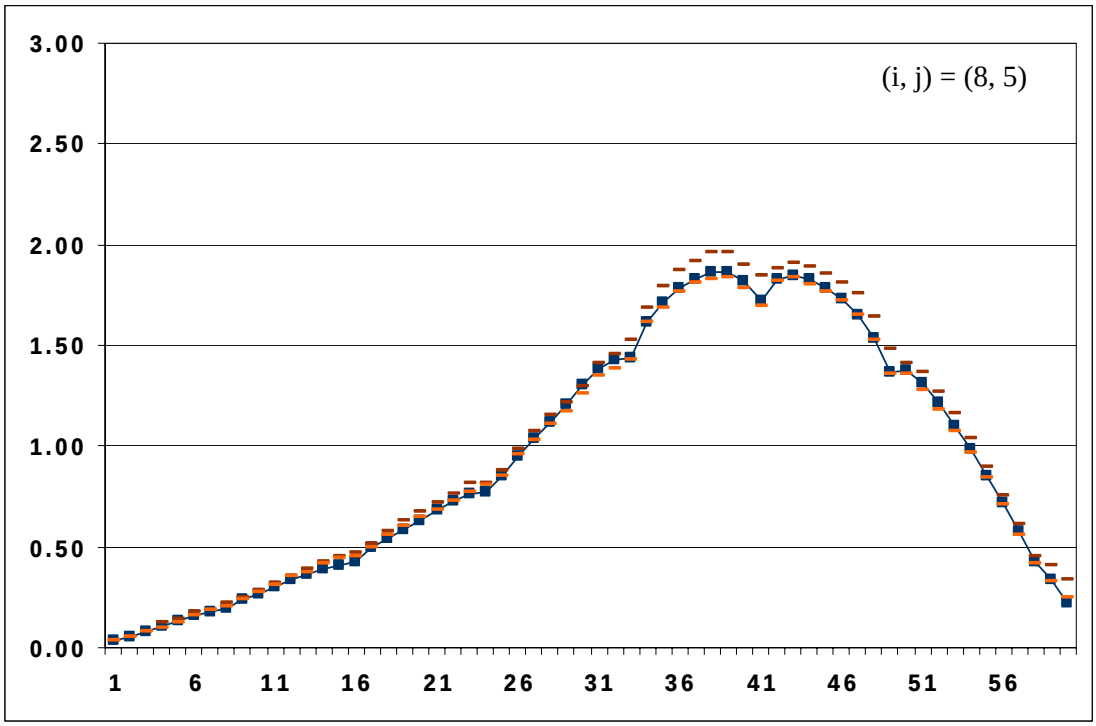
3.00
2.50
2.00
1.50
1.00
0.50
0.00
1
6
11
16
21
26
31
36
41
46
51
56
(i, j) = (8, 5)

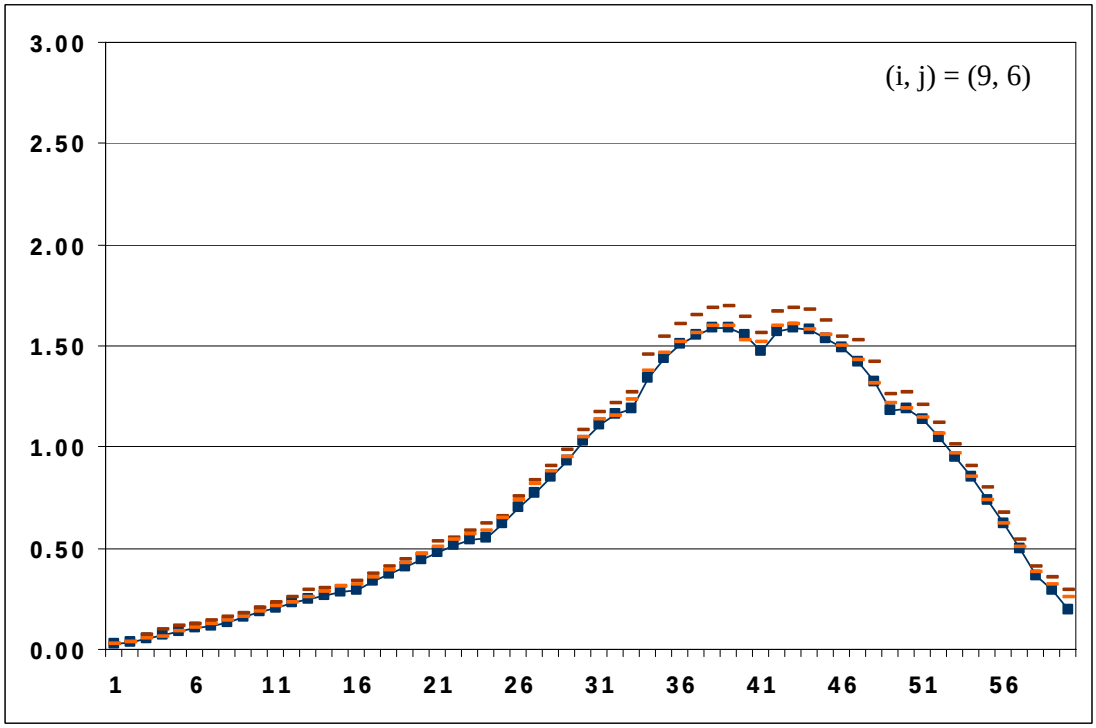
3.00
2.50
2.00
1.50
1.00
0.50
0.00
1
6
11
16
21
26
31
36
41
46
51
56
(i, j) = (9, 6)

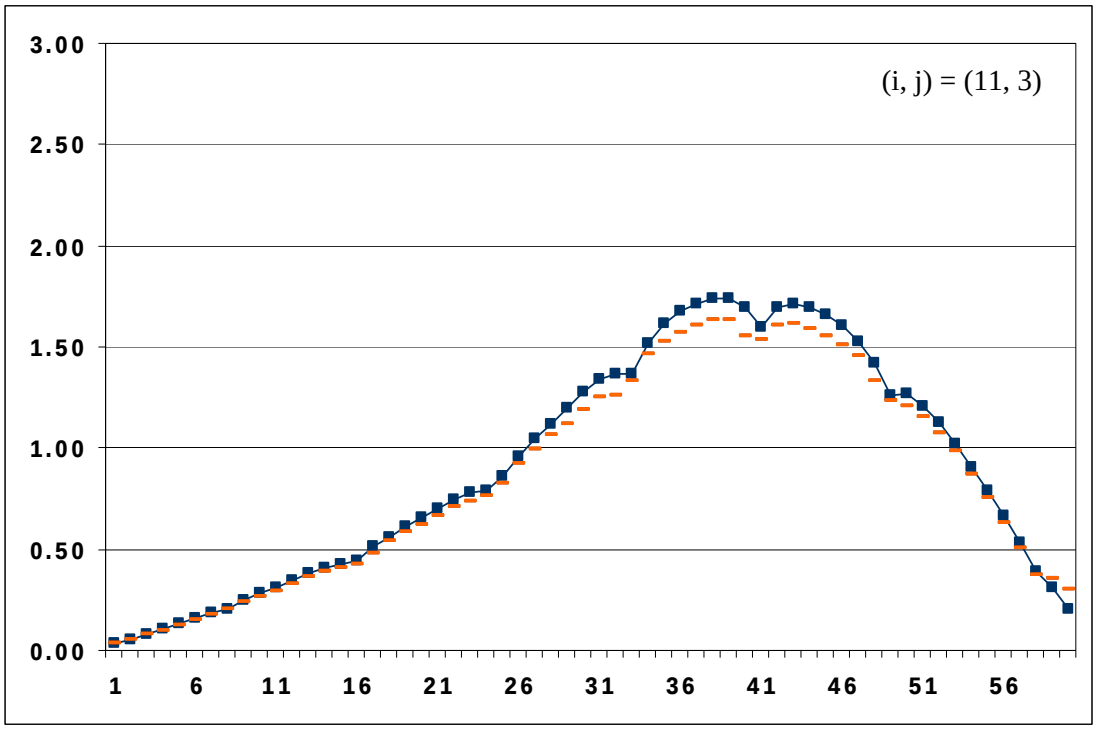
(i, j) = (11, 3)
3.00
2.50
2.00
1.50
1.00
0.50
0.00
1
6
11
16
21
26
31
36
41
46
51
56

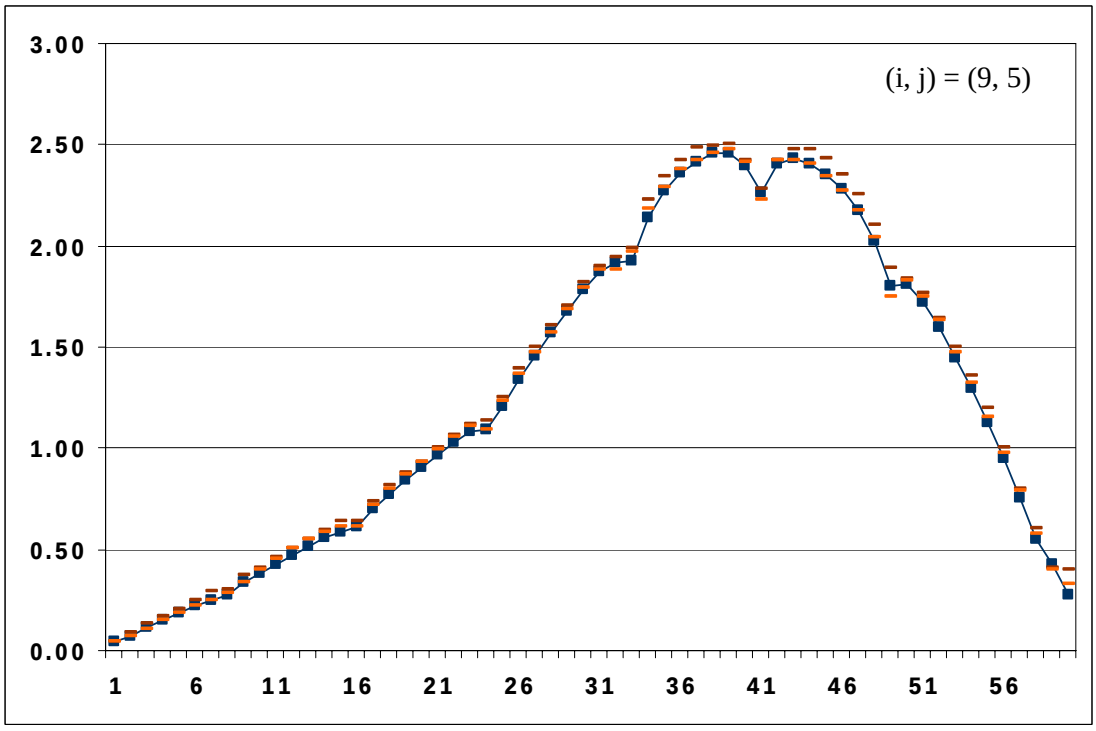
(i, j) = (9, 5)
3.00
2.50
2.00
1.50
1.00
0.50
0.00
1
6
11
16
21
26
31
36
41
46
51
56

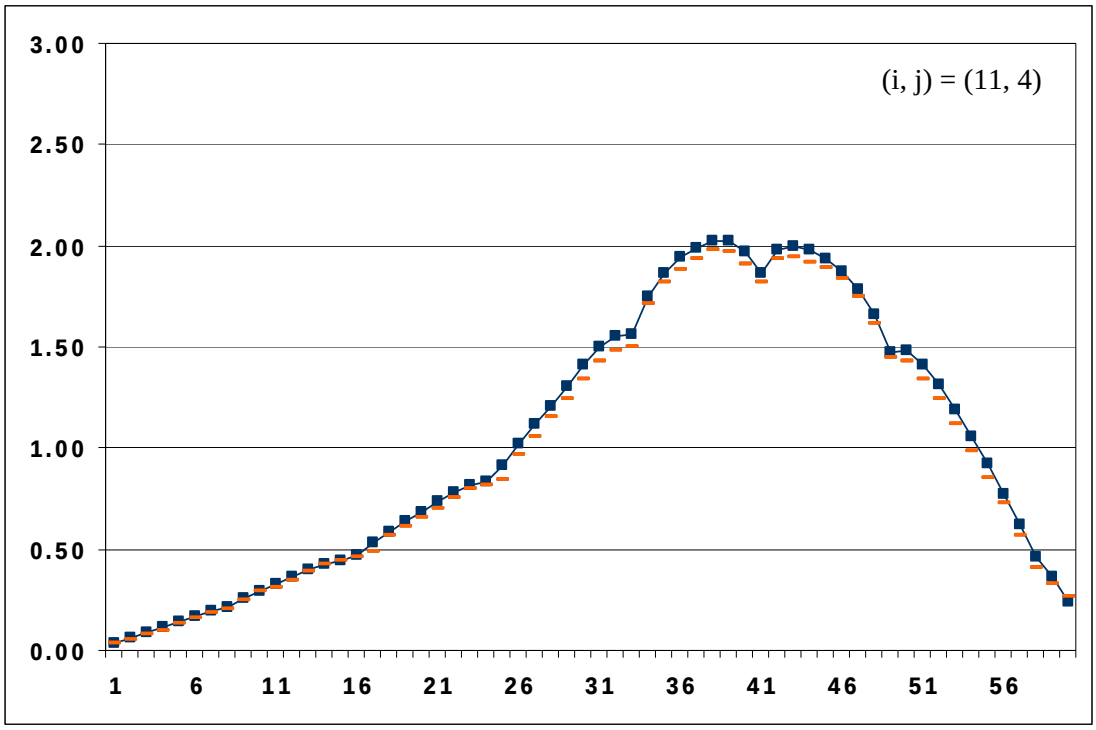
(i, j) = (11, 4)
3.00
2.50
2.00
1.50
1.00
0.50
0.00
1
6
11
16
21
26
31
36
41
46
51
56

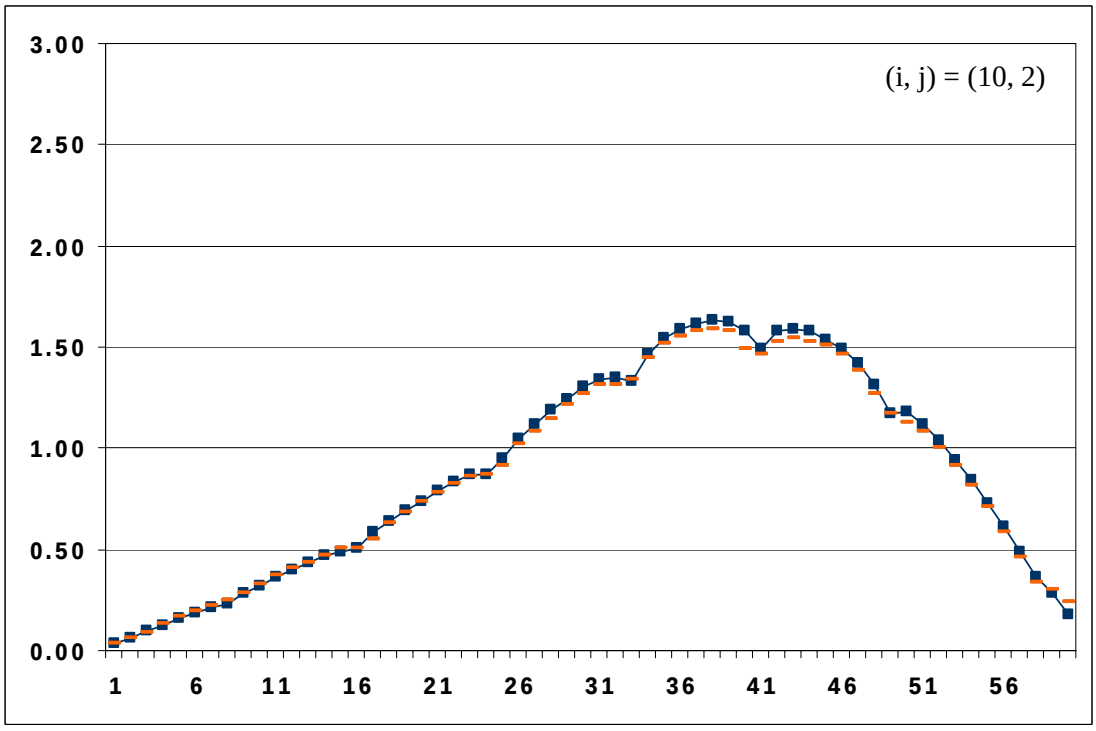
(i, j) = (10, 2)
3.00
2.50
2.00
1.50
1.00
0.50
0.00
1
6
11
16
21
26
31
36
41
46
51
56

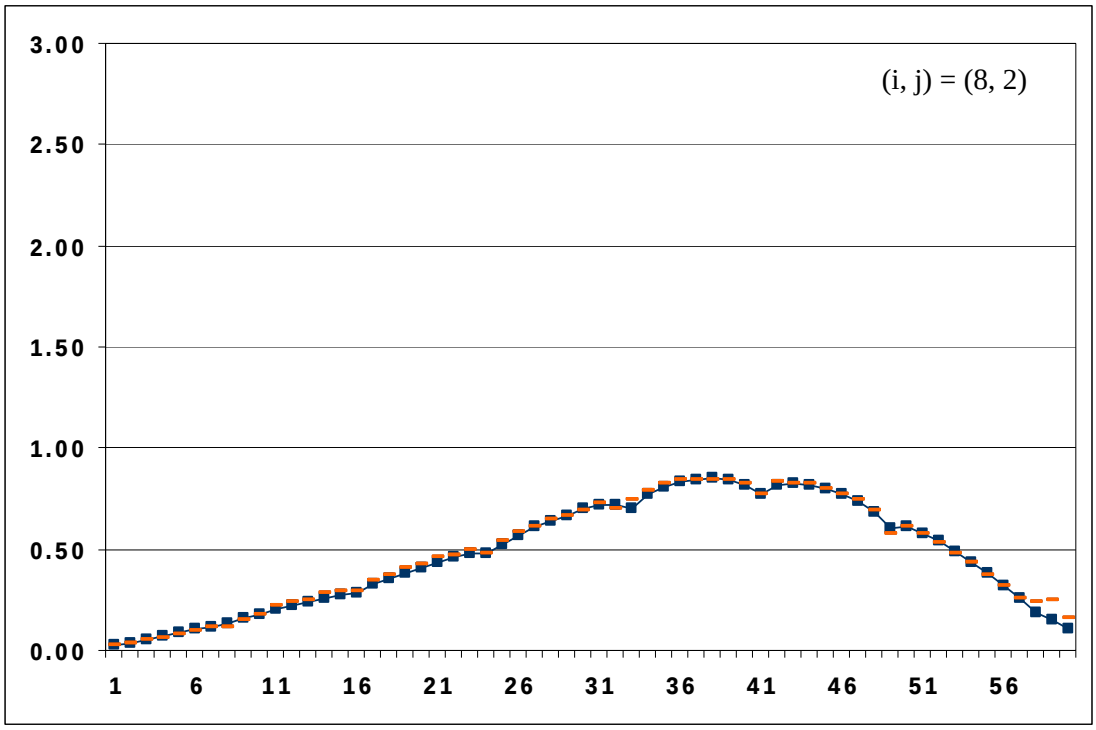
(i, j) = (8, 2)
3.00
2.50
2.00
1.50
1.00
0.50
0.00
1
6
11
16
21
26
31
36
41
46
51
56

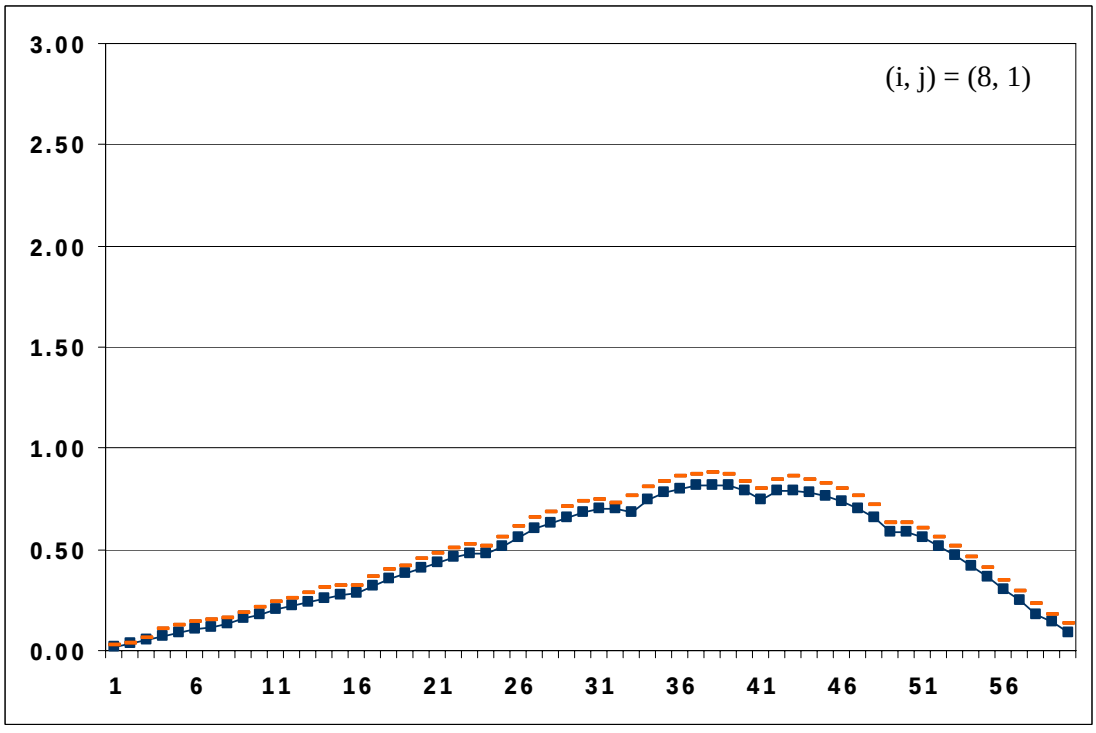
(i, j) = (8, 1)
3.00
2.50
2.00
1.50
1.00
0.50
0.00
1
6
11
16
21
26
31
36
41
46
51
56

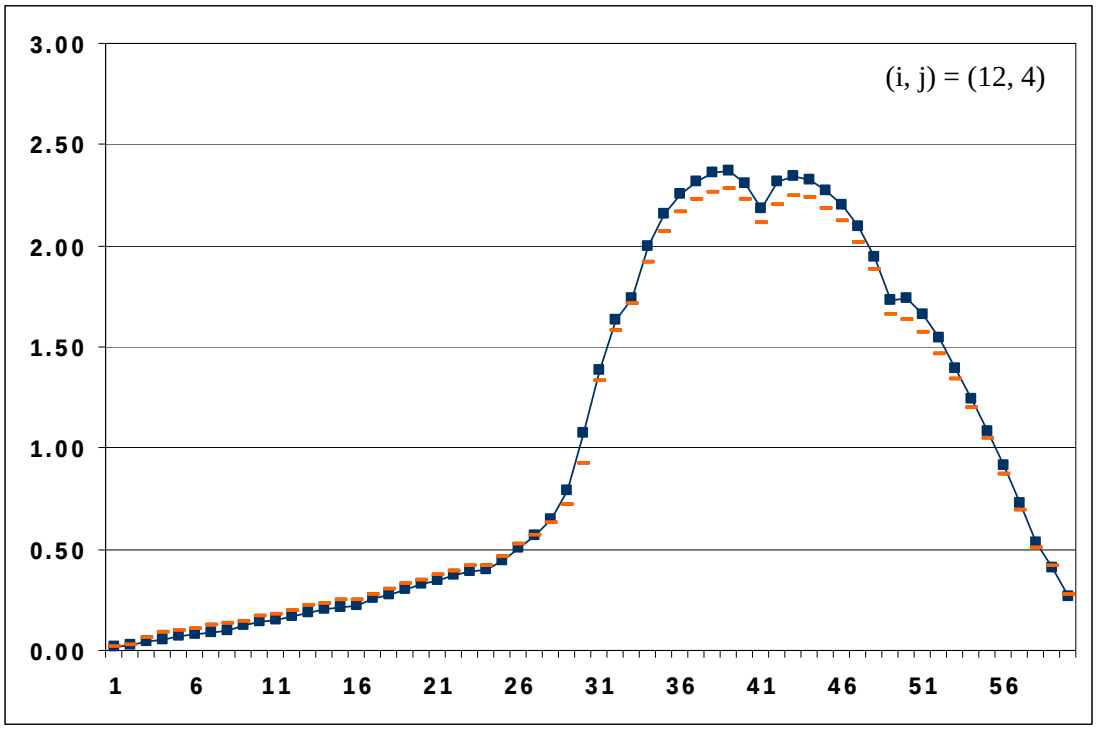
(i, j) = (12, 4)
3.00
2.50
2.00
1.50
1.00
0.50
0.00
1
6
11
16
21
26
31
36
41
46
51
56

B.3 Case 3

The following figures show the comparison of the measured and VNEM-calculated relative detector readings. Both are independently normalized so that the spatial average of the readings over all the measuring points becomes 1.0. Here in the figures:

- ■ : VNEM-calculated relative readings
- — : Upper bound to the measured readings
- — : Lower bound to the measured readings

The upper / lower bounds of the measured readings are defined by the maximum / minimum of the readings of the assemblies at the octant-symmetric positions in the core. The representative of the octant-symmetric positions (i, j) in the core is taken from the north-north-east portion (shown in Fig.1.5.8).

As in Fig.1.5.7, the horizontal axis indicates the axial measuring positions along a thimble that are numbered 1 through 60 from the top to the bottom of the core. The vertical axis indicates the relative detector readings in an arbitrary unit.

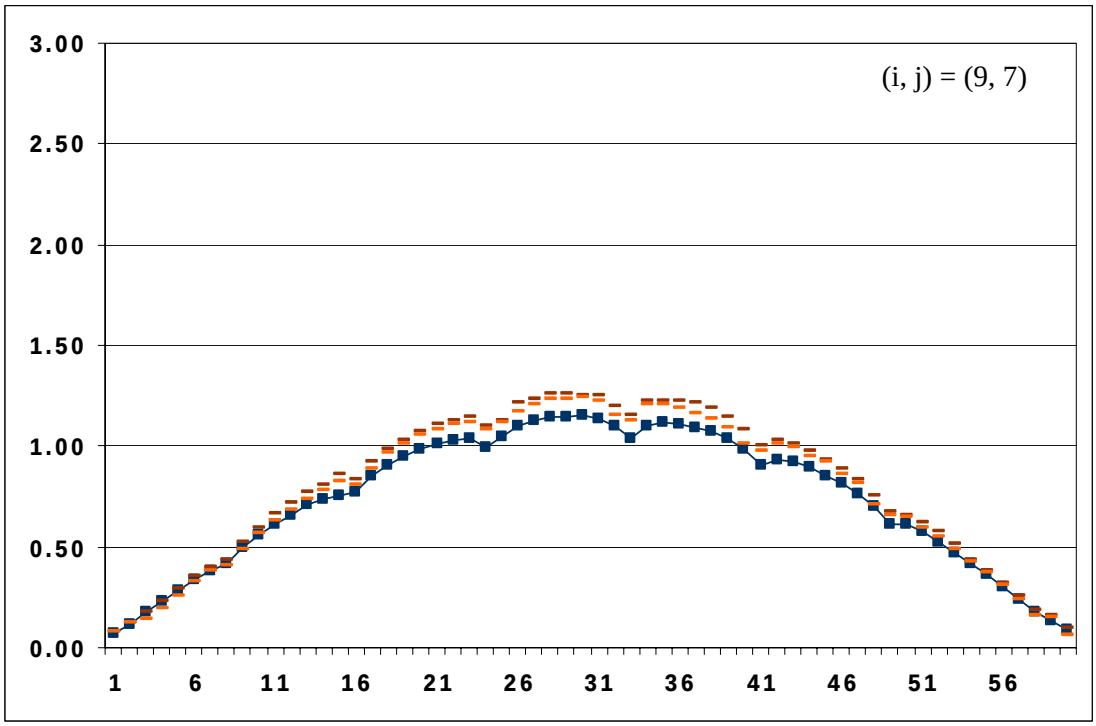
3.00
2.50
2.00
1.50
1.00
0.50
0.00
(i, j) = (9, 7)
1
6
11
16
21
26
31
36
41
46
51
56

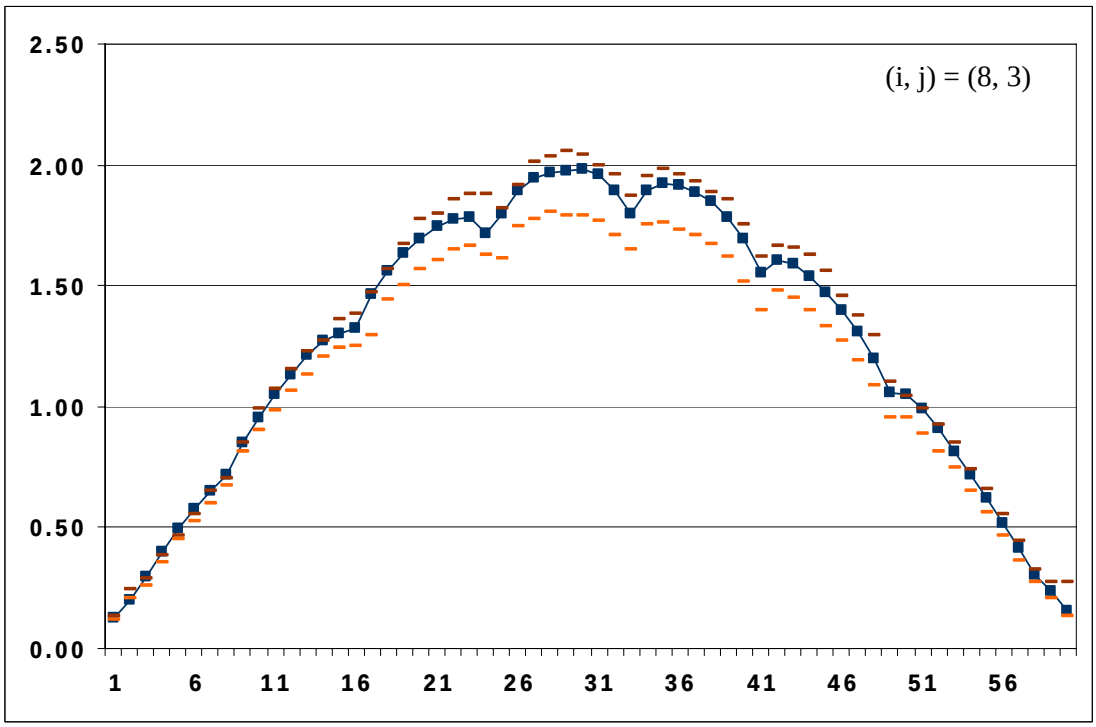
2.50
2.00
1.50
1.00
0.50
0.00
(i, j) = (8, 3)
1
6
11
16
21
26
31
36
41
46
51
56

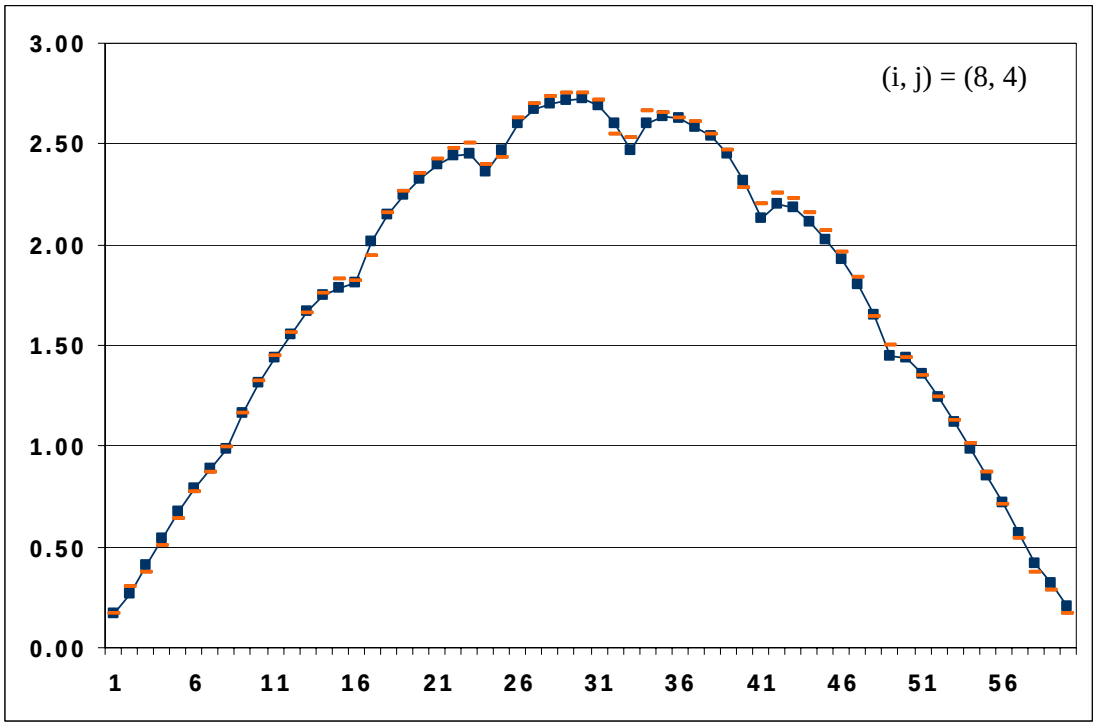
(i, j) = (8, 4)
3.00
2.50
2.00
1.50
1.00
0.50
0.00
1
6
11
16
21
26
31
36
41
46
51
56

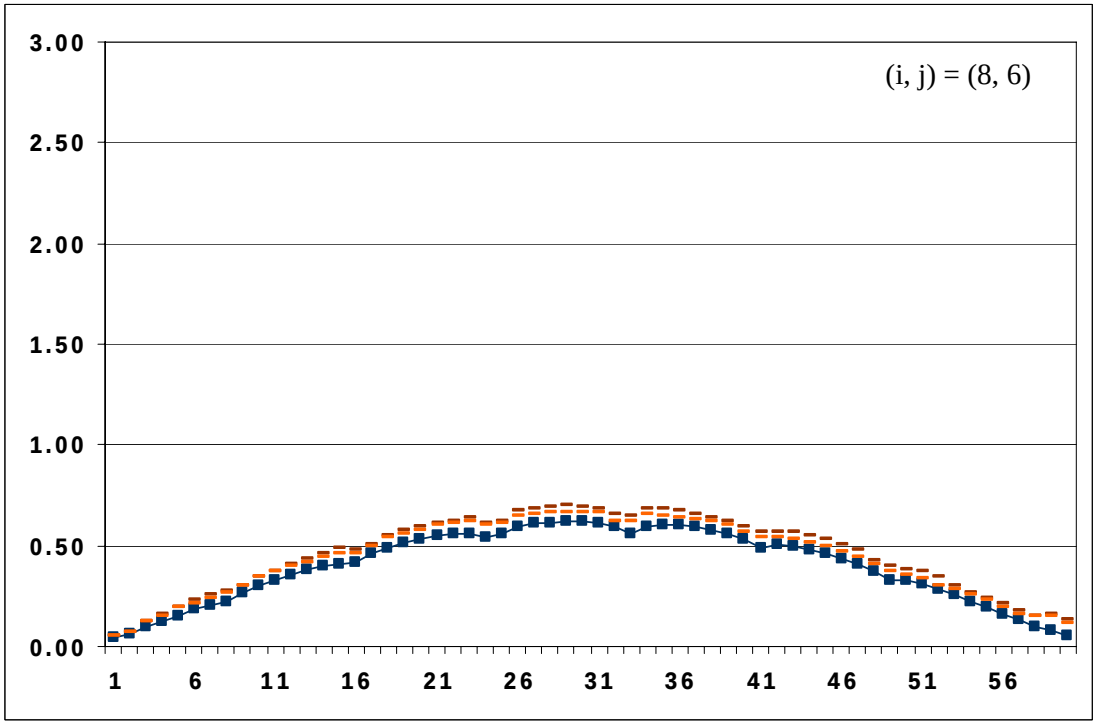
(i, j) = (8, 6)
3.00
2.50
2.00
1.50
1.00
0.50
0.00
1
6
11
16
21
26
31
36
41
46
51
56

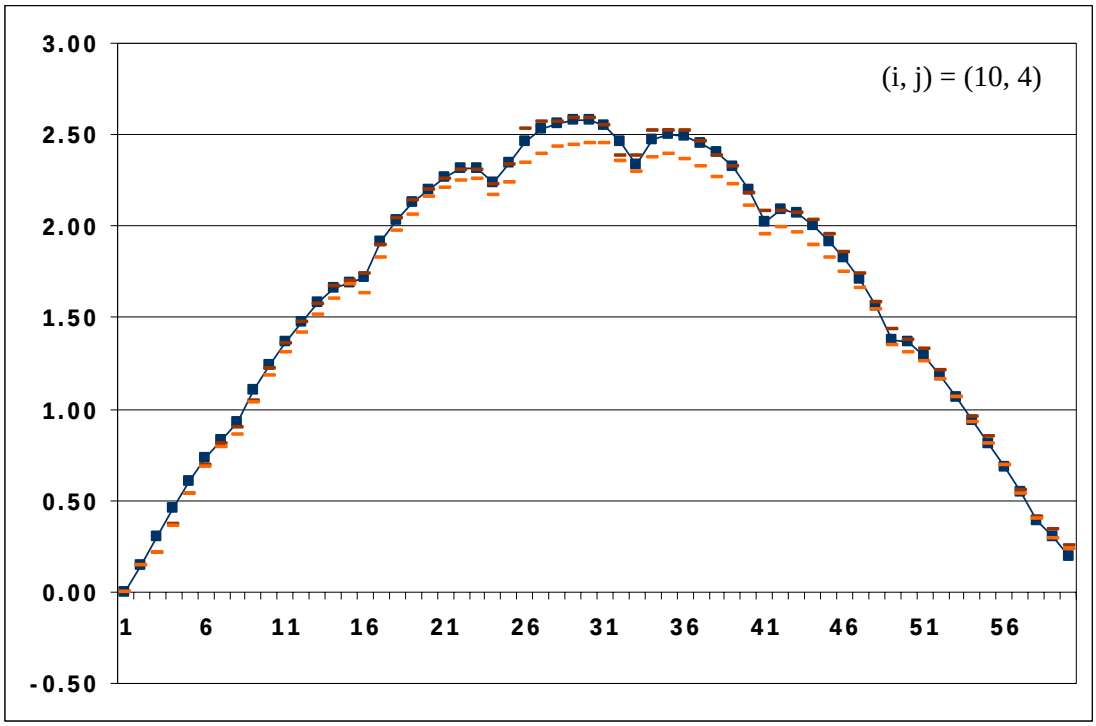
(i, j) = (10, 4)
3.00
2.50
2.00
1.50
1.00
0.50
0.00
-0.50
1
6
11
16
21
26
31
36
41
46
51
56

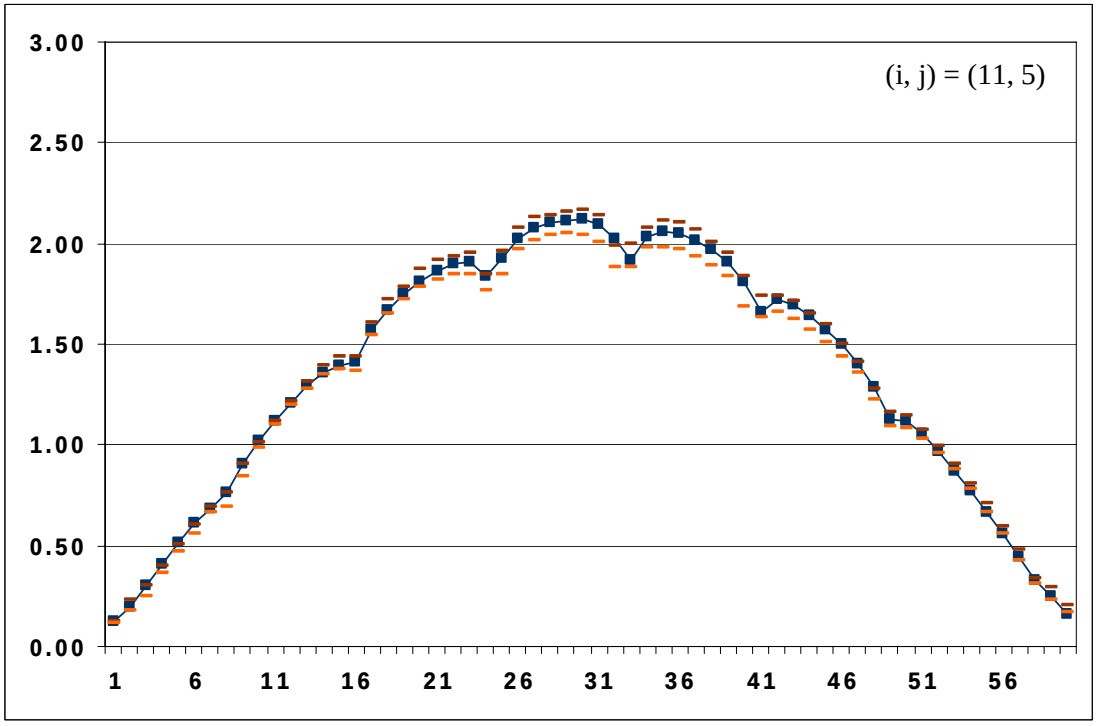
(i, j) = (11, 5)
3.00
2.50
2.00
1.50
1.00
0.50
0.00
1
6
11
16
21
26
31
36
41
46
51
56

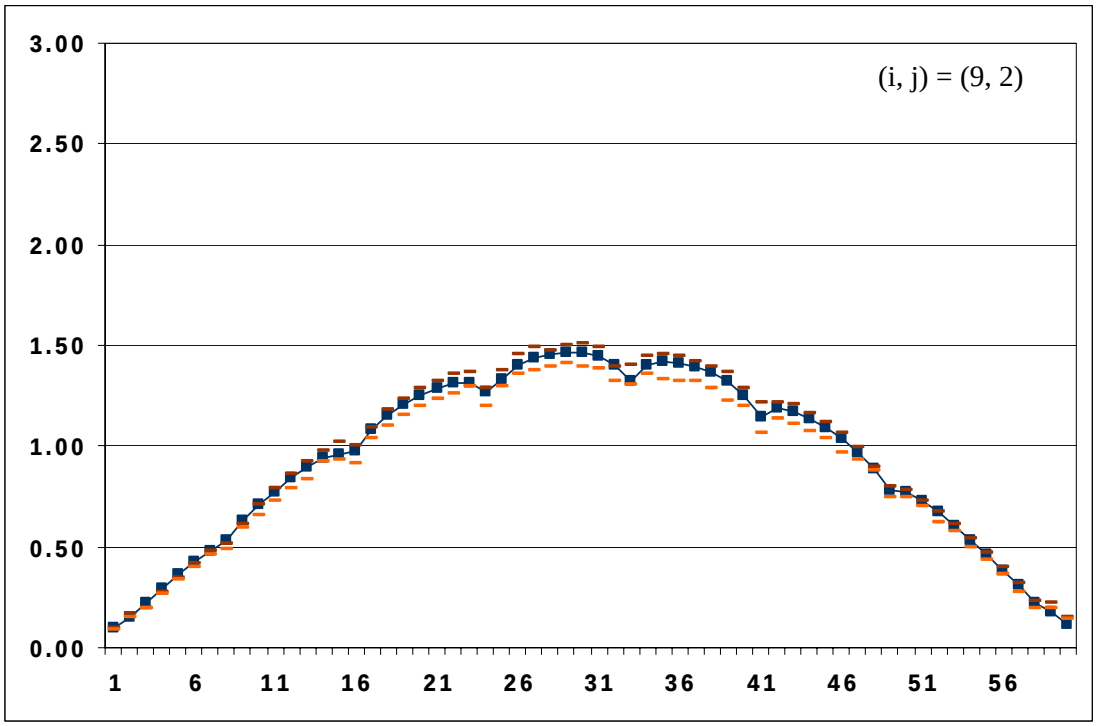
(i, j) = (9, 2)
3.00
2.50
2.00
1.50
1.00
0.50
0.00
1
6
11
16
21
26
31
36
41
46
51
56

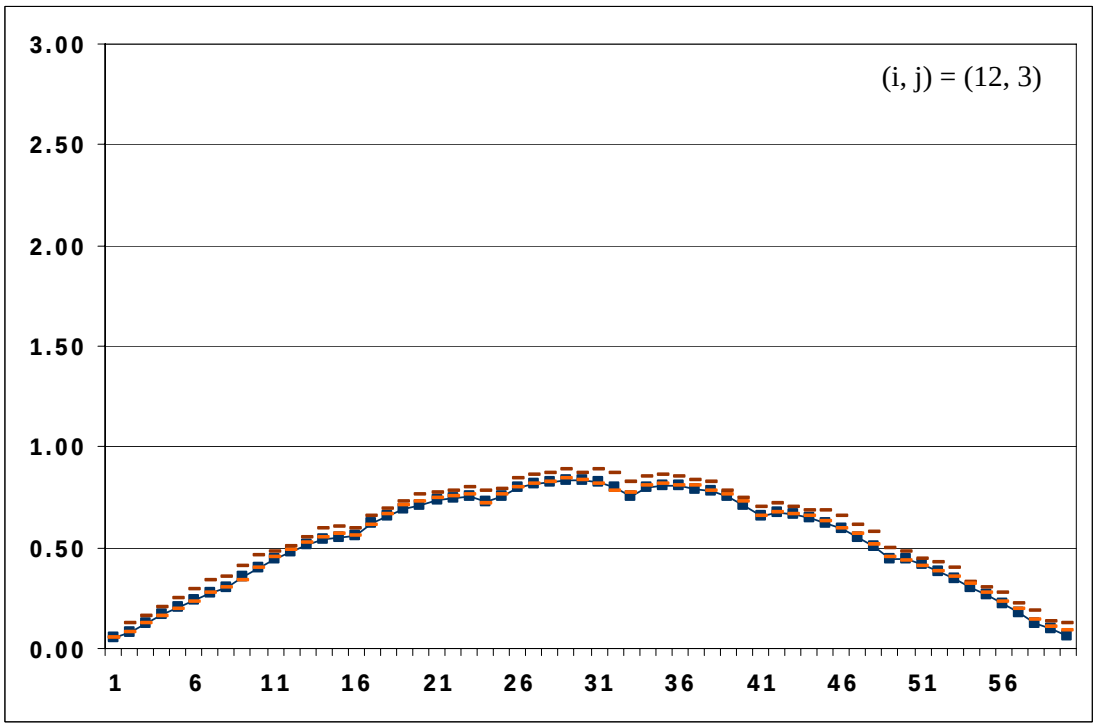
(i, j) = (12, 3)
3.00
2.50
2.00
1.50
1.00
0.50
0.00
1
6
11
16
21
26
31
36
41
46
51
56

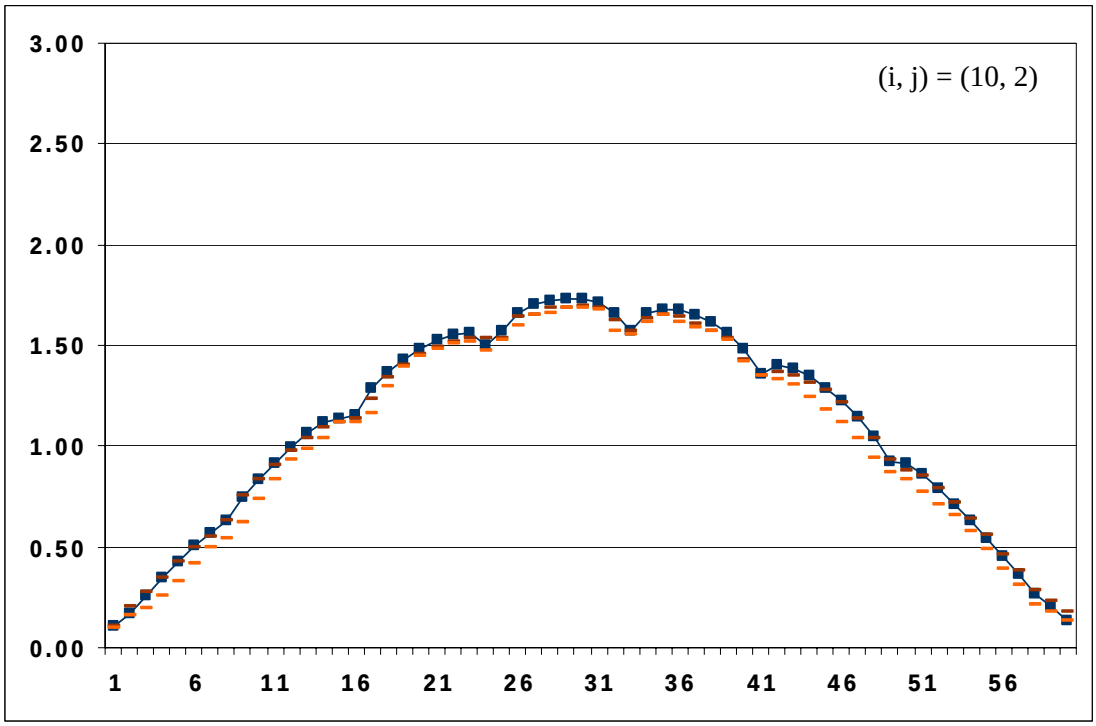
(i, j) = (10, 2)
3.00
2.50
2.00
1.50
1.00
0.50
0.00
1
6
11
16
21
26
31
36
41
46
51
56

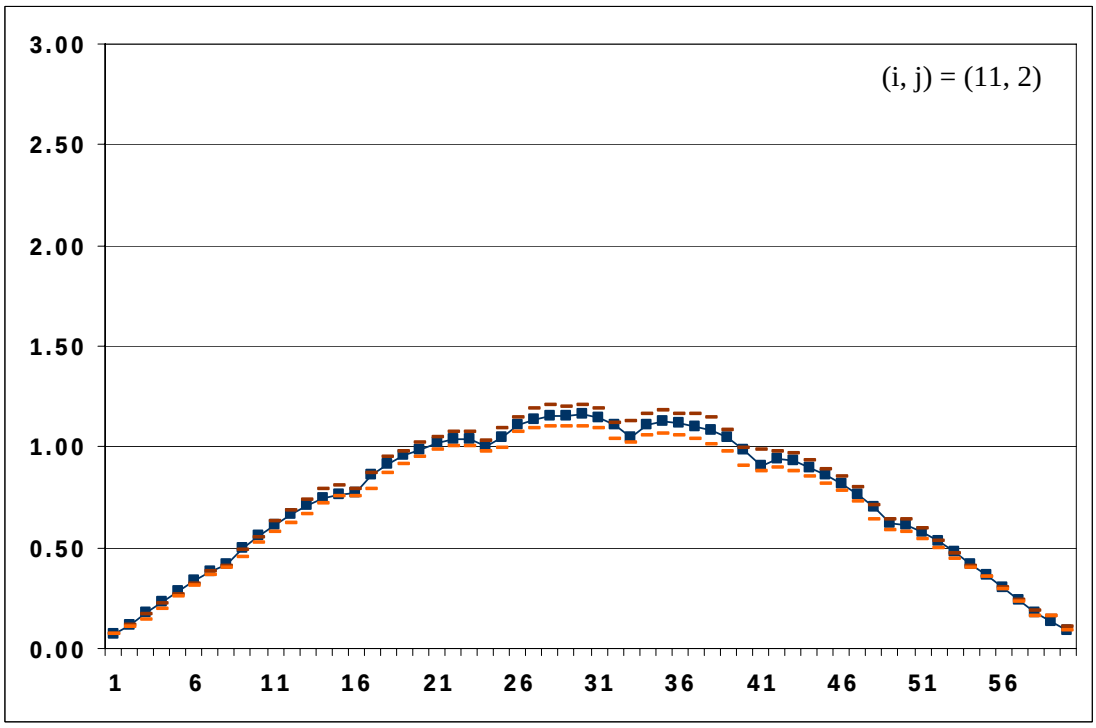
(i, j) = (11, 2)
3.00
2.50
2.00
1.50
1.00
0.50
0.00
1
6
11
16
21
26
31
36
41
46
51
56

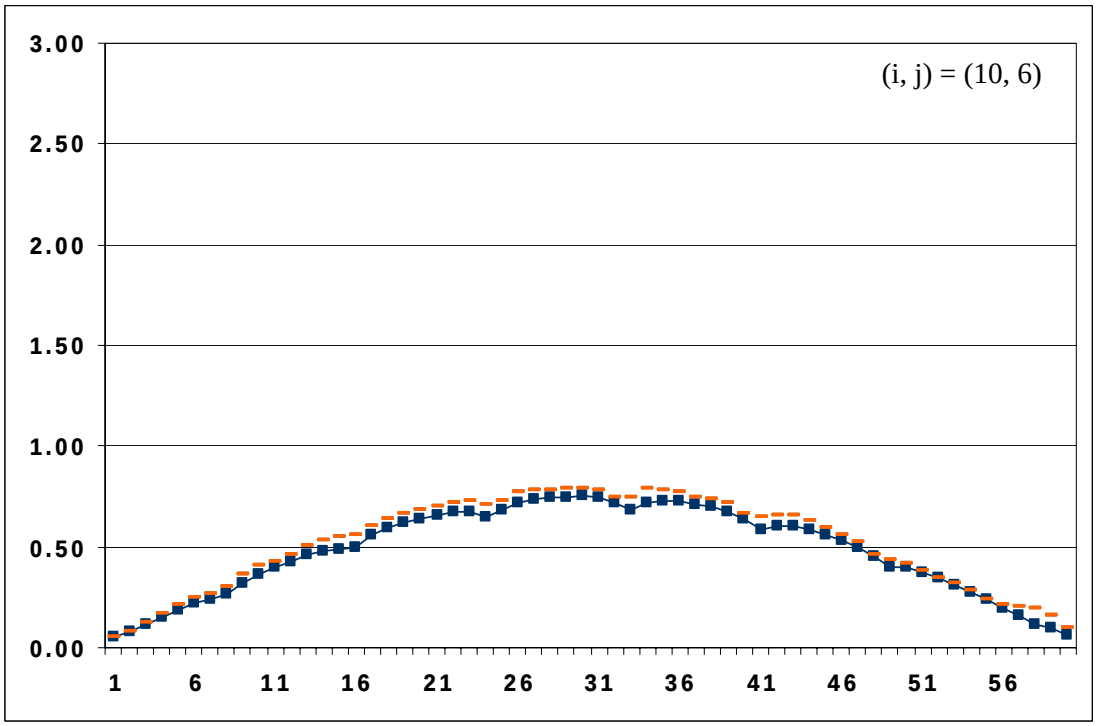
(i, j) = (10, 6)
3.00
2.50
2.00
1.50
1.00
0.50
0.00
1
6
11
16
21
26
31
36
41
46
51
56

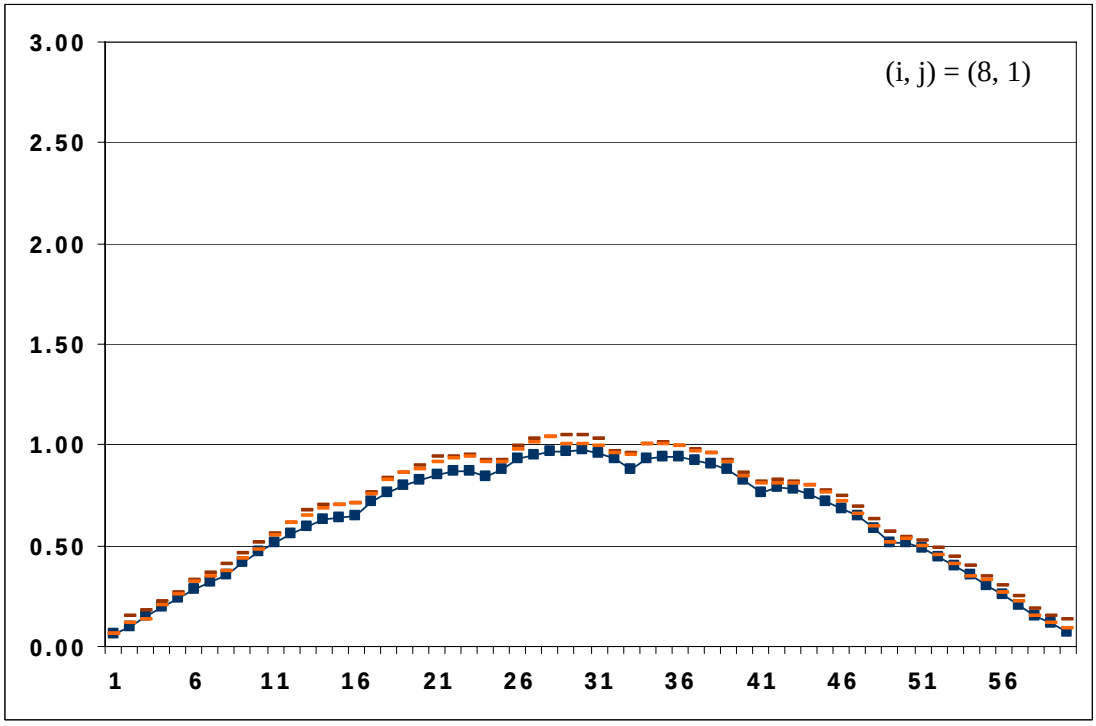
(i, j) = (8, 1)
3.00
2.50
2.00
1.50
1.00
0.50
0.00
1
6
11
16
21
26
31
36
41
46
51
56

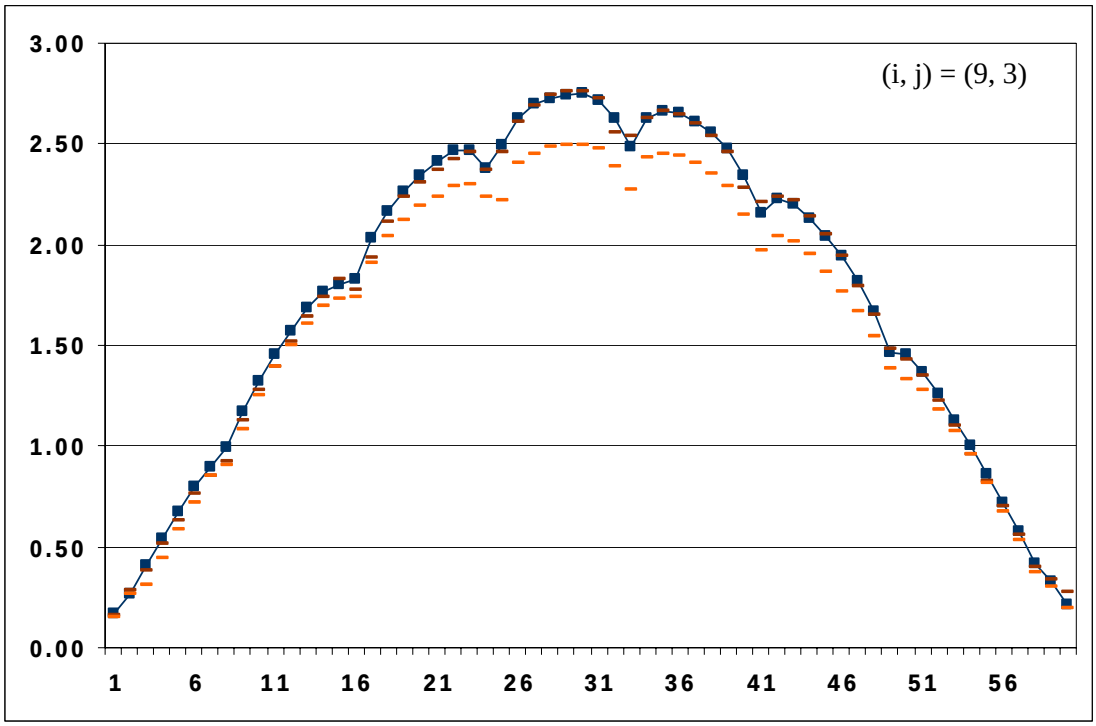
(i, j) = (9, 3)
3.00
2.50
2.00
1.50
1.00
0.50
0.00
1
6
11
16
21
26
31
36
41
46
51
56

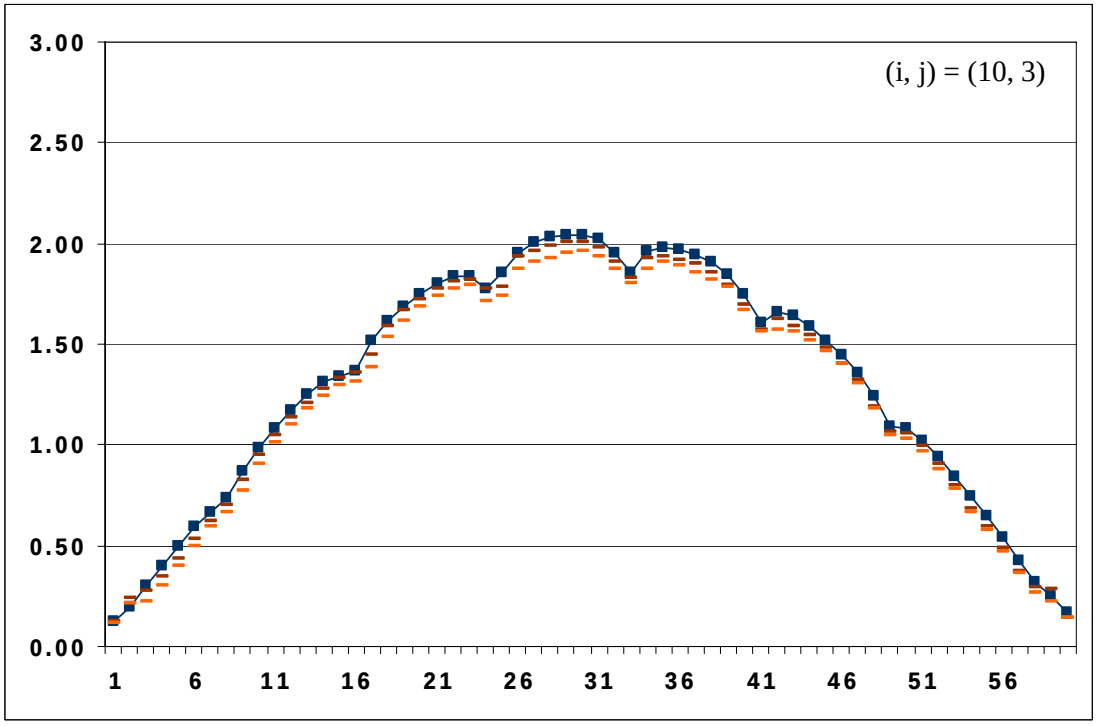
(i, j) = (10, 3)
3.00
2.50
2.00
1.50
1.00
0.50
0.00
1
6
11
16
21
26
31
36
41
46
51
56

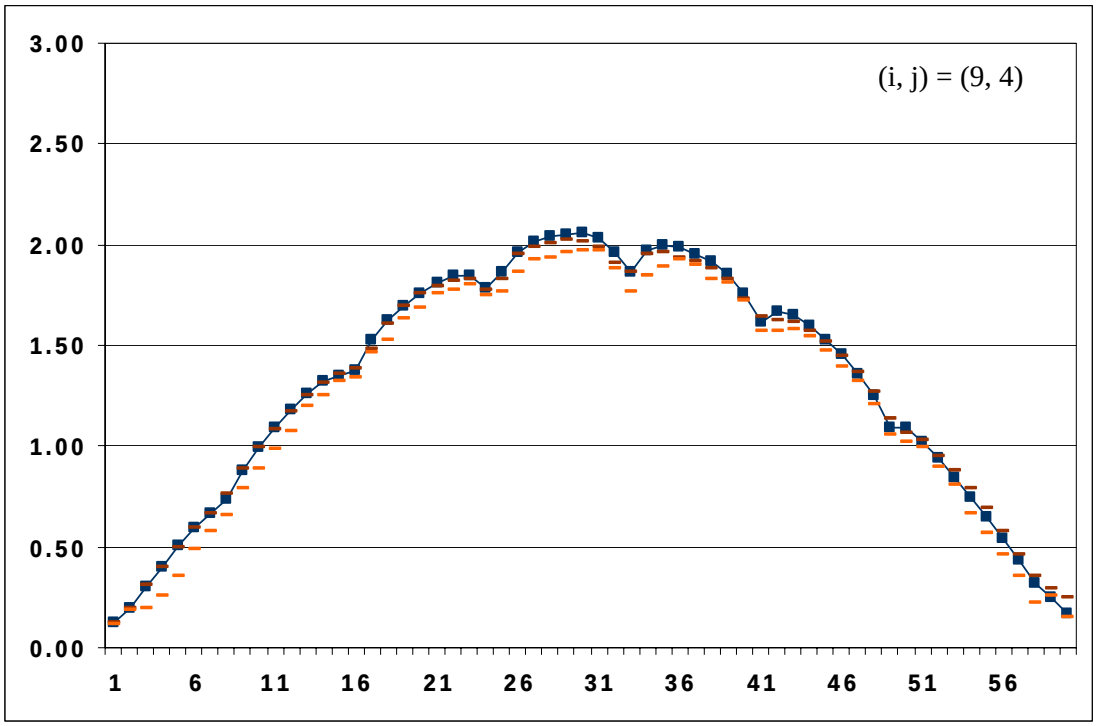
(i, j) = (9, 4)
3.00
2.50
2.00
1.50
1.00
0.50
0.00
1
6
11
16
21
26
31
36
41
46
51
56

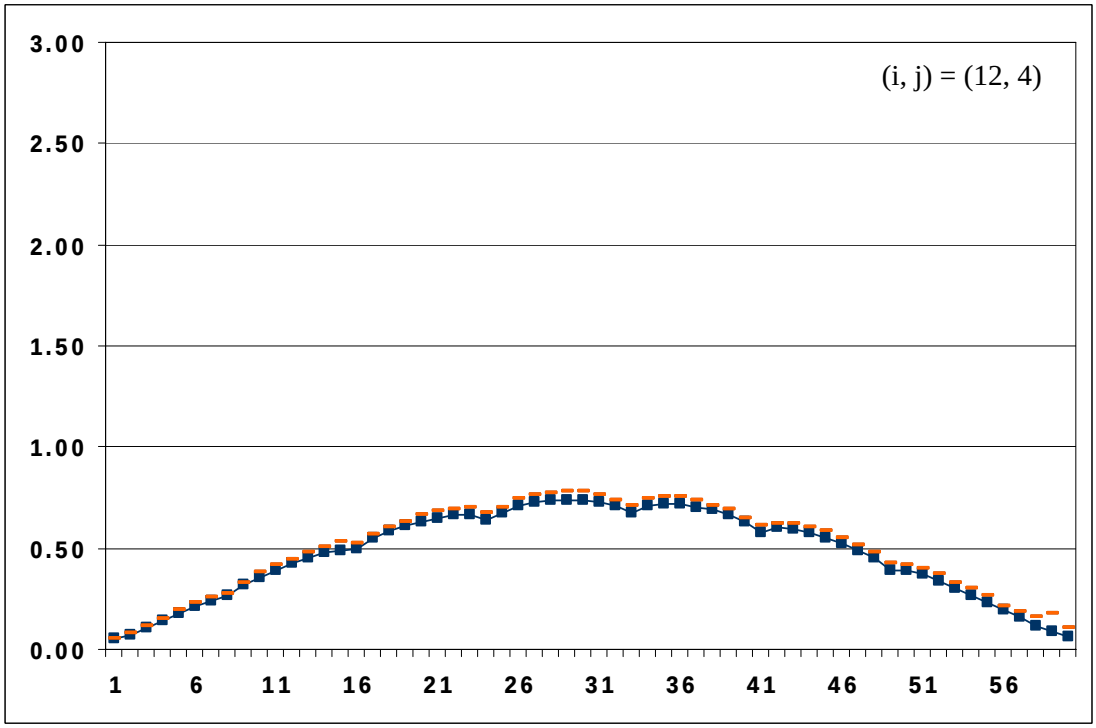
(i, j) = (12, 4)
3.00
2.50
2.00
1.50
1.00
0.50
0.00
1
6
11
16
21
26
31
36
41
46
51
56

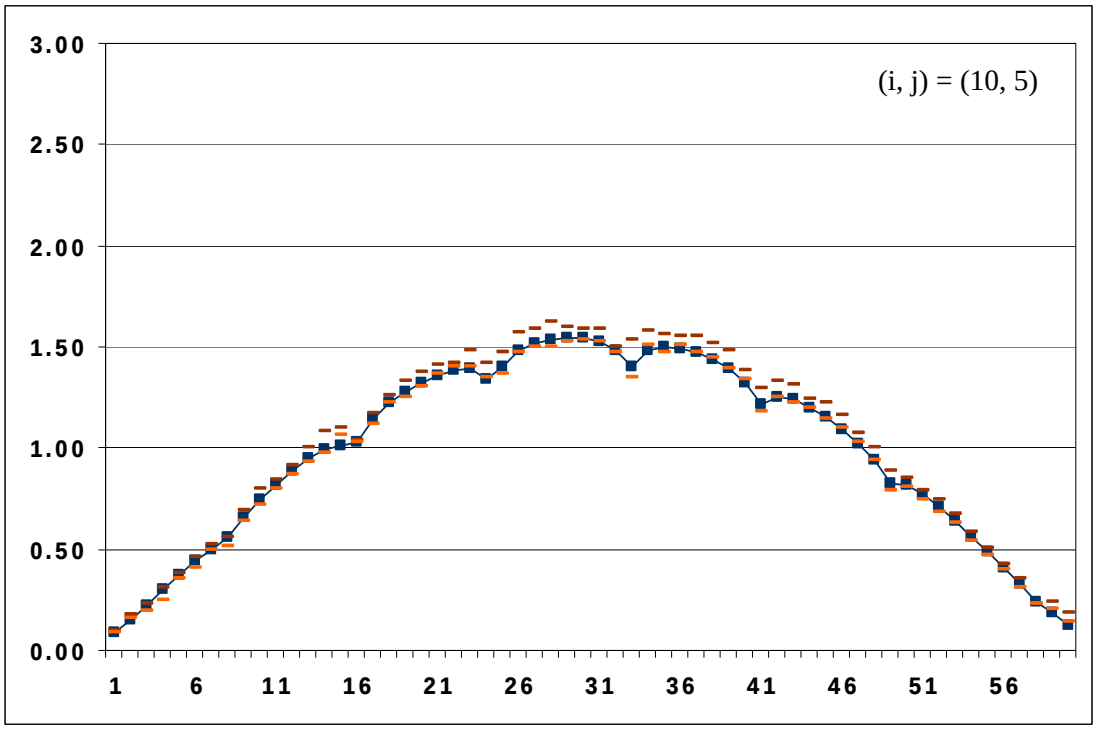
(i, j) = (10, 5)
3.00
2.50
2.00
1.50
1.00
0.50
0.00
1
6
11
16
21
26
31
36
41
46
51
56

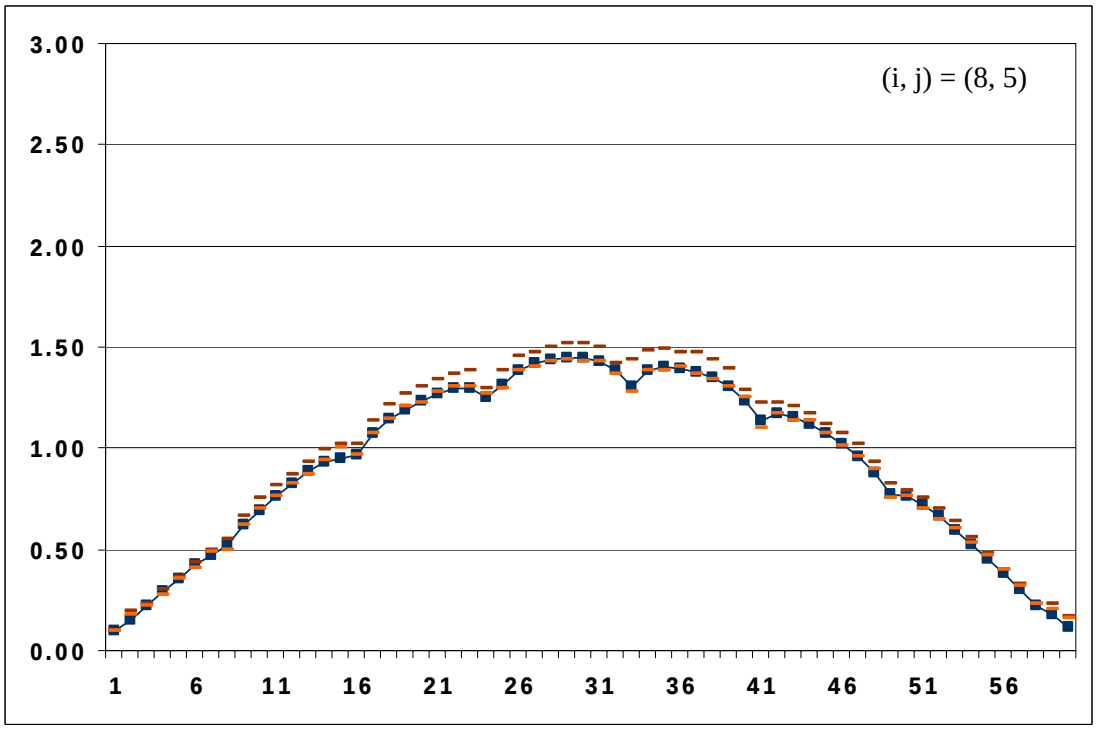
(i, j) = (8, 5)
3.00
2.50
2.00
1.50
1.00
0.50
0.00
1
6
11
16
21
26
31
36
41
46
51
56

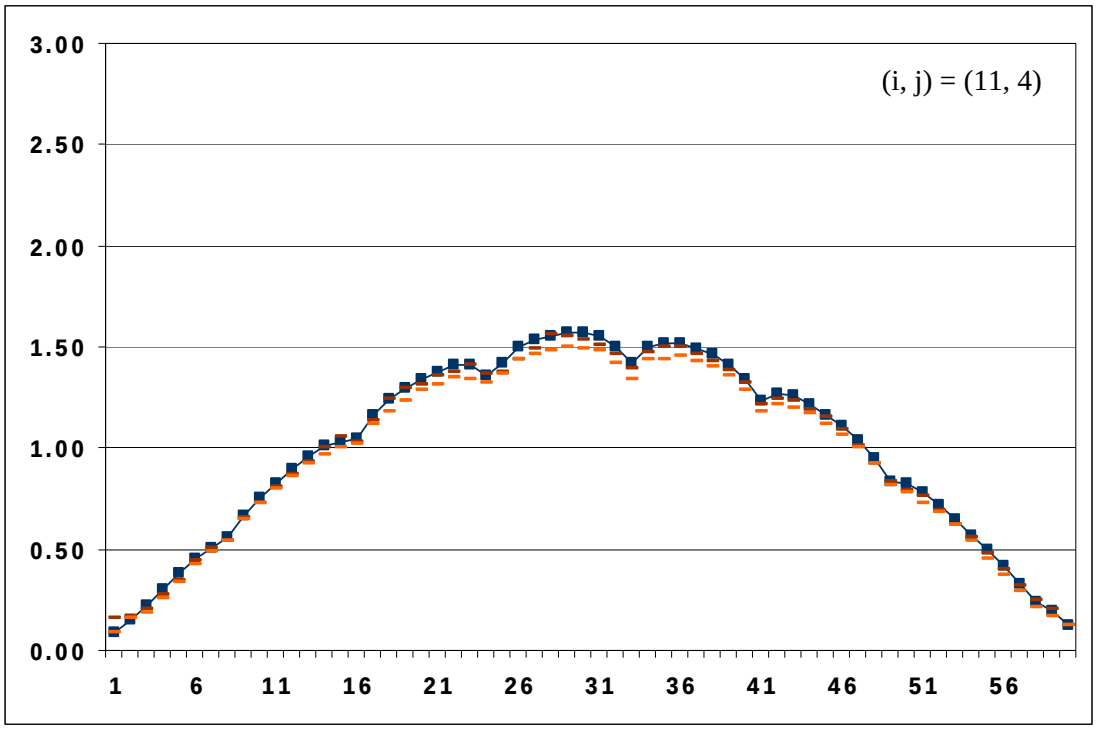
(i, j) = (11, 4)
3.00
2.50
2.00
1.50
1.00
0.50
0.00
1
6
11
16
21
26
31
36
41
46
51
56

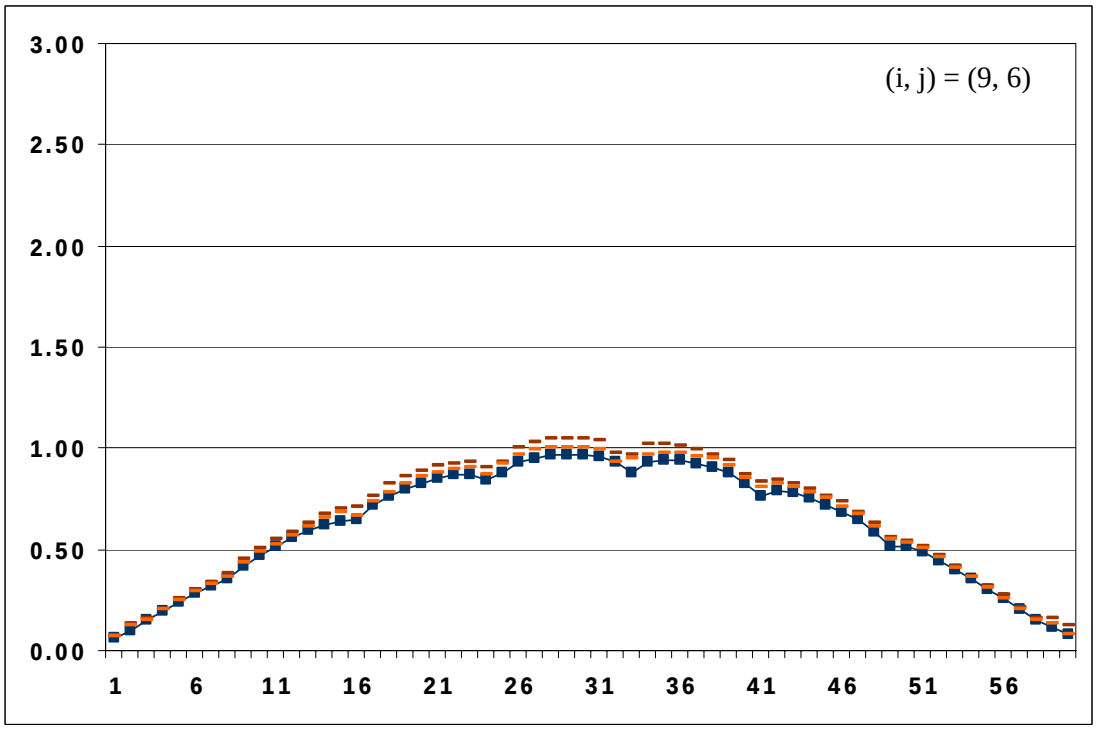
(i, j) = (9, 6)
3.00
2.50
2.00
1.50
1.00
0.50
0.00
1
6
11
16
21
26
31
36
41
46
51
56

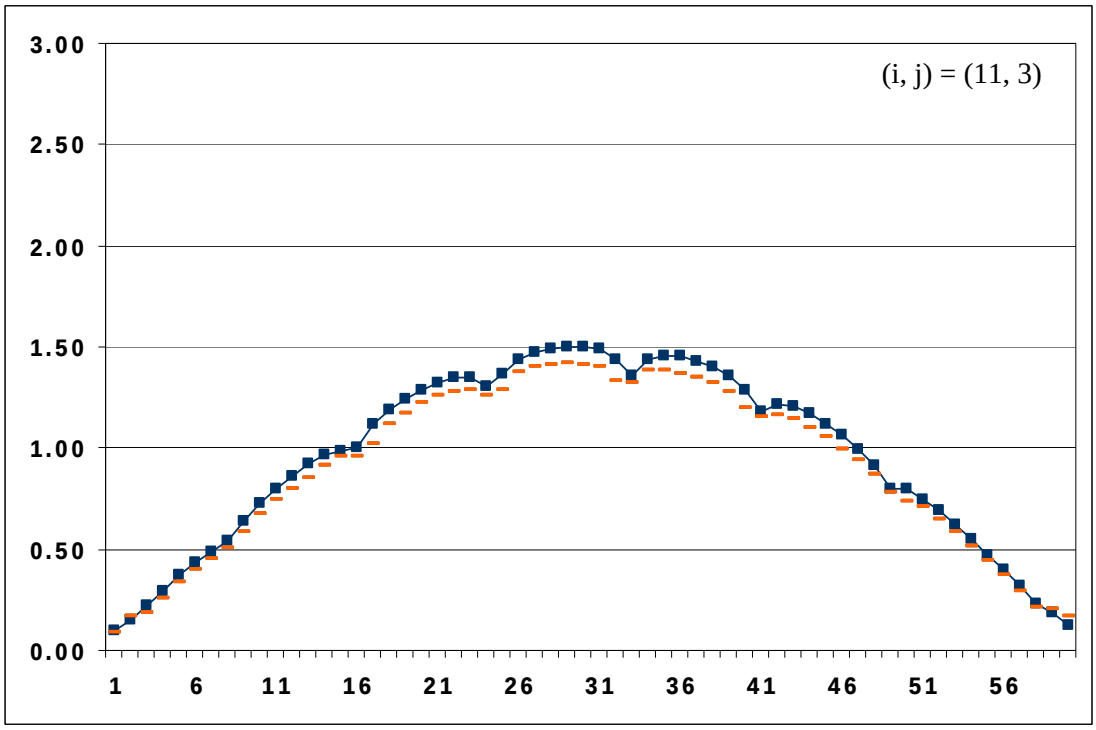
(i, j) = (11, 3)
3.00
2.50
2.00
1.50
1.00
0.50
0.00
1
6
11
16
21
26
31
36
41
46
51
56

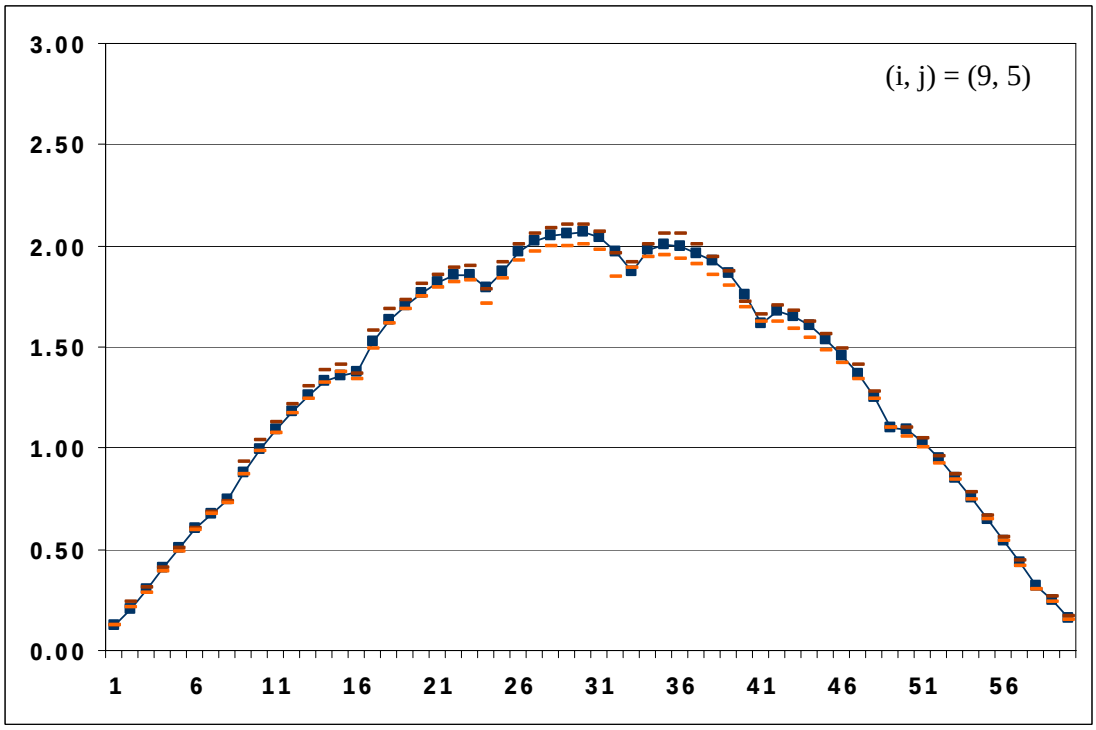
(i, j) = (9, 5)
3.00
2.50
2.00
1.50
1.00
0.50
0.00
1
6
11
16
21
26
31
36
41
46
51
56

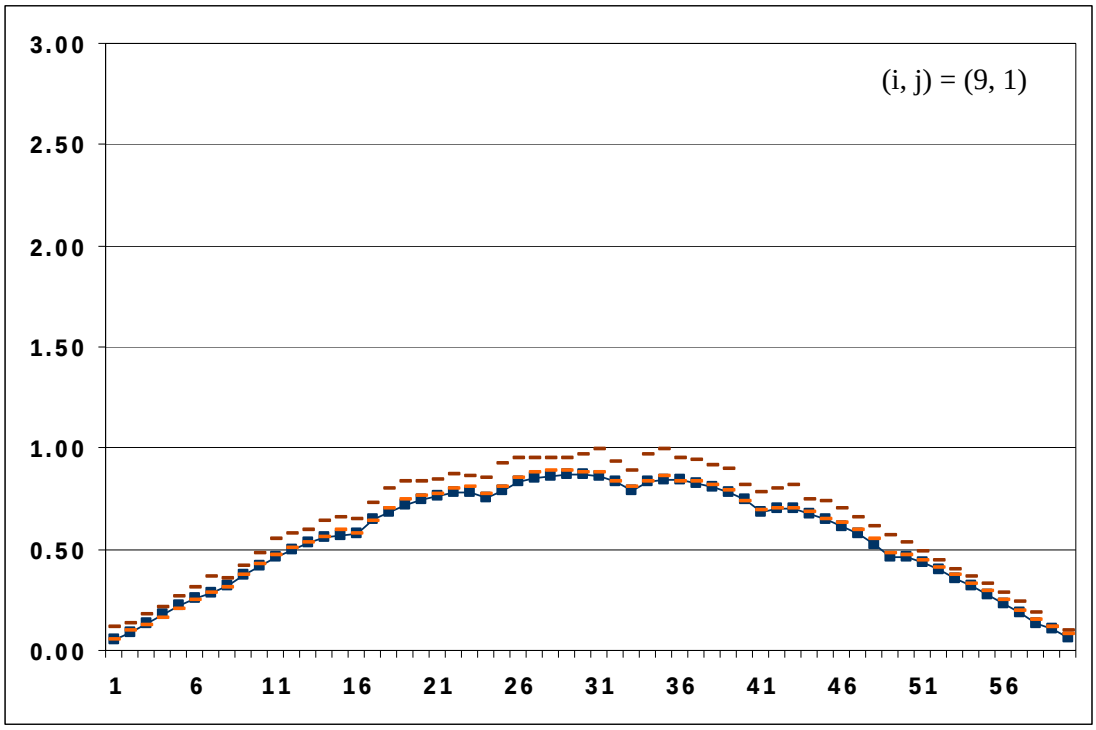
(i, j) = (9, 1)
3.00
2.50
2.00
1.50
1.00
0.50
0.00
1
6
11
16
21
26
31
36
41
46
51
56

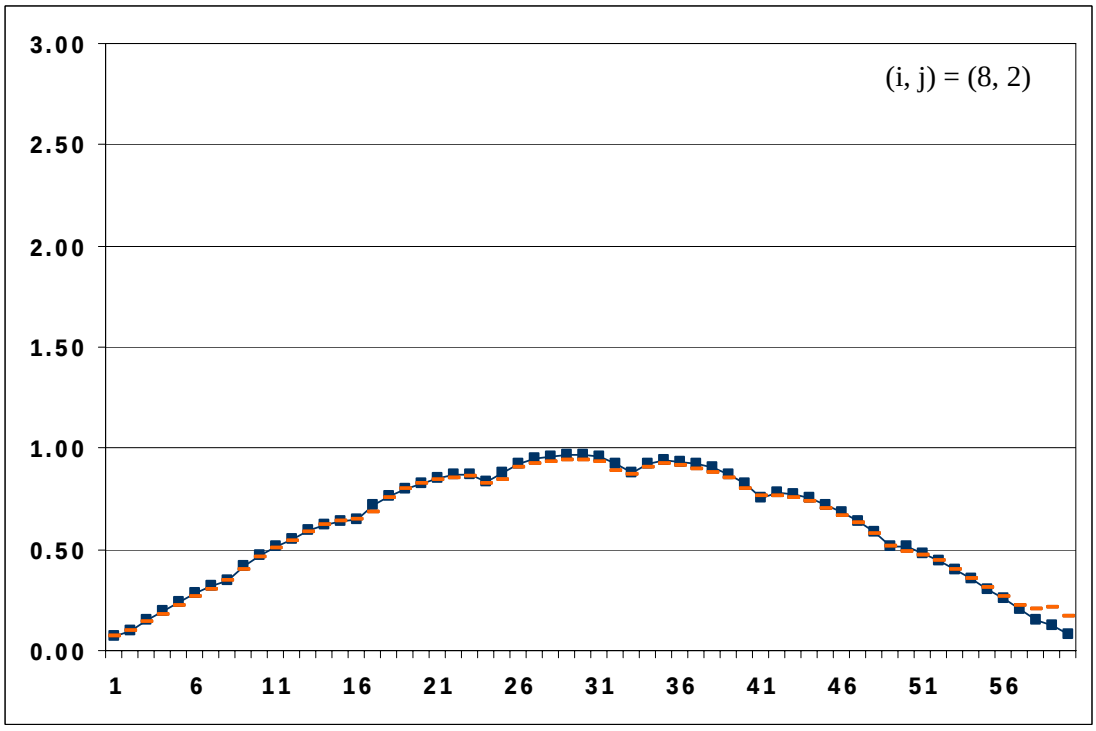
(i, j) = (8, 2)
3.00
2.50
2.00
1.50
1.00
0.50
0.00
1
6
11
16
21
26
31
36
41
46
51
56

Title	Improving Accuracy of the Calculation of In-core Power Distributions for Light Water Reactors
Author(s)	Makoto Tsuiki and William H. Beere
Affiliation(s)	Institute for energy technology, OECD Halden Reactor Project, Norway
ISBN	978-87-7893-272-3
Date	October 2009
Project	NKS-R / IACIP
No. of pages	79
No. of tables	4
No. of illustrations	13
No. of references	4

Abstract

Comparisons have been made of VNEM prototype system to the measured data obtained from Ringhals unit 3 NPP at its beginning of life, hot-stand-by state. Three cases with difference control rod bank positions and Boron concentrations have been compared:

Case 1: nearly all rod banks withdrawn, Boron = 1315 ppm
Case 2: bank C = nearly half-inserted, bank D = fully inserted, Boron = 1131 ppm
Case 3: banks C and D = fully inserted, Boron = 1060 ppm

The results can be summarized as:

	error: maximum detector reading (%)	error: keff (%)
Case 1	-2.1	-0.175
Case 2	1.5	-0.022
Case 3	-0.5	-0.044

Excellent agreement was observed in the comparison of the neutron detector readings and the core eigenvalues.

The method of core modelling and parameters used in calculation of VNEM is completely the same as the "PWR standard option" determined from similar comparisons of VNEM and other PWRs. No empirical, or any sort of adjustment was done.

Key words VNEM, Ringhals, unit 3, PWR, neutron detector, keff, IACIP: NKS_R_2008_61